

Building up a membrane photonics platform in Indium phosphide

Citation for published version (APA):

Pello, J. (2014). *Building up a membrane photonics platform in Indium phosphide*. [Phd Thesis 1 (Research TU/e / Graduation TU/e), Electrical Engineering]. Technische Universiteit Eindhoven. <https://doi.org/10.6100/IR770716>

DOI:

[10.6100/IR770716](https://doi.org/10.6100/IR770716)

Document status and date:

Published: 01/01/2014

Document Version:

Publisher's PDF, also known as Version of Record (includes final page, issue and volume numbers)

Please check the document version of this publication:

- A submitted manuscript is the version of the article upon submission and before peer-review. There can be important differences between the submitted version and the official published version of record. People interested in the research are advised to contact the author for the final version of the publication, or visit the DOI to the publisher's website.
- The final author version and the galley proof are versions of the publication after peer review.
- The final published version features the final layout of the paper including the volume, issue and page numbers.

[Link to publication](#)

General rights

Copyright and moral rights for the publications made accessible in the public portal are retained by the authors and/or other copyright owners and it is a condition of accessing publications that users recognise and abide by the legal requirements associated with these rights.

- Users may download and print one copy of any publication from the public portal for the purpose of private study or research.
- You may not further distribute the material or use it for any profit-making activity or commercial gain
- You may freely distribute the URL identifying the publication in the public portal.

If the publication is distributed under the terms of Article 25fa of the Dutch Copyright Act, indicated by the "Taverne" license above, please follow below link for the End User Agreement:


www.tue.nl/taverne

Take down policy

If you believe that this document breaches copyright please contact us at:

openaccess@tue.nl

providing details and we will investigate your claim.



Building up a
membrane photonics platform
in Indium phosphide

Josselin Pello

Building up a membrane photonics platform in Indium phosphide

PROEFSCHRIFT

ter verkrijging van de graad van doctor
aan de Technische Universiteit Eindhoven
op gezag van de rector magnificus, prof.dr.ir. C.J. van Duijn,
voor een commissie aangewezen door het College voor Promoties
in het openbaar te verdedigen op
donderdag 13 februari 2014 om 16.00 uur

door

Josselin Pello

geboren te Boulogne-Billancourt, Frankrijk

Dit proefschrift is goedgekeurd door de promotor en de samenstelling van de promotiecommissie is als volgt:

voorzitter: prof.dr.ir. A.C.P.M. Backx
promotor: prof.dr.ir. M.K. Smit
copromotor: dr. J.J.G.M. van der Tol
leden: prof.dr. V. Pruneri (Institute of Photonic Sciences - ICFO)
prof.dr.ir. G.C. Roelkens (Ghent University - IMEC)
prof.dr. A. Fiore
prof.dr. H.J.S. Dorren
dr.ir. L.M. Augustin

A catalogue record is available from the Eindhoven University of Technology (TU/e) Library.

The research presented in this thesis was supported by the TU/e High Potential Research Program, and carried out in the Photonic Integration group, at the Department of Electrical Engineering of TU/e, the Netherlands.

Building up a membrane photonics platform in Indium phosphide, by Josselin Pello

ISBN: 978-94-6259-049-6

Copyright © 2013 Josselin Pello

Typeset using LyX

Printed in the Netherlands, by Ipskamp Drukkers



Être heureux, c'est un travail à plein temps :)

Being happy is a full-time job :)

Contents

1	Introduction	1
1.1	Merging photonics and electronics	1
1.2	Membrane photonics	2
1.3	Outline of this thesis	3
2	The IMOS platform	5
2.1	The IMOS concept	5
2.1.1	Membrane specifics	5
2.1.2	Building blocks	6
2.1.3	Active-passive integration techniques	9
2.2	IMOS simulation tools	11
2.3	IMOS Fabrication	11
2.4	IMOS Characterization setup	14
2.5	Conclusion	17
3	Waveguide loss properties	19
3.1	Loss mechanisms	19
3.1.1	Scattering loss	19
3.1.2	Material-induced losses	20
3.2	Loss measuring structures	22
3.2.1	Waveguides of different lengths	22
3.2.2	Ring resonators	23
3.2.3	Mach-Zehnder interferometers (MZIs)	26
3.3	Loss reduction strategies	29
3.3.1	Thermal reflow of the ZEP pattern	30
3.3.2	Dielectric overcladding	31
3.3.3	ZEP/C ₆₀ composite resist	32
3.4	Conclusion	33
4	A ring-based memory element	35
4.1	Phase-change materials (PCMs)	36
4.2	Design	39
4.3	Fabrication	43
4.4	Characterization	44
4.4.1	Optical switching setup	44

4.4.2	Switching parameters determination	45
4.4.3	Results	47
4.5	Conclusion	50
5	A Polarization conversion device	51
5.1	Design	52
5.1.1	Principle	52
5.1.2	Design optimization	53
5.1.3	Wavelength behavior and tolerances	55
5.2	Fabrication	57
5.2.1	Process-flow	57
5.3	Characterization	61
5.3.1	Characterization technique	61
5.3.2	Results	62
5.3.3	Conclusion	65
6	Wavelength selective components	67
6.1	Distributed Bragg Reflectors (DBRs)	67
6.1.1	Design	68
6.1.2	Fabrication	69
6.1.3	Characterization	70
6.1.4	Conclusion	73
6.2	Wavelength demultiplexers	74
6.2.1	Arrayed Waveguide Grating (AWG)	74
6.2.2	Planar Concave Grating (PCG)	75
6.2.3	Conclusion	81
7	The POLIS active-passive integration scheme	83
7.1	POLIS Material analysis	83
7.1.1	POLIS principle	83
7.1.2	POLIS layer-stack	84
7.1.3	Photoluminescence (PL)	85
7.2	Laser design	87
7.2.1	Laser principle	87
7.2.2	Optically pumped lasers	88
7.2.3	Electrical pumping and contacting	90
7.3	Experimental results	93
7.3.1	Fabrication	93
7.3.2	First IMOS laser	95
7.4	Conclusion	97
8	Conclusions and outlook	99
8.1	Conclusions	99
8.2	Outlook and recommendations	100
	Bibliography	103

List of Abbreviations	109
Summary	111
Acknowledgments	113
List of Publications	115
Curriculum Vitae	117

Chapter 1

Introduction

The word “photonics” is derived from the Greek word “photos” meaning light. According to the French scientist Pierre Aigrain, who coined the word in 1967, “photonics encompasses the generation of light, the detection of light, the management of light through guidance, manipulation, and amplification, and most importantly, its utilization for the benefit of mankind.”

1.1 Merging photonics and electronics

Since the advent of the integrated circuit (IC) in 1958, electronic chips have revolutionized our society. They are present in every digital appliance from computers and mobile phones to watches and cars. The extraordinary success of the IC industry comes from its scalability. As the technology used to manufacture ICs started to improve, the density of components integrated on single chips doubled about every two years. This trend, known as Moore’s law, has since been used by the semiconductor industry as a roadmap to determine the characteristics of consecutive generations of ICs. Thanks to the increase in transistor density, individual ICs could be made smaller, faster and mass-produced on large wafers, making high-end technology goods increasingly powerful and affordable for consumers.

The IC industry is supporting innovation, and is a key driver for economic growth. In 2004, the IC industry market was worth 160 billion euro worldwide, while the electronics sales and services directly enabled by the IC industry represented close to 10 % of the world’s GDP.

However, integration on ICs has now become so dense that the associated power consumption threatens to prevent the performance improvements usually obtained from miniaturization. This limit is known as the interconnect bottleneck, be-

cause most of the energy dissipation in ICs doesn't originate from the logic switching, or from storing information in memory cells, but from the interconnection between different components [1]. In fact, microprocessors in current computers are already running below the theoretically obtainable clock speed, because faster operation would make the chip dissipate too much heat [2]. In order to continue improving the overall system speed, multi-core processors had to be introduced. Furthermore, at several percent of the global electric power consumption, the overall energy consumption of information and communication technologies is becoming ecologically significant [3]. Therefore, any way of reducing the power consumption of ICs is very important.

A solution proposed to overcome the interconnect bottleneck is the use of optical on-chip interconnects (cf. Fig.1.1). Light has some intrinsic advantages compared to electricity in terms of information density (thanks to the use of multiple wavelengths) and signal integrity, such as improved timing precision, reduced reflection, reduced cross-talk and voltage isolation [1]. But more importantly, it is not subjected to the capacitive charging and discharging effects which cause most of the power dissipation in electrical lines. Therefore, optical interconnects have potentially an energy benefit compared to electrical interconnects. In order to exploit this advantage, optical transmitters and receivers with low energy consumption and good performance at low optical power must be designed, and integrated together with the electronic IC.

Conversely, future photonic devices such as sensors or optical data communication components need to be scaled down together with the electronics driving them in order to reduce their fabrication costs, power consumption and final size. Therefore, it is clear that electronics and photonics can both greatly benefit from co-integration on the same chip.

1.2 Membrane photonics

The best option for realizing a photonic integrated circuit (PIC) on top of electronic chips, is membrane photonics. A photonic membrane is a thin (typically a few 100 nm thick) layer of high refractive index material surrounded above and below by low-refractive index materials. Thanks to the high vertical refractive index contrast created in such a structure, light is tightly confined in the high refractive index material. This allows for narrow waveguides ($\sim 0.5 \mu\text{m}$ wide), tight bends ($\sim 5 \mu\text{m}$ radius) and generally very compact photonic devices to be realized in the membrane, and combined into high-density, low-power circuits.

Different materials and processes can be considered to create such membranes. Because of its relative degree of compatibility with the mature complementary metal-oxide-semiconductor (CMOS) technology used to manufacture most electronic ICs, Silicon-On-Insulator (SOI) is considered a suitable platform for optical interconnect applications. Many high-quality photonic components [4], as well as low-loss waveguides [5, 6], have already been demonstrated on SOI. However, because of the indirect bandgap of silicon, SOI circuits cannot easily integrate the optical sources and amplifiers necessary for generating and maintaining the optical signals in PICs. In general, lasers and optical amplifiers on SOI are realized by heterogeneous inte-

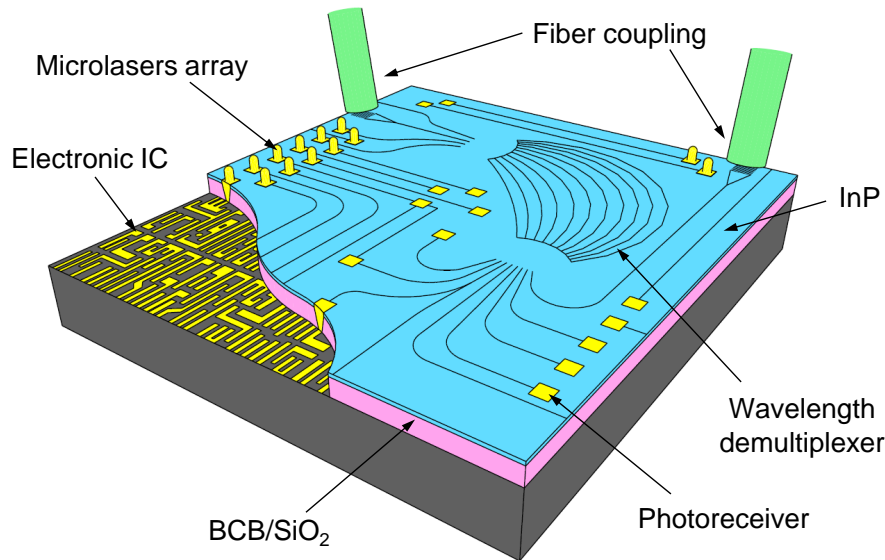


Figure 1.1: Schematic representation of an InP-membrane on Silicon (IMOS) optical interconnect integrated on top of an electronic integrated circuit (IC). The high refractive index contrast between the InP membrane (in blue) and the air and BCB/SiO₂ stack (in pink) enables the fabrication of compact and low-power photonic devices connected to the underlying IC by vias.

gration of III-V gain materials [7].

A membrane platform fully based on III-V materials can integrate both active and passive components in a single layer, thereby simplifying the fabrication process of PICs. Recently, several low-power consumption active devices, including electrically-pumped lasers [8] and switches [9] have been demonstrated in III-V-material-based membranes. We have demonstrated a number of high-quality passive components, including power splitters and ring resonators, in such a platform, called InP-Membrane-on-silicon (IMOS) [10]. In this thesis, the development of this platform is described.

1.3 Outline of this thesis

The aim of this work is to develop the Indium phosphide-based membrane photonics platform IMOS, with optical on-chip interconnects as the main long-term application. For this purpose, a number of building blocks are necessary to generate, guide and control light in IMOS integrated circuits. The thesis describes how these building blocks are designed and fabricated.

Chapter 2 contains a detailed description of the IMOS platform concept, software tools, fabrication technology, and characterization technique. The information given in this chapter will be useful for the understanding of the results presented in the remaining of the thesis.

In **Chapter 3**, the main loss mechanisms relevant for the IMOS platform are described. Structures that enable measurement of the propagation loss of waveguides are then presented, and a discussion of several techniques used to reduce this loss is

given.

In **Chapter 4**, the first optical memory element integrated on a photonic platform using phase-change material is presented. This device is based on a microring resonator partially covered with a phase-change material, which can be switched in a fast, reversible and non-volatile way. It can be used to create memory functionality in IMOS or SOI, as well as for the trimming of certain parameters in realized circuits.

The device presented in **Chapter 5** is used to convert the polarization of signals in IMOS circuits from TE to TM and vice versa. It is based on a new fabrication concept, resulting in the world's smallest polarization converter made to date in InP. It can be used for the implementation of polarization-diversity schemes, light intensity modulation or polarization bit interleaving applications in IMOS.

In **Chapter 6**, two new IMOS wavelength-selective devices are introduced. The first, a distributed Bragg reflector (DBR), can be used for wavelength filtering or to build laser cavities, as shown in the following chapter. The second is a planar concave grating demultiplexer, to be used for efficient wavelength demultiplexing (WDM) signal processing, or in multi-wavelength lasers.

The purpose of **Chapter 7** is to explore the potential of a polarization-based active-passive integration scheme (POLIS) in IMOS. In the process, we will describe the first laser prototype successfully fabricated in IMOS.

Finally, **Chapter 8** summarizes the main achievements of the thesis and gives an outlook and recommendations for the future of IMOS.

Chapter 2

The IMOS platform

This chapter is designed to give the reader a more detailed understanding of the IMOS platform concept, software tools, fabrication technology, and characterization technique. The information given in this chapter will be useful for the understanding of the results presented in all the following chapters.

2.1 The IMOS concept

The IMOS platform is based on a high refractive index contrast composition, which makes it suitable for the creation of high-density, low-power PICs. In the long term, we want all the useful functionalities of PICs to be easily integratable in IMOS, using a set of standard building blocks. Finally, the strength of IMOS resides in its inherent ability to integrate active and passive functions. All these points are addressed in the following paragraphs.

2.1.1 Membrane specifics

Fig.2.1 represents the typical dimensions and composition of an IMOS chip. InP ($n = 3.17$) is chosen as the high refractive index wave-guiding material, because of its ability to integrate lattice-matched active and passive materials. The low-refractive index ($n = 1.5$) polymer Benzo-Cyclo-Butene (BCB) is used as an adhesive to bond the InP membrane to a Silicon wafer. The thickness of the InP membrane is chosen as ~ 250 - 300 nm to obtain a strong light confinement, while a bonding layer thickness of $1.9 \mu\text{m}$ enables to optically decouple the InP membrane from the high-refractive index silicon wafer.

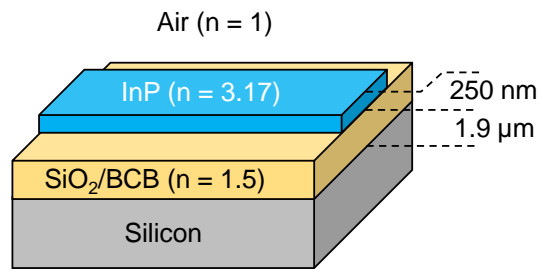


Figure 2.1: Schematic composition of an IMOS chip.

This configuration brings a number of advantages:

- First, as demonstrated in the mature technology of bulk InP-based photonics [11], the use of InP and related compounds as the guiding material simplifies the integration of passive and active functions on the platform. The SOI platform, by comparison, requires a hybrid approach to create active devices.
- Second, thanks to the high vertical refractive index contrast created in IMOS, light is tightly confined in the InP membrane. This allows for very compact photonic devices to be realized in the membrane. Consequently, circuits in IMOS can be made very dense, and with low power consumption. The basic building block for light guiding, for instance, is a single-mode waveguide with a cross-section of 250 nm × 450 nm, more than one order of magnitude smaller than single-mode waveguides in bulk InP-based photonics.
- Finally, the use of a polymer (BCB) as the bonding material brings a relatively high degree of flexibility with regard to the carrier wafer composition and topology. In terms of integration of an IMOS optical interconnect on top of an electronic IC, this means that back-end processing can be used, limiting the interference with the CMOS fabrication to the connections between IMOS and CMOS devices using vias.

Once the platform composition has been chosen, the next step is to design a set of basic building blocks, which can be combined to realize complex functions in PICs. Ideally, these building blocks should be brought together in a single generic integration process, optimized for providing high performance for all the building blocks [11].

2.1.2 Building blocks

Most functions in PICs can be realized with just four types of basic components: passive waveguides, and devices to control the polarization, phase and amplitude of optical signals [11]. In the next paragraphs, we describe these basic components and show how they can be combined to create all the main building blocks considered in the IMOS platform.

Waveguides

In PICs, waveguides are typically rectangular structures which guide optical waves by total internal reflection. Primarily, waveguides are used for transporting signals between different points of the circuit. They can be straight or bent, and thus can connect together any points of the circuit. One of the most important property of waveguides is their propagation loss, which Chapter 3 will cover in detail.

Power splitters

When waveguides are wide enough to support several lateral modes, they can also be used to create high-efficiency multi-mode interference (MMI) couplers and splitters. In MMI devices, the velocity difference between the different supported optical modes is exploited to create single or multiple images of the input field at certain periodic intervals along the propagation direction of the light. By correctly choosing the length of the MMI section, one can efficiently split the power coming from a single-mode waveguide, into two output single-mode waveguides. In IMOS, we have realized 1×2 MMI splitters as small as $2 \mu\text{m} \times 3.1 \mu\text{m}$ [12].

Filters

A simple way of realizing wavelength filtering is by using ring resonators. A ring resonator consists of a waveguide looped back on itself, and coupled to one or more adjacent waveguides. Input light coming from one of the adjacent waveguides is partially coupled into the ring, while experiencing a 90° phase-shift. If the optical length of the ring is an integer multiple of the wavelength of the light, there will be destructive interference between the light which has made one round-trip in the ring and couples back into the adjacent waveguide, and the light coming directly from the adjacent waveguide. Therefore, at the wavelengths matching this condition, light is suppressed in the adjacent waveguide and trapped in the ring, leading to a drop in the adjacent waveguide's transmission. More detail about the theory of ring resonators can be found in Section 3.2.2.

Memory elements

A very desirable feature in a photonic platform is the ability to write, store and read data. Non-volatile memories, in which the data is maintained even when no power is supplied, are of special interest to create low-power consumption PICs. In Chapter 4, we will describe a non-volatile memory element based on a ring resonator and a phase-change material.

Phase and amplitude modulators

Electro-optic phase modulators are commonly used to control the phase of the light, by changing the refractive index of a material using an electric field. A phase modulator can be used in combination with MMI couplers in a Mach-Zehnder interferometer (MZI) configuration in order to create an amplitude modulator.

Reflectors

Another important building block for IMOS is a reflector. This device is of particular interest for creating optical cavities where lasing can occur. Reflectors can be created by varying periodically one parameter of a waveguide along the propagation direction. These are called distributed Bragg reflectors (DBRs), and will be described in more detail in Section 6.1.

Polarization converters

Polarization handling is a very important function in PICs. In high refractive index contrast platforms like IMOS in particular, the propagation properties of the TE and TM polarized modes often differ strongly. Therefore, most devices only function well for a single polarization. A polarization diversity scheme is then required in order to process the orthogonally polarized light [13]. In Chapter 5, we will describe a polarization converter used for efficient TE to TM conversion, based on triangular waveguides. This device can be combined with other building blocks to create polarization splitters, switches and wavelength converters [14].

Wavelength demultiplexers

One of the main advantages of optical signal processing over its electrical counterpart, is that optical signals of different wavelengths can propagate in the same material without interference. In order to benefit from this property in IMOS, wavelength (de)multiplexing devices are required. In Section 6.2.2, a wavelength demultiplexer created by combining waveguides and DBR reflectors will be described.

Semiconductor Optical Amplifiers (SOAs)

When signals are attenuated by propagation loss, semiconductor optical amplifiers (SOAs) are used to amplify them. Using the process of stimulated emission, photons traveling through a gain material supplied with energy can stimulate the emission of new photons identical to themselves. SOAs can be used to create among others wavelength converters, ultra-fast switches, and lasers.

Lasers

If an SOA is placed in an optical cavity and supplied with energy, light can be amplified during each round-trip through the cavity. Above a certain pumping power (the lasing threshold), the light amplification becomes larger than the cavity losses. The power of the recirculating light can then rise exponentially, making the device *lase*. Lasers are crucial components of PICs, since they supply the chip with the light necessary to function. In Section 7.3.2, we will present an optically pumped IMOS laser.

Photodetectors

Optical signals propagating in PICs must sometimes be converted into the electronic domain. For this, photodetectors are used. Typically, an SOA in reverse bias will generate an electronic signal dependent on the number of photons it receives and

absorbs. The most important parameters of a photodetector are its responsivity, and its bandwidth.

Input/output couplers

The last important function which needs to be integrated in IMOS is the coupling of light in and out of the IMOS chip. Due to the large mismatch between the IMOS membrane thickness (~ 300 nm), and the diameter of the optical mode in standard single-mode fibers (~ 10 μm), butt-coupling is extremely inefficient for coupling light in and out of IMOS chips. To overcome this problem, one option is to use mode-size converters. However, mode-size converters create a large topography on the chip surface, occupy a large footprint and can only be placed on the chip edges. Another option is to use grating-couplers. These can be printed in the membrane plane in a single etch step, and placed anywhere on the chip, allowing wafer-scale testing [15]. The main limitation of grating-couplers is their bandwidth (FWHM ~ 60 nm), their polarization dependence (they only work for one polarization), and their less than 100 % coupling efficiency.

In order to integrate all of the previously mentioned building blocks together in IMOS, an efficient active-passive integration scheme has to be used. In this way, the passive devices (such as waveguides, polarization converters and wavelength demultiplexers) can connect seamlessly with the active devices (lasers, detectors, modulators, etc.).

2.1.3 Active-passive integration techniques

As depicted in Fig. 2.2, we are currently investigating three schemes for active-passive integration in IMOS.

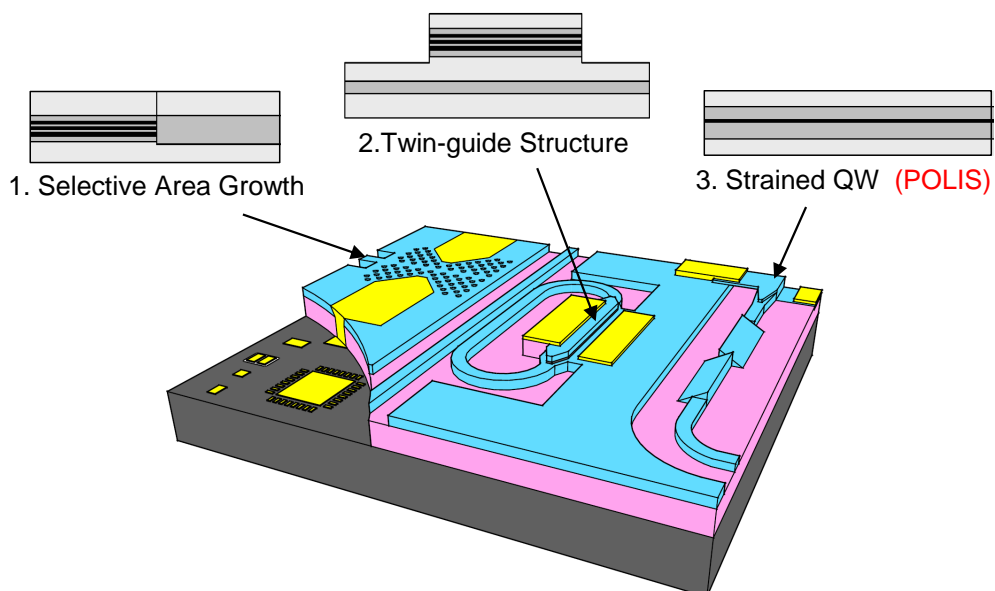


Figure 2.2: Schematic representation of the three IMOS active-passive integration schemes currently being developed.

1. The first scheme is based on selective-area regrowth, or butt-joint integration. An active layer-stack containing a gain material is grown on an InP substrate. This gain material is then locally etched away from the areas where it is not needed, and replaced by passive material, using a regrowth process. In our group, quantum well (QW) active regions have been successfully integrated with Q1.25 passive material [10]. This is a proven technology for conventional InP-based integration technology, and it has also been recently demonstrated in membranes [16].
2. The second active-passive integration scheme relies on so-called twin-guide structures (cf. top diagram in Fig. 2.2). In such a scheme, passive and active layers are grown on top of each other, in a single epitaxy. The active layers are removed from the areas where passive devices are to be printed, but retained in areas where gain or absorption is needed. In the latter, the optical mode overlaps with both the passive and active layers (or adiabatic tapers are used to couple the light between these layers). With this method, problems due to regrowth are avoided. However, optical coupling between passive and active sections is more complex, since it needs to be controlled both in the lateral and in the vertical directions. The topography created in this scheme during fabrication can also complicate further processing.
3. A third approach, called the POLarization-based Integration Scheme (POLIS), relies on the polarization behavior of specially designed strained QWs [17]. The strain induced by the lattice mismatch between the QW and the surrounding semiconductor material leads to a separation of the light hole and heavy hole subbands in the valence band. As a consequence, there is a wavelength range in which the QW absorbs TE polarized light while transmitting TM polarized light. Using the polarization conversion device described in Chapter 5, it thus becomes possible to easily connect passive waveguides and passive devices to devices requiring gain (amplifiers, lasers) or absorption (detectors). As in the twin-guide scheme, the semiconductor material can be grown in a single epitaxy, avoiding all problems related to regrowth. However, POLIS offers the superior advantage of keeping the optical mode in a single plane. The main drawbacks of this scheme are the limited optical bandwidth of the effect, the implicit polarization dependence of the circuit, and the need to integrate in the circuit compact and efficient polarization converters with a very low reflectivity.

On the longer term, we expect that butt-joint integration will prove to be the most flexible integration technology. In this thesis, however, we have focused on the POLIS integration scheme (cf. Chapter 7), because the regrowth technology for butt-joint integration in membranes was not yet available in COBRA. Furthermore, the POLIS scheme connects smoothly with the processing developed for the polarization converter (Chapter 5), and from a scientific point of view it is more novel. Most of the processing that we developed can be used in all three integration schemes.

In the next sections, we describe successively the simulation tools used for the design of IMOS devices, the process-flow used for the fabrication of IMOS chips, and the setup used to characterize them.

2.2 IMOS simulation tools

The design of IMOS devices relies on different pieces of software. The most important ones are the mode solver FIMMWAVE, and the eigenmode expansion tool CAMFR.

FIMMWAVE/FIMMPROP

FIMMWAVE is a generic, robust, fully vectorial mode finder for 3D waveguide structures. Among others, the FMM Solver, based on the mode matching method, is optimized for rectangular geometry waveguides such as epitaxially grown structures. It is fully vectorial, and capable of solving structures with complex refractive index (such as metallic components and waveguides with gain). FIMMPROP is the EigenMode Expansion method propagation tool integrated in FIMMWAVE.

The mode solver of FIMMWAVE was used extensively in the design of the memory device presented in Chapter 4, to calculate the effective index and absorption coefficient of the modes in Si waveguides covered with an absorbing material. It was also used together with FIMMPROP to determine the lengths of the triangular waveguide sections leading to full TE to TM conversion in the polarization converter described in Chapter 5. Finally, 1×2 MMI couplers were also simulated using this tool.

CAMFR

CAMFR (CAvity Modelling FRamework) is a fast, flexible, friendly full-vectorial Maxwell solver. Its main focus is on applications in the field of nanophotonics [18]. It is based on a combination of eigenmode expansion and advanced boundary conditions like perfectly matched layers (PML). CAMFR is an ongoing active research project, started at the photonics group of the Department of Information Technology (INTEC) at Ghent University in Belgium.

In this work, CAMFR was used to design the grating-couplers enabling coupling in and out of IMOS chips, as well as the DBR reflectors (cf. Section 6.1). Although CAMFR can only model 2D Cartesian structures, the simulation results are found to be very reliable and match the measurements well.

2.3 IMOS Fabrication

Standard IMOS passive devices are fabricated in a 250 to 300 nm thick InP membrane bonded to a silicon (or sometimes glass) carrier wafer. The first devices demonstrated in IMOS were processed before bonding, with the membrane still on the InP substrate [10]. However, some future IMOS chips with complex devices may require double-sided processing. Furthermore, creating single-sided IMOS circuits after bonding enables to select samples based on bonding quality. Therefore, a new fabrication scheme is developed, whereby devices are patterned after bonding the membrane. The IMOS post-bonding fabrication scheme used for standard passive devices is shown in Fig. 2.3 and explained below. More specific technologies (for the

memory element, the polarization converters and the POLIS scheme) will be given in other chapters.

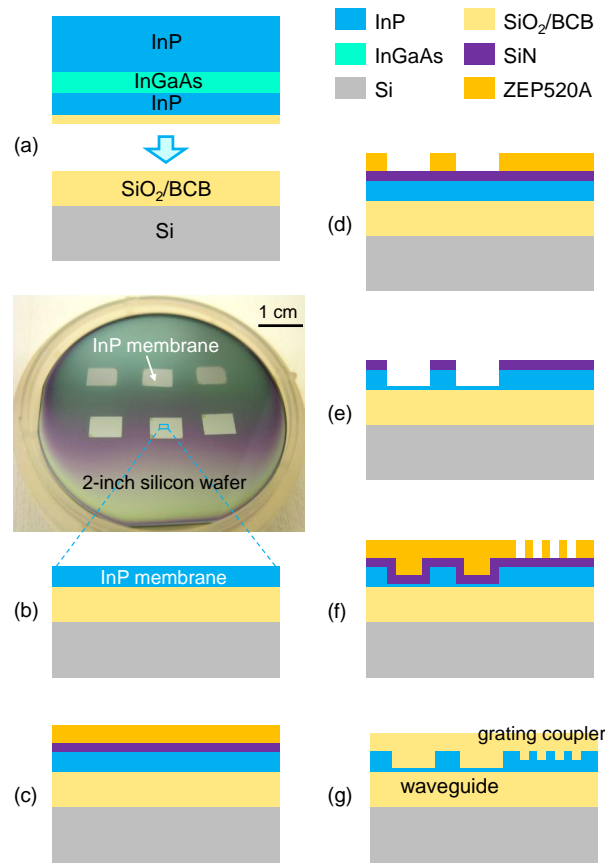


Figure 2.3: (a-g) Post-bonding process-flow used for fabricating standard IMOS passive devices. (b-inset) Photograph of six InP dies bonded simultaneously on a 2-inch silicon wafer.

- (a) The membrane is prepared by growing a two-layer stack (300 nm InGaAs / 300 nm InP) on an InP substrate. The 300 nm InP layer is the future membrane, whereas the InGaAs layer will be used as an etch-stop layer during the InP substrate removal after bonding. Thanks to the high selectivity of the etching solutions used in step (b), a thickness of 300 nm is sufficient for protecting the InP membrane, while etching the InP substrate. A 2-inch silicon carrier wafer is then cleaned and covered with a 1.5 μm thick SiO₂ layer deposited by Plasma Enhanced Chemical Vapor Deposition (PECVD). A die is cleaved from the previously mentioned InP layer-stack, and covered with a 350 nm thick SiO₂ layer to improve adhesion to BCB. This die is then flip-chip bonded to the silicon/SiO₂ carrier wafer, using a 50 nm thick BCB adhesive layer [19]. The use of such a thin BCB bonding layer, combined with the SiO₂ layers grown by PECVD enables to accurately control the thickness and

uniformity of the SiO₂/BCB stack between the InP membrane and the Silicon substrate. This is important to ensure a high-coupling efficiency of the grating-couplers.

- (b) The InP substrate and the 300 nm thick InGaAs etch-stop layer are then removed successively by selective wet etching (using 4HCl: 1H₂O, and 1H₂SO₄: 1H₂O₂: 10H₂O respectively), leaving the 300 nm thick InP membrane bonded on the Silicon carrier wafer, ready for the patterning of photonic devices.
- (c) IMOS devices are fabricated in this membrane using two e-beam lithography (EBL) steps, to define consecutively deeply (250 nm) and shallowly (120 nm) etched regions. First, a 50 nm thick SiN layer is deposited on the membrane by PECVD, and a layer of ZEP520A (ZEP) e-beam resist is spin-coated on top of it. The choice of ZEP as the e-beam resist is motivated by its high resolution, and by its strong resistance in the Reactive Ion Etching (RIE) process used to transfer the pattern to the SiN layer. In the future, adding C₆₀ molecules to ZEP may improve the EBL quality (cf. Section 3.3.3).
- (d) The first EBL step is then used to define simultaneously the devices, the trenches around the access waveguides, and local markers to which the second EBL can be precisely aligned. An important step following the development of the exposed ZEP pattern is a reflow bake of 2'00" at ~ 154 °C (cf. Section 3.3.1). This step enables to soften the roughness in the pattern, and reduce the final roughness in the fabricated devices.
- (e) The exposed pattern is transferred from the ZEP layer to the SiN layer using a pure CHF₃ RIE process, and subsequently from the SiN layer to the InP membrane, using a CH₄-H₂ RIE process. Note that the RIE etching time is controlled to leave a 50 nm footing in these deeply etched regions. This prevents under-etching of the SiO₂ cladding and BCB adhesion loss, during the subsequent SiN removal in BHF.
- (f) In order to define the shallowly etched regions (e.g. the grating couplers), the SiN layer is replaced with a fresh one, and the same EBL procedure is repeated, albeit with a shorter etching time in the final InP RIE etching.
- (g) Once all the structures are fabricated, the SiN layer is removed in BHF, and a 300 nm thick SiO₂ over-cladding is deposited on the membrane, to reduce the effect of sidewall roughness on waveguide losses (cf. Section 3.3.2).

In the following section, we describe the grating-coupler setup used to characterize the realized IMOS chips.

2.4 IMOS Characterization setup

As mentioned at the beginning of this chapter, the solution chosen for in and out-coupling of light in IMOS chips is the use of grating-couplers. This device is a periodic structure designed to diffract the light coming from a fiber placed on top of it, into the horizontal plane of the chip (cf. Fig.2.4).

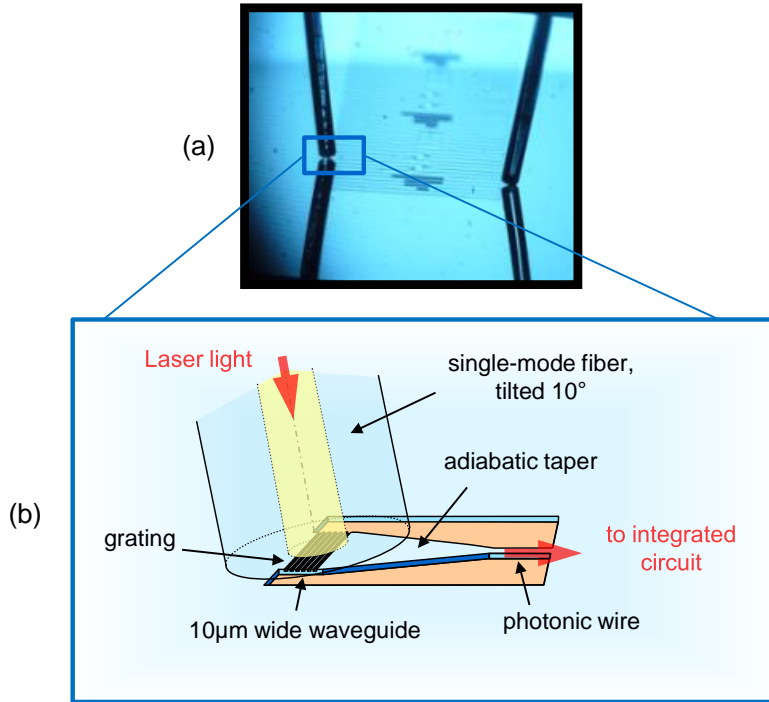


Figure 2.4: (a) Photograph of two fibers used to characterize an IMOS photonic circuit. (b) Schematic of the coupling of light from a single-mode fiber into a photonic integrated circuit, using a grating-coupler.

The grating-coupler is $10\ \mu\text{m} \times 10\ \mu\text{m}$ in size, and converts the fiber mode ($\sim 10\ \mu\text{m}$) into a $\sim 10\ \mu\text{m}$ wide mode in the InP membrane. An adiabatic taper can then be used to laterally convert this mode into the fundamental mode of a single-mode 450 nm wide IMOS photonic wire. In this case, a linear taper length of 300 μm is required for adiabatic conversion. As demonstrated on SOI [15], curving the grating grooves in the proper way allows to create a focusing grating-coupler, with a total length (grating-coupler + taper) of just 30 μm . By virtue of the reciprocal propagation of light, a grating-coupler can also be used in the reverse configuration, to couple light from the photonic integrated circuit into the fiber.

In this work, grating-couplers are designed using CAMFR. Fig.2.5(a) shows the result of the 2D simulation of an IMOS grating-coupler. Light is initially coming from the InP waveguide on the left. As light propagate to the right, the corrugation of the grating-coupler diffracts the light upwards and downwards. The grating period is chosen in order for the diffracted field to be at 10° with respect to the direction normal to the surface. This will ensure that the light is coupled in the right direction when the grating-coupler is used in the in-coupling configuration.

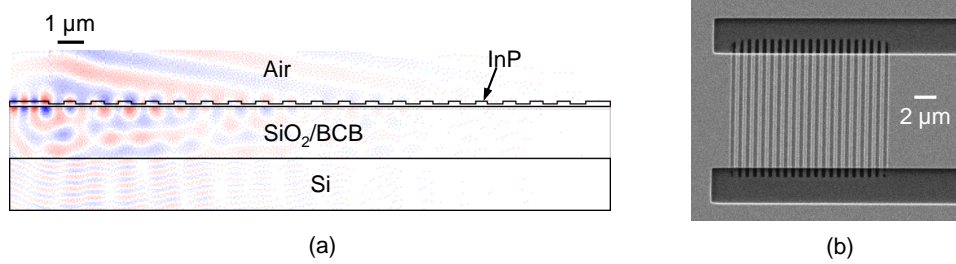


Figure 2.5: (a) Lateral view of a grating-coupler simulated using CAMFR. (b) Top-view SEM picture of a grating-coupler fabricated in IMOS.

As seen on this simulation plot, the intensity of the diffracted wave is highest at the beginning of the grating and decreases exponentially along the grating. The overlap between the Gaussian mode profile of the optical fiber and the diffracted field is therefore not perfect, which limits the theoretical coupling efficiency between fiber and chip to about -1 dB.

Furthermore, a significant fraction of the light is diffracted downwards by the grating. Part of this light is lost in the Silicon substrate, but a careful choice of the SiO₂/BCB stack thickness will ensure that the fraction of the light reflected by the Silicon surface interferes constructively with the light diffracted upward by the grating, and can be collected by the fiber. In practice, fabricated grating-couplers have a typical coupling efficiency of about -5 dB [15].

A photograph of the standard grating-coupler setup used to characterize passive IMOS devices is shown in Fig.2.6. The different elements of this setup have the following functions:

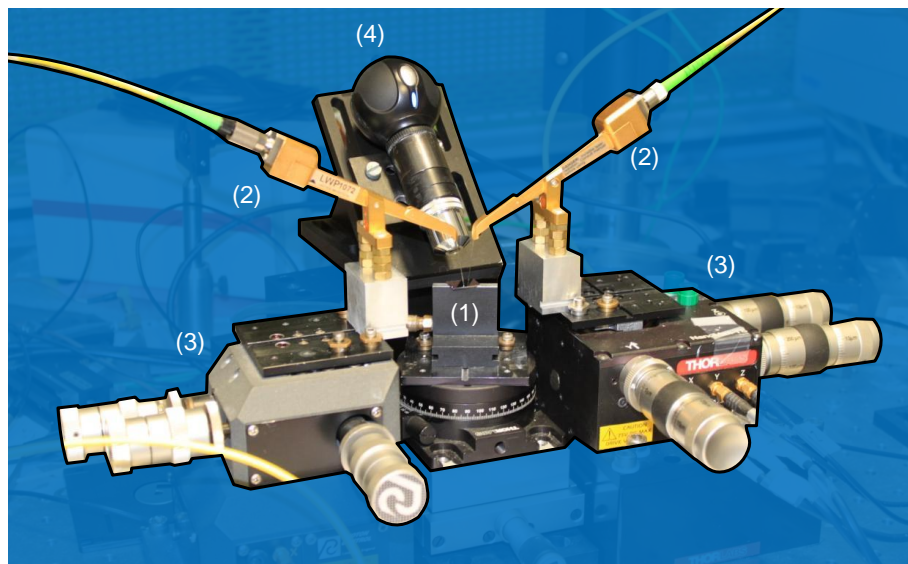


Figure 2.6: Photograph of the grating-coupler setup used to characterize passive IMOS devices. (1) Vacuum chuck, (2) Fiber holders, (3) Micropositioners, (4) Alignment camera.

(1) Vacuum chuck The sample is kept in place on a vacuum chuck.

- (2) Fiber holders** Most grating-couplers are designed to couple the desired wavelength in or out of the chip for an angle of $\sim 10^\circ$ between the fiber and the direction normal to the sample surface. Fiber holders are used to maintain the tips of the fibers at that angle throughout the measurements, while connecting the other ends to the relevant equipment such as a source (e.g. tunable laser, or erbium-doped fiber amplifier (EDFA)) or a detector (e.g. power-meter, or optical spectrum analyzer (OSA)).
- (3) Micropositioners** In order to finely tune the positions of the fibers, the fiber holders are fixed on 3-axis micropositioners.
- (4) Alignment camera** Coarse alignment of the fibers with respect to the on-chip grating-couplers is achieved using a camera placed at $\sim 45^\circ$ relative to the sample surface. Fig.2.4(a) shows a typical image recorded by the camera during device characterization. In and out-coupling fibers can be seen on the image, as well as their reflections on the sample surface, providing an indication of the distance between the fibers and the sample. The resolution of the camera must be high enough to distinguish individual devices on the chip, so that the fibers can be aligned to the corresponding grating-couplers. In our setup, the camera is composed of a webcam connected to a $7\times$ microscope objective using a tube of ~ 5 cm length. Once the fibers have been coarsely aligned to the grating-couplers using the alignment camera, the operator is usually able to observe a transmitted signal through the setup. The micropositioners are then adjusted successively to maximize the power of the detected signal, until the in and out-coupling fibers are properly aligned.
- (-) Polarization controller** When using an external laser as the source, a polarization controller (not pictured in Fig.2.6) is always added between the laser and the fiber holder in order to match the polarization state of the input light with the designed operating polarization of the grating-coupler. This is also achieved by optimizing the transmission of the signal through the whole setup.

Grating-couplers are designed using the eigenmodes expansion simulation tool CAMFR [18]. In table 2.1, we sum up the dimensions of a few interesting grating-coupler designs for IMOS.

Memb.thick.	pol.	cladding	pitch	etch.depth	fill.fac.	buffer	efficiency
[nm]	-	-	[nm]	[nm]	[%]	[μ m]	[%]
300	TE	Air	664	120	50	1.9	40.3
	TM	Air	960	120	50	1.9	29.2
	TM	SiO ₂	870	120	50	1.9	31.0
250	TE	Air	680	100	50	1.9	48.5
	TM	Air	960	100	50	1.9	33.4

Table 2.1: Interesting grating-couplers for IMOS, simulated with CAMFR at $\lambda = 1550$ nm. “buffer” refers to the thickness of the BCB/SiO₂ bonding stack.

Fig.2.7 shows the measured coupling efficiency of a typical IMOS grating-coupler, as a function of wavelength. A maximum coupling efficiency of 31 % is obtained at $\lambda = 1550$ nm, and the FWHM (3-dB bandwidth) is 58 nm. This value is good enough for the purpose of this thesis. However, it can be increased using high-reflection coatings on the substrate side, or a semiconductor overlay in the grating [15], at the cost of extra processing steps.

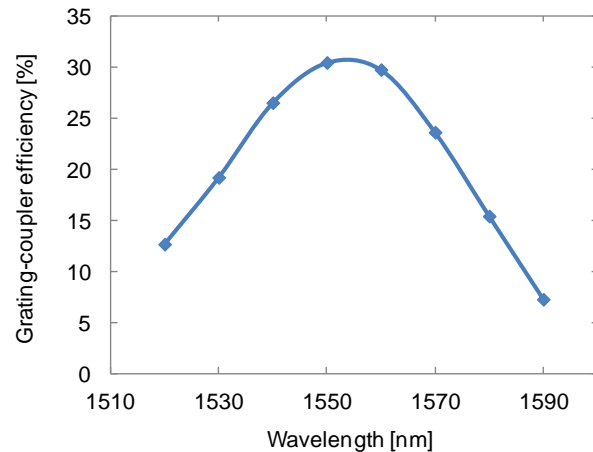


Figure 2.7: Measured coupling efficiency of an IMOS grating-coupler designed for TE polarization. (membrane thickness = 250 nm, period = 680 nm, etch depth = 100 nm)

2.5 Conclusion

The concept of the IMOS platform has been presented, showing its suitability for the integration of the active and passive building blocks required for realizing complex optical functions. The pieces of software useful for the design of IMOS devices have been mentioned. The process-flow presented in the third section of this chapter allows post-bonding processing of nanometer and micrometer-sized photonic devices in IMOS. Grating-couplers printed during this process-flow are used to couple light in and out of IMOS chips with efficiencies above 30 %.

In the next chapter, we give a detailed overview of the loss properties of IMOS waveguides realized and measured using the techniques described in this chapter.

Chapter 3

Waveguide loss properties

3

One of the most important issues in a photonic platform is the propagation loss of its waveguides. Waveguides are transporting signals between different points of the circuit. Due to propagation losses, the signals get attenuated, and eventually impossible to detect. Semiconductor optical amplifiers (SOA), are used to amplify signals and compensate for these propagation losses. However, SOAs increase the amount of noise in the signals, and need to be powered by an external source. Therefore, for a low-power photonic circuit, it is important to reduce the number of required SOAs, by minimizing the waveguide propagation loss.

In this chapter, we first describe the main loss mechanisms relevant for the IMOS platform. Then structures are presented that enable the measurement of the waveguide propagation loss, and results obtained with them are given. Finally, we discuss some techniques used to reduce the propagation loss in IMOS waveguides.

3.1 Loss mechanisms

Losses in semiconductor photonic waveguides are mainly of three types [20]: scattering loss, carrier-induced losses and losses caused by non-linear effects such as two-photon absorption (TPA). These three types of losses are described below.

3.1.1 Scattering loss

Scattering loss is the most basic and common source of waveguide loss. The propagation of light through a waveguide is based on total internal reflection of the wave at internal interfaces. If these interfaces are rough or irregular, light can be reflected in random directions, and lost from the waveguide. Therefore, in the IMOS fabrica-

tion process, a strong emphasis is put on reducing the waveguide roughness. Fig.3.1 shows the roughness created on the sidewalls of a waveguide during the IMOS fabrication process.

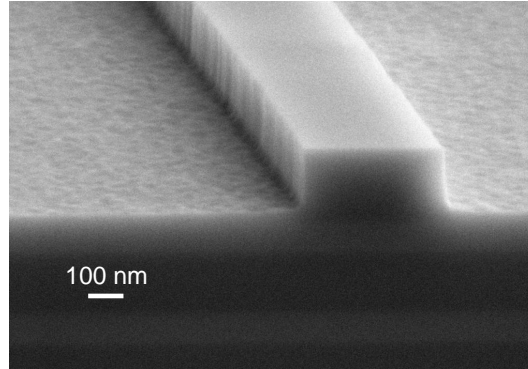


Figure 3.1: SEM picture of an IMOS waveguide (before bonding), showing sidewall roughness created during the fabrication process.

The scattering loss in an optical waveguide has been shown in ref.[21] to depend on the width of the waveguide core d , and the root-mean square σ of the roughness. According to this work, The upper boundary of this scattering loss can be written as:

$$\alpha_{\max} = \frac{16\sigma^2\kappa}{k_0d^4n_1}, \quad (3.1)$$

where k_0 is the propagation constant of the field in vacuum, n_1 the effective index of a slab with the same thickness as the core, and κ a factor dependent on the waveguide geometry and the statistical distribution of the roughness (for most practical waveguide geometries, $\kappa \simeq 1$). Since α_{\max} is inversely proportional to d^4 , scattering losses are much more harmful in IMOS waveguides than in bulk InP waveguides whose cross-section is much larger. For example, a roughness of only 3 nm can cause scattering losses of 3.3 cm^{-1} (14 dB.cm^{-1}) in a typical $250 \text{ nm} \times 450 \text{ nm}$ core single-mode IMOS waveguide (the effective index of a 250 nm InP slab is around $n_1 = 2.63$). For comparison, the scattering loss in a bulk InP/InGaAsP waveguide with the same roughness is less than 1 dB.cm^{-1} .

3.1.2 Material-induced losses

A second type of waveguide propagation loss arises due to the interaction of photons with the semiconductor material itself. The main material-induced loss are interband absorption and free-carrier (or intraband) absorption.

Interband absorption

Photons with energy greater than the bandgap energy of a semiconductor ($h\nu > E_g = E_C - E_V$) get absorbed very easily, by giving up their energy to raise electrons from the valence band to the conduction band. This effect is generally very strong, resulting in absorption coefficients larger than 10^4 cm^{-1} [20]. Therefore, the passive part of an IMOS circuit is always built in materials with a bandgap larger than the energy of

the wavelength of interest. Undoped InP, for instance, can easily be used for circuits operating in the C-band (1530 to 1565 nm) because interband absorption is almost nonexistent* for photon energies below the bandgap (~ 1.27 eV), corresponding to wavelengths longer than 980 nm

Free-carrier absorption

However, photons with energy lower than the bandgap ($h\nu < E_g$) can still be absorbed, due to free-carrier (or intraband) absorption. This process occurs when photons give up their energy to electrons already in the conduction band, or holes already in the valence band. As shown in [20], using the classical electromagnetic description of the motion of an electron in the presence of an applied oscillating electric field, the absorption coefficient α_{fc} due to free-carrier absorption can be shown to be equal to:

$$\alpha_{fc} = \frac{Ne^2\lambda_0^2}{4\pi^2n(m^*)^2\mu\epsilon_0c^3}, \quad (3.2)$$

with N the free carrier concentration (in cm^{-3}), e the elementary charge, λ_0 the wavelength of the light, n the refractive index of the material, m^* the (electron or hole) effective mass, μ the (electron or hole) mobility, ϵ_0 the vacuum permittivity and c the speed of light.

In the most general case, free-carrier absorption is thus proportional to the free carrier concentration N in the semiconductor material. This means that free-carrier absorption can cause high losses in the heavily doped layers used for electrical contacting of active devices. As a consequence, when designing active devices such as lasers and amplifiers, it is very important to reduce the overlap of the optical mode with the doped contact layers.

For p-type materials, there is also another loss mechanism called intervalence-band absorption. This mechanism occurs when photons are absorbed due to transitions between the split-off band and the heavy-hole or light-hole subbands of a semiconductor.

The free-carrier absorption of a semiconductor is sometimes described using a parameter called the absorption cross-section. For a p-doped material for instance, the absorption cross-section s_p (in cm^2) links the free-carrier absorption coefficient α_{fc} to the doping level p (in cm^{-3}) by the formula:

$$\alpha_{fc} = s_p \times p. \quad (3.3)$$

A typical value for the absorption cross-section of p-doped InP at $\lambda = 1535$ nm is $s_p = 2.2 \times 10^{-17} \text{ cm}^2$ [22].

Two-photon absorption (TPA)

In addition to interband, free-carrier absorption, and intervalence-band absorption, a non-linear effect known as two-photon absorption (TPA) can also create unwanted

*In reality, the Urbach tail absorption effect means that photons with energies below the bandgap can still be absorbed by interband absorption. However, this effect depends exponentially on the photon energy, and is thus limited to photon energies close to the bandgap.

loss in waveguides. TPA is the absorption of two photons of identical or different frequencies causing the excitation of an electron-hole pair. Since it requires two photons to coincide in time and space, this phenomenon only appears at relatively high optical powers. In fact, the rate of TPA can be shown to be proportional to the square of the light intensity [23]. This follows from probability analysis: the chance that two particles interact is linearly dependent on the concentration of both, so the dependence of TPA is quadratic with the photon concentration.

In IMOS, where the strong optical confinement leads to high power densities in waveguides, TPA can become problematic in high-power devices such as lasers, because it both wastes light and generates unwanted heat.

3.2 Loss measuring structures

3.2.1 Waveguides of different lengths

Scattering loss and carrier-induced losses attenuate the signal exponentially as a function of the propagation length (following a trend known as Lambert-Beer's law). Therefore, when measuring the transmission of an IMOS waveguide of length L , the power P_{in} coming from the source is related to the power P_{out} measured by the detector by the formula:

$$P_{\text{out}} = P_{\text{in}} \times C_{\text{coupling}}^2 \times \exp(-\alpha L) \quad (3.4)$$

where α (in cm^{-1}) is the propagation loss coefficient in the waveguide, and C_{coupling} is the product of the fiber, grating coupler and taper transmissions (see Section 2.4).

Since only P_{in} , P_{out} and L are known, at least two transmission measurements on waveguides of different lengths are required to determine C_{coupling} and α . In practice, the more waveguides are measured, the higher the accuracy in the determined values of C_{coupling} and α . The traditional way of presenting the measurement data is to plot the transmission of the waveguides on a dB scale, $10 \log \left(\frac{P_{\text{out}}}{P_{\text{in}}} \right)$, as a function of their length L , and to fit the data by a linear function (see Fig.3.2). In this way, the slope of the linear fit directly gives α in dB per unit length, while the y-intercept gives 2 times the coupling efficiency in dB. In Fig.3.2, we show the measured transmissions through four IMOS waveguides of 100, 300, 500 and 700 μm length respectively. The fitting of the data yields a propagation loss coefficient of $\alpha = 25 \pm 2 \text{ dB}\cdot\text{cm}^{-1}$ and a coupling efficiency of $C_{\text{coupling}} = 5.8 \pm 1 \text{ dB}$.

The value of C_{coupling} is close to the average value obtained for grating couplers in other groups [15]. However the value of the propagation loss is too high for interconnect applications. Using the loss-reducing strategies described later in this chapter (see Section 3.3), it is possible to bring the value of α down to just $3.0 \pm 1 \text{ dB}\cdot\text{cm}^{-1}$.

Measuring the propagation loss using waveguides of different lengths is straightforward, however it takes a relatively large amount of space on the chip. Furthermore, it requires several measurements and is thus sensitive to variations in coupling efficiency when moving from one waveguide to the other. As shown in the two following sections, in order to circumvent these issues, losses can be measured by analyzing the

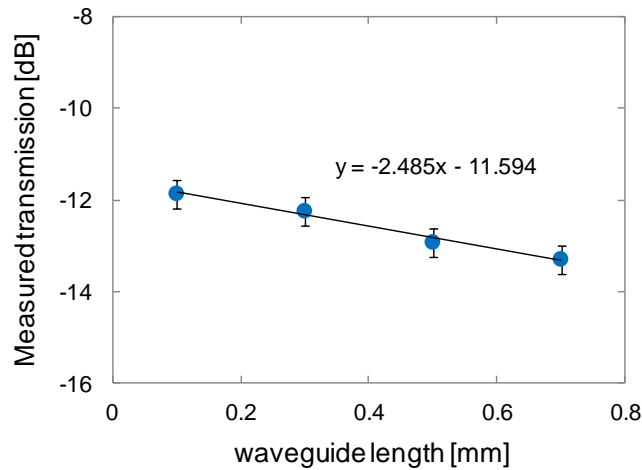


Figure 3.2: Determination of the waveguide propagation loss at $\lambda = 1550$ nm, using waveguides of different lengths.

transmission spectrum of a single device, such as a ring resonator or a Mach-Zehnder interferometer (MZI).

3.2.2 Ring resonators

Principle

Ring resonators are very versatile devices that have been applied to a large number of applications ranging from filters and optical delay lines to sensors and active rings for modulators and light sources [24]. As mentioned in Chapter 2, a ring resonator consists of a waveguide looped back on itself, and coupled to one or more adjacent waveguides. When the wavelength of the light traveling in an adjacent waveguide matches a resonance of the ring, a drop in the transmission of the adjacent waveguide is observed. As shown in the next paragraph, the transfer function of the waveguide adjacent to the ring depends among others on the losses in the ring cavity. Therefore, fitting the measured resonance spectrum to the theoretical transfer function allows the determination of the propagation loss of the waveguide forming the ring.

Ref.[25] gives a good description of the derivation of the transfer function of a ring resonator such as the one pictured in Fig.3.3. Let ξ_a and ξ_b be the coupling coefficients between the ring resonator (r) and the adjacent waveguides (a, b), $t_{a,b} = \sqrt{1 - \xi_{a,b}^2}$ the transmission coefficients, and $\phi = \frac{2\pi}{\lambda} n_{\text{eff}} L$ and $\tau = \sqrt{\exp(-\alpha L)}$ (with $L = 2\pi r + 2L_s$) respectively the phase difference and the amplitude attenuation induced by one round-trip in the ring. Considering the π phase-shift occurring when light couples between the ring and the adjacent waveguides, the different field amplitudes in the resonator (see Fig.3.3 for the definition of the various fields) can be

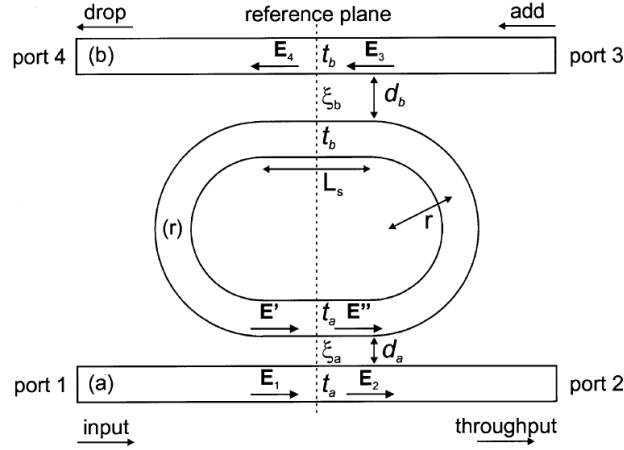


Figure 3.3: Sketch of a ring resonator, describing the notations used for deriving the general transfer function of ring resonators [25].

related as follows:

$$\begin{cases} E_2 = t_a E_1 + i \xi_a E' \\ E'' = t_a E' + i \xi_a E_1 \\ E' = t_b E'' \tau e^{i\phi} \\ E_4 = i \xi_b E'' \sqrt{\tau} e^{i\phi/2} \\ E_3 = 0 \end{cases} \quad (3.5)$$

After a few manipulations, the transmission from port 1 to port 2 of the ring (which is the easiest quantity to measure in practice) is shown to be:

$$|S_{21}|^2 = \left| \frac{E_2}{E_1} \right|^2 = \frac{t_a^2 - 2t_a t_b \tau \cos \phi + t_b^2 \tau^2}{1 - 2t_a t_b \tau \cos \phi + t_a^2 t_b^2 \tau^2} \quad (3.6)$$

This formula is used in the next section to derive the propagation loss in IMOS waveguides.

Measurements

In Fig.3.4, we show the SEM picture of a 10 μm radius ring resonator fabricated in IMOS. According to ref.[10], the bending loss for such a radius is negligible. Therefore, the measured value of the propagation loss in the ring can be considered identical to the propagation loss of straight waveguides. The transmission of this device from Port 1 to Port 2 was recorded using the standard IMOS characterization setup, and Fig.3.5 shows a resonance in the measured transmission spectrum. The squares represent the measured data, and the continuous line a fit of this data using the $|S_{21}|^2$ transfer function of equation (3.6). Since this ring only has one adjacent waveguide, we have $t_b = 1$, and the transfer function can be rewritten as:

$$|S_{21}|^2 = \frac{t^2 - 2t \tau \cos \phi + \tau^2}{1 - 2t \tau \cos \phi + t^2 \tau^2}, \quad (3.7)$$

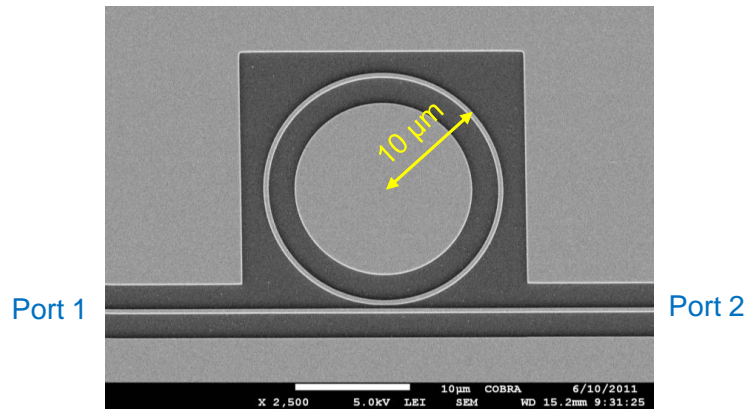


Figure 3.4: SEM picture of a 10 μm radius IMOS ring resonator.

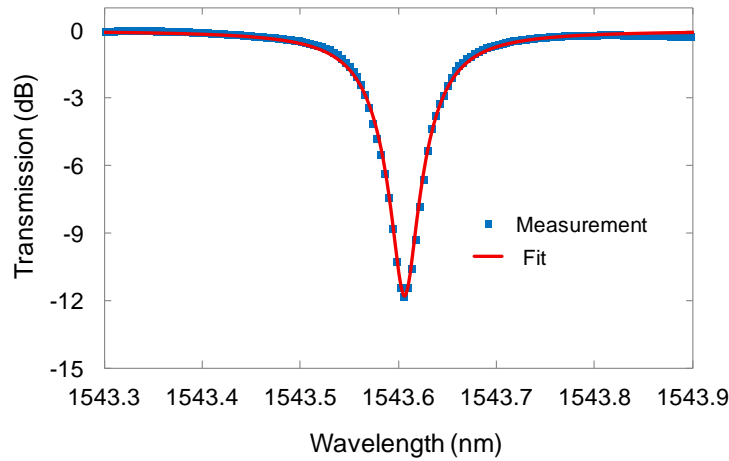


Figure 3.5: Measured transmission of the IMOS ring resonator shown in Fig.3.4.

where t is the amplitude transmission coefficient in the ring's single coupling region. The transfer function is now symmetric in t and τ , therefore we cannot distinguish between the two. Using an effective index value of $n_{\text{eff}} = 2.26$ (calculated using FIMMWAVE) and a ring length of $L = 2\pi \times 10\mu\text{m} = 63\mu\text{m}$, the fit yields (t, τ) or $(\tau, t) = (0.995, 0.991)$. The propagation loss coefficient α (in cm^{-1}) is linked to the round-trip amplitude attenuation in the ring τ and the ring cavity length L by:

$$\alpha = \frac{2\ln(\tau)}{L}. \quad (3.8)$$

Therefore, for this IMOS ring resonator, the propagation loss is $\alpha = 1.7$ or $2.9 \pm 0.2\text{ cm}^{-1}$ (7 or $12 \pm 1\text{ dB}\cdot\text{cm}^{-1}$). Using additional information (e.g. from the transmission of other devices on the same chip), it is usually possible to determine which of these two values is correct.

3.2.3 Mach-Zehnder interferometers (MZIs)

Another way to measure the propagation losses in waveguides using only one measurement is to analyze the transmission of an on-chip Mach-Zehnder interferometer (MZI), such as the one pictured in Fig. 3.6.

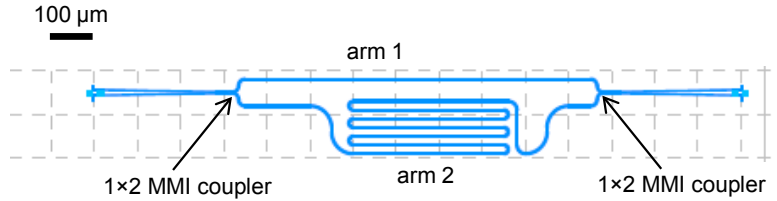


Figure 3.6: Layout of an MZI used to measure the propagation loss of IMOS waveguides.

Principle

The light coming from an input waveguide is split using a 1×2 MMI coupler into two waveguides (arms) of different lengths, and recombined into an output waveguide using a second 1×2 MMI coupler. Due to the length difference between the arms, the light contributions coming from each arm have a different phase and power, leading to interference which appears as sinusoidal oscillations in the transmitted spectrum. As shown below[†], the period and amplitude of these oscillations can then be used to determine respectively the group index N_{group} and the propagation loss coefficient α of the waveguides.

For the sake of simplicity we take the input power to be 1. The amplitude associated with a certain power P is given as $A = \sqrt{P}$ (and $P = AA^*$). This neglects certain constants, but that does not influence the final results, since in the end everything will be calculated back to power. The power launched from the input MMI into each of the two arms:

$$P_{1,2}(0) = 0.5\varepsilon \quad (3.9)$$

where ε is a factor describing the loss due to the input grating-coupler, taper and waveguide and the input MMI. The indices 1,2 refer to the two arms. The coordinate z along the waveguide is taken as 0 at the beginning of the branches. After propagation through the branches the power levels are reduced by the propagation loss:

$$\begin{cases} P_1(L_1) = 0.5\varepsilon e^{\alpha L_1} \\ P_2(L_2) = 0.5\varepsilon e^{\alpha L_2} \end{cases} \quad (3.10)$$

with L_1 and L_2 , the lengths of arm 1 and arm 2.

However, to determine the interferometric behavior of the device we have to include the phase differences obtained in the arms as well. The complex amplitudes

[†]Original idea of the MZI technique and its mathematical description by dr. J.J.G.M. van der Tol

of the signals at the end of the arms is:

$$\begin{cases} A_1(L_1) = \sqrt{0.5\varepsilon} e^{0.5\alpha L_1} e^{i\beta L_1} \\ A_2(L_2) = \sqrt{0.5\varepsilon} e^{0.5\alpha L_2} e^{i\beta L_2} \end{cases} \quad (3.11)$$

with β the propagation constant of the guided modes. In the output MMI-coupler, half of the power from each arm is coupled to the output port, and the resulting interference signal is detected at the output waveguide. We introduce another factor η which describes the loss of the output MMI and the output waveguide. The total complex amplitude arriving at the output is thus:

$$A_{\text{tot}} = \sqrt{0.5\eta} [A_1(L_1) + A_2(L_2)] = 0.5\sqrt{\eta\varepsilon} \left[e^{0.5\alpha L_1} e^{i\beta L_1} + e^{0.5\alpha L_2} e^{i\beta L_2} \right] \quad (3.12)$$

which can be used to calculate the output power:

$$P_{\text{out}} = A_{\text{tot}} A_{\text{tot}}^* = 0.25\eta\varepsilon e^{\alpha L_1} \left[1 + e^{\alpha\Delta L} + 2e^{0.5\alpha\Delta L} \cos(\beta\Delta L) \right] \quad (3.13)$$

with $\Delta L = L_2 - L_1$. Since $\beta = 2\pi/\lambda$, measuring the output power as a function of wavelength will result in constructive ($\cos(\beta\Delta L) = 1$) and destructive ($\cos(\beta\Delta L) = -1$) interference, so a series of peaks and valleys will be found. The propagation loss α can be obtained from the ratio of the maximum and the minimum of the measured spectrum:

$$C = \frac{P_{\text{max}}}{P_{\text{min}}} = \frac{1 + e^{\alpha\Delta L} + 2e^{0.5\alpha\Delta L}}{1 + e^{\alpha\Delta L} - 2e^{0.5\alpha\Delta L}} \quad (3.14)$$

which conveniently removes the loss factors up front in equation (3.13). With some manipulation equation (3.14) can be rewritten as:

$$\frac{C+1}{C-1} = 0.5 \left(e^{-0.5\alpha\Delta L} + e^{0.5\alpha\Delta L} \right) = \cosh(0.5\alpha\Delta L) \quad (3.15)$$

The group index The group index is another important parameter of optical waveguides which take into accounts their dispersion. From the wavelength distance between subsequent peaks, this parameter can be derived. Two subsequent maxima of equation (3.13) are obtained for values of $\beta\Delta L = M2\pi$ and $\beta\Delta L = (M-1)2\pi$, with M a large integer (since ΔL will be much larger than λ). The propagation constant β depends on the wavelength as:

$$\beta = \frac{2\pi n(\lambda)}{\lambda} \quad (3.16)$$

with $n(\lambda)$ the wavelength dependent effective index of the waveguide mode. If two subsequent peaks are at λ and $\lambda + \Delta\lambda$, then:

$$1 = \Delta L \left[\frac{n(\lambda)}{\lambda} - \frac{n(\lambda + \Delta\lambda)}{\lambda + \Delta\lambda} \right] \approx \Delta L \left[\frac{n(\lambda)}{\lambda} - \frac{n(\lambda) + \frac{\delta n}{\delta \lambda} \Delta\lambda}{\lambda + \Delta\lambda} \right] \quad (3.17)$$

Chapter 3. Waveguide loss properties

Using the approximation $\lambda (\lambda + \Delta\lambda) \approx \lambda^2$ (which is quite accurate, if $\Delta L \gg \lambda$), it follows:

$$\Delta\lambda = \frac{\lambda^2}{\Delta L N_{\text{group}}} \quad (3.18)$$

with

$$N_{\text{group}} = n(\lambda) + \frac{\delta n}{\delta \lambda} \Delta\lambda \quad (3.19)$$

Measurements

To demonstrate the validity of this method in measuring waveguide propagation losses, three MZIs such as the one pictured in Fig.3.6 (with $\Delta L = 910 \mu\text{m}$, $1710 \mu\text{m}$, and $2510 \mu\text{m}$, respectively) are fabricated on an IMOS chip. The light of an EDFA is then fed in each of the three devices and their transmission is recorded using an OSA. Fig.3.7 shows the obtained transmission spectra.

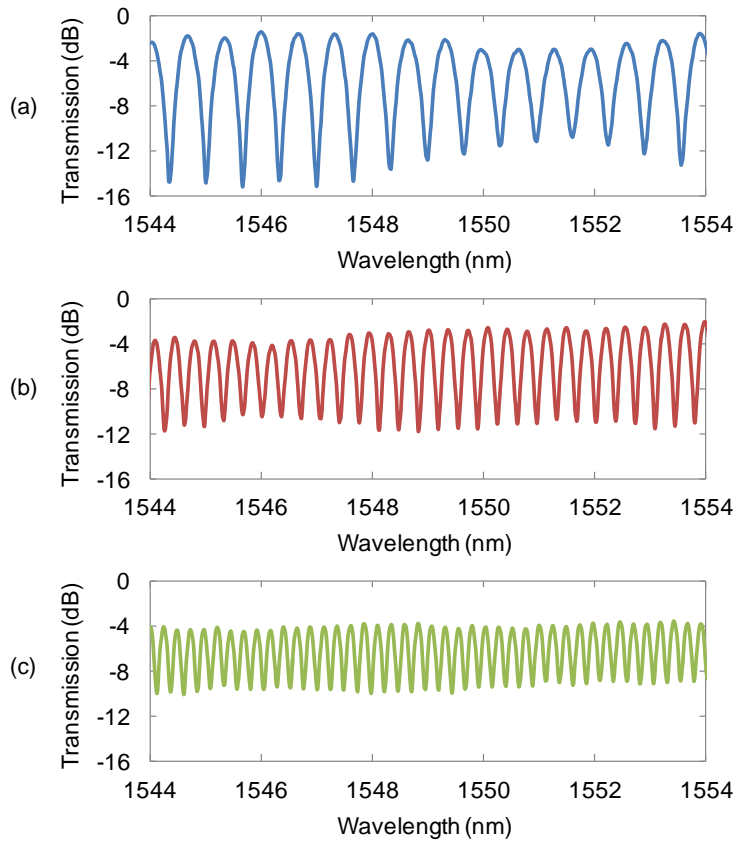


Figure 3.7: Measured transmission spectra of three MZIs fabricated in IMOS. (a) $\Delta L = 910 \mu\text{m}$, (b) $\Delta L = 1710 \mu\text{m}$, and (c) $\Delta L = 2510 \mu\text{m}$.

As expected from equation (3.13), each spectrum shows a cosine dependence with the wavelength. Knowing the length difference ΔL between the two arms of each MZI, the period $\Delta\lambda$ of this cosine dependence can be used to calculate the group index N_{group} , with equation (3.18). As shown in table 3.1, the spectra of all three

MZIs yield a group index of $N_{\text{group}} = 4.0$, comparable to the group index calculated from the FSR of IMOS ring resonators.

	MZI-55	MZI-57	MZI-59
ΔL [μm]	910	1710	2510
$\Delta\lambda$ [nm]	0.657	0.351	0.242
N_{group}	4.02	4.00	3.95
T_{max} [dB]	-1.0	-2.7	-3.9
T_{min} [dB]	-15.2	-11.7	-10.0
$\frac{C+1}{C-1}$	1.08	1.29	1.65
α [dB.cm ⁻¹]	37.7	37.6	37.5

Table 3.1: Results obtained from the analysis of the MZI transmission spectra shown in Fig.3.7.

Next, we use the ratio of the maximum and minimum transmission $T_{\text{max}}/T_{\text{min}} = P_{\text{max}}/P_{\text{min}} = C$ of each spectrum to calculate the quantity $\frac{C+1}{C-1}$, from which the propagation loss coefficient α can be determined using equation (3.15). The only problem here is that the spectra are modulated by parasitic components, which make T_{max} and T_{min} vary slowly over the whole spectrum. This unwanted modulation is most probably caused by parasitic reflections in the MMIs (see Section 6.1.3 for more details). The parasitic modulation function is a cosine function with a maximum value of 1. Therefore, the meaningful values of T_{max} and T_{min} can still be extracted from the graph, where the amplitude of the MZI oscillations is maximum (i.e. where the parasitic modulation function is equal to 1). The spectra of all three MZIs give almost identical results for the propagation loss coefficient ($\alpha = 37.7, 37.6, 37.5 \pm 1$ dB.cm⁻¹, respectively). These values are close to the one obtained with waveguides of different lengths fabricated on the same chip.

The fact that three different MZIs give almost identical results for N_{group} and α shows that this technique is robust and reproducible. Besides, it doesn't depend on the coupling efficiency through the input and output grating couplers, and is therefore not dependent on the operator. But spurious reflections can degrade the transmission spectrum and should be avoided.

3.3 Loss reduction strategies

In the previous section on loss measuring structures, we reported waveguide propagation losses between 10 and 40 dB.cm⁻¹, obtained on different IMOS chips processed separately. Since IMOS circuits envisaged in the future will have lengths of at least several mm or cm, these losses have to be reduced down to just a few dB.cm⁻¹, like on SOI [5, 6]. In IMOS passive waveguides, the main source of propagation loss is scattering loss due to roughness (cf. Fig.3.1). In order to reduce this scattering loss, the first strategy is of course to reduce the roughness (e.g. by partial reflow of the EBL resist pattern after development). Another option is to mitigate the effect of the

roughness by covering it with a material whose refractive index lies between those of the core and of the usual cladding, air. Finally, it has been shown that incorporating C_{60} molecules in ZEP can make it more resistant to dry-etching [26], therefore reducing the thickness needed for pattern definition, and limiting the accumulation of roughness from mask erosion during etching. These strategies are described in more detail in the next three sections.

3.3.1 Thermal reflow of the ZEP pattern

In the IMOS fabrication process, patterns are defined in an electron-sensitive resist, and transferred into the semiconductor material using a hard mask made of SiN (cf. Section 2.3). Due to its relatively low etch-rate in the SiN etching RIE process, we use ZEP as the electron-sensitive resist. However, the polymerization of ZEP during exposure to electrons forms clusters which cause roughness in the ZEP pattern after development. In the subsequent transfer of the pattern from the ZEP to the SiN layer and from the SiN layer to the InP membrane using RIE dry etching, the ZEP roughness creates vertical lines on the sidewalls of the waveguides (cf. Fig. 3.1). These vertical lines are very difficult to remove once they have been created. Therefore, the only way to reduce the roughness in the waveguides sidewalls is to reduce the original roughness in the ZEP pattern.

Luckily, ZEP possesses a phase transition temperature (around 145 °C), above which it starts to reflow [27], losing part of its roughness. Therefore, introducing a reflow bake after development can greatly help reduce the sidewall roughness in IMOS waveguides. Fig. 3.8(a) shows a pattern created by EBL just after ZEP development, with the roughness clearly visible. Fig. 3.8(b) shows the same pattern after a 2'00" ZEP reflow bake at 154 °C[‡]. The roughness on the ZEP surface is considerably reduced. Fig. 3.8(c) and (d) show two IMOS gratings printed respectively without and with ZEP reflow bake. The vertical lines present on the grating sidewalls in Fig. 3.8(c) are completely absent in Fig. 3.8(d). The second grating will have a lower scattering loss and an increased coupling efficiency.

However, the duration and temperature of the reflow bake have to be carefully controlled. If the reflow bake is too long or the temperature too high, the resolution of the exposed pattern can be lost. Fig. 3.9 shows the rounding in the corners of an MMI printed with a ZEP reflow bake (b), compared to an MMI printed without ZEP reflow bake (a). After repeated testing, it was found that a 2'00" reflow bake at 154 °C gives the best results for IMOS samples pre-bonded on silicon.

Finally, reproducibility is critical for this step. The shape of the ZEP pattern can change a lot following a variation of just a few °C around its phase transition temperature. In practice, it is important to make sure that the hotplate is clean when performing the ZEP reflow bake. It is also preferable to use a clean silicon carrier wafer on the hotplate, in order to achieve a good and reproducible contact between the hotplate, the silicon carrier wafer and the IMOS sample.

[‡]154 °C is the temperature setting of the hotplate, assuming that the sample is a III-V membrane bonded on silicon, positioned on a clean silicon carrier wafer lying on the hotplate. This value will be different if the reflow bake is realized under different conditions (e.g. in a vacuum oven), or the sample bonded on a different substrate (e.g. glass).

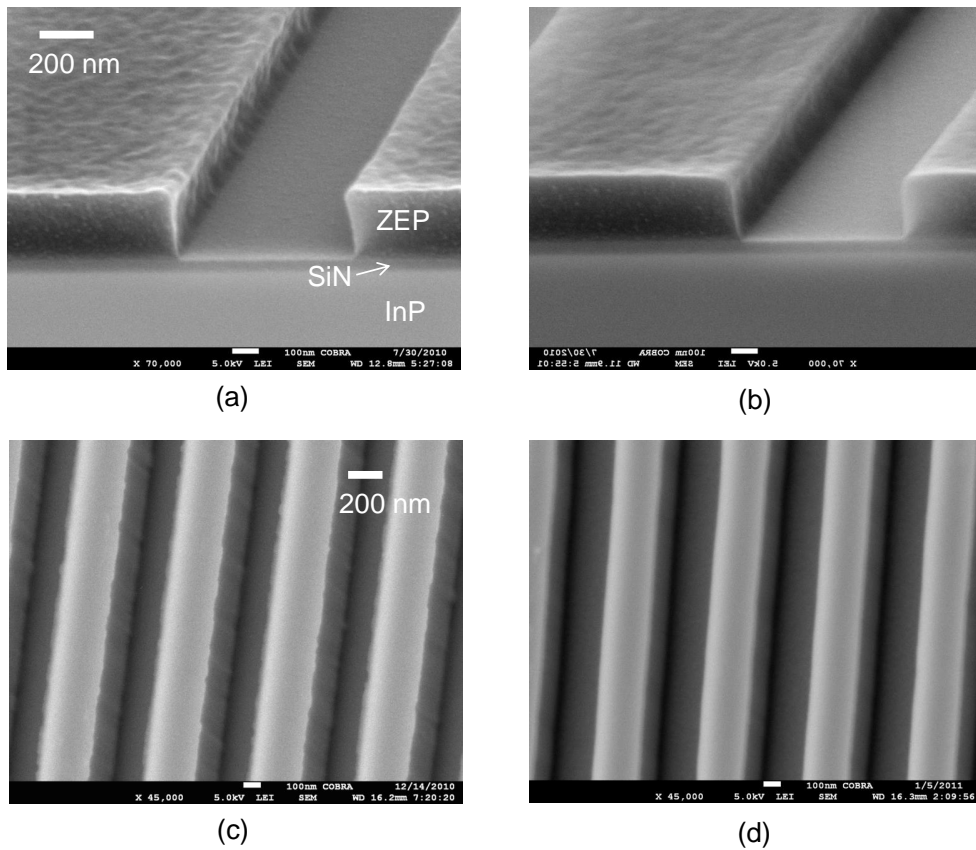


Figure 3.8: (a-b) ZEP pattern on a 50 nm SiN layer on top of InP (a) just after development, and (b) after a 2'00'' ZEP reflow bake at 154 °C. (c-d) Grating etched in InP (c) without ZEP reflow, and (d) with a 2'00'' ZEP reflow bake at 154 °C.

3.3.2 Dielectric overcladding

Another strategy to reduce the propagation loss of IMOS waveguides is to use a dielectric overcladding to reduce the effect of existing roughness [9]. A preliminary experiment is carried out to investigate this technique. Waveguides of different lengths are fabricated on a pre-bonded IMOS sample. The propagation loss is measured to be around $\alpha = 23 \pm 1 \text{ dB.cm}^{-1}$ for wide waveguides ($w = 10 \mu\text{m}$), and $\alpha = 25 \pm 1 \text{ dB.cm}^{-1}$ for narrow ones ($w = 0.45 \mu\text{m}$). The influence of the waveguide width is rather small. This suggests that the loss is not caused only by sidewall scattering, but also by other effects such as top surface roughness, or defects in the bonding layer.

Next, a 400 nm thick overcladding of SiN is deposited on the chip by PECVD. The propagation loss is measured again and found to have decreased to $18 \pm 2 \text{ dB.cm}^{-1}$ and $22 \pm 2 \text{ dB.cm}^{-1}$, for the wide and the narrow waveguides respectively (cf. table 3.2). This indicates that placing a higher index material on the core surface decreases the effect of roughness on the losses. In order to further investigate this method, more experiments are needed, for example using different dielectric overcladdings (SiN, SiO₂, AlO_x, etc.). Recently, IMOS waveguides fabricated with an SiO₂ overcladding have shown a propagation loss of $\alpha = 6.3 \pm 1 \text{ dB.cm}^{-1}$.

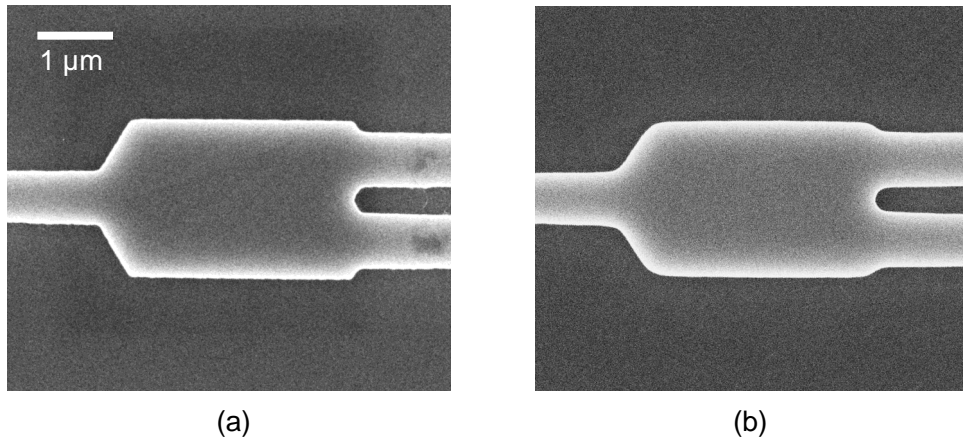


Figure 3.9: Rounding due to the ZEP reflow bake. MMI splitters printed (a) without reflow bake, and (b) with a 2'00'' ZEP reflow bake at 154 °C.

	Air	SiN	
Wide waveguides ($w = 10 \mu\text{m}$)	23 ± 1	18 ± 1	dB.cm^{-1}
Narrow waveguides ($w = 0.45 \mu\text{m}$)	25 ± 1	22 ± 1	dB.cm^{-1}

Table 3.2: Waveguide propagation losses for different overcladdings (Air and SiN).

Finally, when designing the circuit layout, one has to keep in mind that covering waveguides with a dielectric overcladding will reduce the confinement of the modes in the photonic waveguides. Therefore, the smallest bend radius useable will be larger than with an air overcladding.

3.3.3 ZEP/C₆₀ composite resist

The last loss-reducing strategy currently being investigated in our group[§] relies on the introduction of C₆₀ fullerene molecules (also known as “buckyballs”) in the ZEP resist used during waveguide definition by EBL. These molecules can make the ZEP layer much more resistant to dry etching [26]. This brings the double advantage of reducing damage to the pattern during transfer to the SiN layer, and decreasing the resist thickness required for correct pattern definition. As a consequence, the sidewall roughness and waveguide propagation losses can be decreased [28]. Preliminary testing using this method has shown that the waveguide propagation loss in IMOS can be decreased to $3.0 \pm 1 \text{ dB.cm}^{-1}$.

Furthermore, the rounding of the resist pattern caused by the reflow bake (cf. Fig. 3.9) seems to be much reduced when mixing the ZEP with C₆₀ molecules. Therefore, the ZEP/C₆₀ composite resist is very promising both for the definition of low-loss IMOS waveguides and for the fabrication of ultra-small IMOS devices.

[§]Research carried out by dr. Y. Jiao.

3.4 Conclusion

In this chapter, the loss mechanisms relevant in IMOS have been described, together with the structures allowing to measure them, and the strategies used to reduce them. Waveguides fabricated using standard ZEP with a reflow bake and covered with an SiO₂ overcladding have shown propagation losses of $\alpha = 6.3 \text{ dB.cm}^{-1}$, while similar experiments using ZEP/C₆₀ composite resist have shown losses as low as $3.0 \pm 1 \text{ dB.cm}^{-1}$.

Chapter 4

A ring-based memory element

4

As mentioned in Chapter 2, the ability to write, store and read data is a very desirable feature for a photonic platform like IMOS. As shown in everyday life with the CD-ROM or the DVD, optical memories based on phase-change materials (PCMs) can store large quantities of data very inexpensively because the information stored is stable for years without requiring any power supply. Some PCMs can even be switched reversibly millions of times, making them excellent candidates for use as optical memories or in reconfigurable PICs.

Another very interesting application of PCMs in PICs could be the trimming of newly fabricated circuits. Due to unavoidable fabrication errors, the performance of fabricated photonic components often deviates slightly from the design. This deviation is generally corrected using active heaters to exploit the thermo-optic effect in the waveguide material [24]. However, this technique is very power-consuming. Using PCMs, it is possible to correct the design deviations due to fabrication errors once and for all (set-and-forget), reducing the consumption of PICs by up to one order of magnitude [29].

In this chapter, we describe the first PCM optical memory element integrated on a photonic platform. Shown in Fig.4.1, the device is based on a microring resonator combined with a PCM. It was first designed for IMOS but ultimately fabricated on SOI samples due to the availability of inexpensive chips already containing fabricated ring resonators*, allowing to shorten the fabrication time and offering more room for testing. Nevertheless, since IMOS and SOI's main passive properties are virtually identical, the results presented here can be considered fully applicable

*The device was designed by R. Simpson, V. Pruneri, J. Van der Tol and J. Pello. The PCM deposition and device characterization were carried out by J. Pello, R. Simpson and M. Rudé on SOI microring samples provided by Ghent University - IMEC.

to IMOS as well.

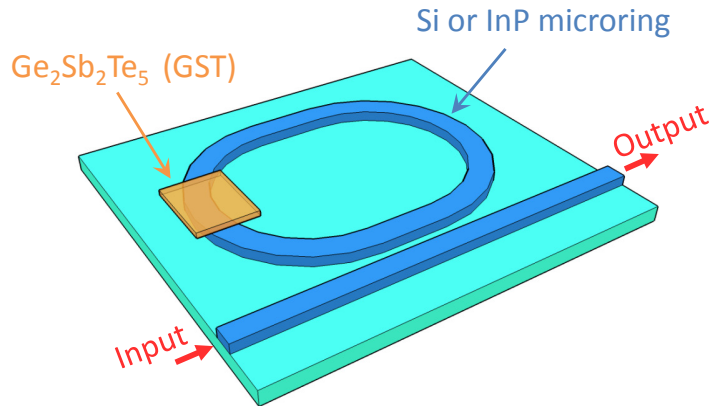


Figure 4.1: Schematic view of the ring-based memory element. The evanescent tail of the optical mode propagating in the ring overlaps with the $\text{Ge}_2\text{Sb}_2\text{Te}_5$ (GST) film. Therefore a change in the optical properties of the GST film induces a change in the ring's transmission.

In the next three sections, we will successively describe how the device was designed, fabricated and characterized.

4.1 Phase-change materials (PCMs)

PCMs exhibit a large change in refractive index and optical absorption when switched between two solid states. Traditionally, these materials have been primarily used in data storage (e.g. rewritable DVDs [30], and electrical phase-change RAM [31]). However, several groups are now looking into the use of PCMs for the active control of photonic circuits.

Fig.4.2 shows a diagram representing the amorphous and crystalline phases of a typical PCM used in data storage. In the crystalline phase, atoms are periodically organized following a lattice structure, whereas in the amorphous phase, they are randomly distributed. Due to these different atomic distributions, the two phases of a PCM have different electrical and optical properties (e.g. resistance, reflectivity, refractive index, optical absorption, etc.).

In addition to having different electrical and optical properties, the two phases of certain PCMs are stable around room temperature for several years [30], and can be switched in a few tens of nanoseconds, and reversibly for up to 1×10^7 cycles [31]. This makes such materials perfectly suitable for non-volatile, low-power memory applications in PICs.

Switching

Switching a PCM between its two phases is achieved by controlled heating (generally using optical or electrical pulses). When a PCM is heated above its melting temperature T_m (typically somewhere between 250 and 550 °C), it changes into a liquid-like state and its atoms can move freely. A subsequent rapid cooling of the PCM (at rates higher than 10^9 K.s^{-1}), forces the atoms to solidify in a disorganized amorphous phase

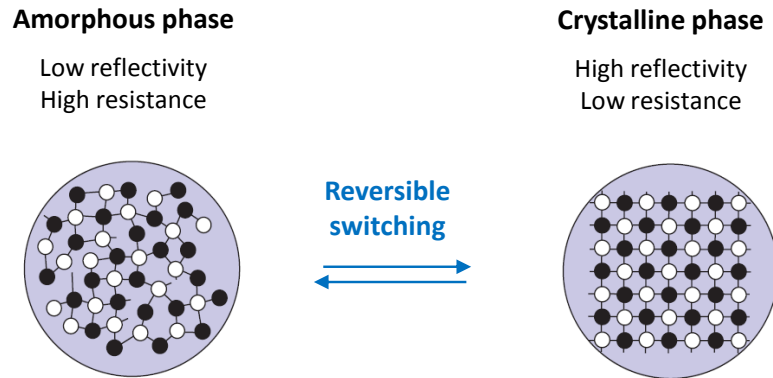


Figure 4.2: Diagram representing the amorphous and crystalline phases of a typical phase change material (PCM) used in data storage. Both phases are stable at room temperature for several years. Switching between both phases is reversible and can take place at sub-nanosecond timescales.

(cf. red path in Fig.4.3). To switch the PCM back to its crystalline phase, it needs to be heated above its glass transition temperature T_g . Atoms then once again become mobile and can rearrange themselves in the more energy-favorable crystalline phase (cf. green path in Fig.4.3). Subsequent cooling solidifies the PCM in its crystalline phase.

In practice, crystallization is achieved by using relatively long pulses of moderate power (enough to make the PCM reach its glass transition temperature), whereas reamorphization is achieved by using shorter high-power pulses (allowing the PCM to reach its melting temperature and then solidify rapidly).

Ge₂Sb₂Te₅ (GST)

In this work, we focus on a PCM named GST for its chalcogenide composition (Ge₂Sb₂Te₅). This is one of the most well-known PCMs, and as shown in Fig.4.4, its complex refractive index $n + ik$ exhibits a large change in the infrared, upon switching between the amorphous and crystalline phases. At $\lambda = 1550$ nm, the relative change in the real part of the refractive index is:

$$\frac{n_{\text{cryst}} - n_{\text{amorph}}}{n_{\text{amorph}}} = \frac{6.5 - 4.0}{4.0} = 0.63,$$

while the relative change in the imaginary part (i.e. the optical absorption) is:

$$\frac{k_{\text{cryst}} - k_{\text{amorph}}}{k_{\text{amorph}}} = \frac{1.4 - 0.1}{0.1} = 13.$$

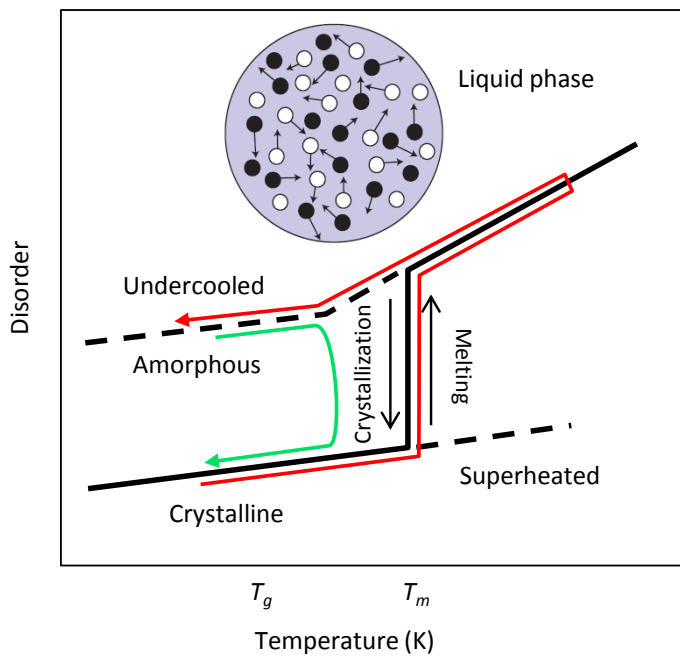


Figure 4.3: Typical phase diagram of a PCM used for data storage (at atmospheric pressure). Switching the phase from crystalline to amorphous occurs along the red path, whereas switching from amorphous to crystalline occurs along the green path. (Adapted from [30])

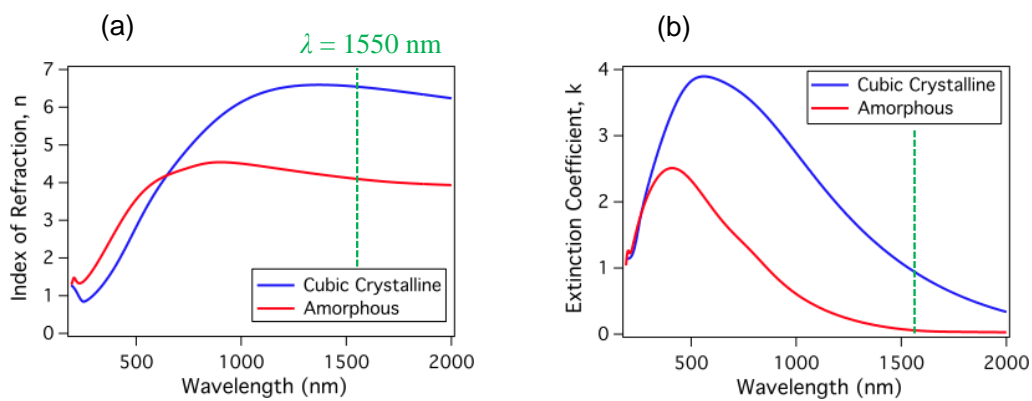


Figure 4.4: Wavelength dependence of the real part (a) and imaginary part (b) of the complex refractive index $n + ik$ of $\text{Ge}_2\text{Sb}_2\text{Te}_5$ (GST), in its crystalline and amorphous phases (reproduced from [32]). The dashed line indicates the center of the C-band ($\lambda = 1550$ nm).

4.2 Design

In order to create a photonic memory element based on GST, we need a device sensitive to the refractive index and optical absorption changes of this material. An obvious candidate is the ring resonator. Indeed, due to their resonating nature, microrings are very sensitive to small changes in their environment, and have already been applied in a wide variety of sensing applications [24], ranging from temperature and pressure sensing to biomolecular detection. Since thin films of GST can be deposited by sputtering and patterned by conventional lithography, we consider the structure depicted in Fig.4.1, where a ring resonator has been locally covered with a rectangle of GST. The ring resonator model described in Section 3.2.2 and a mode solver (FIMMWAVE) are used to optimize the dimensions of the device for memory applications.

In the previous chapter, we saw that the transmission through a ring resonator with a single coupling section (as in Fig.4.1) can be expressed as:

$$|S_{21}|^2 = \frac{t^2 - 2t\tau \cos \phi + \tau^2}{1 - 2t\tau \cos \phi + t^2\tau^2} \quad (4.1)$$

where t is the amplitude transmission coefficient in the ring's coupling region, and ϕ and τ are respectively the phase difference and the amplitude attenuation induced by one round-trip in the ring. Considering a ring of total length L , of which a section of length x has been covered with PCM, ϕ and τ can be expressed as follows:

$$\phi = k_0 n_{\text{eff}}(L - x) + k_0 n_{\text{eff}_{\text{PCM}}}x \quad (4.2)$$

$$\tau = e^{-[\alpha(L-x) + \alpha_{\text{PCM}}x]/2} \quad (4.3)$$

where $k_0 = 2\pi/\lambda$ is the propagation constant of the field in vacuum, and α and n_{eff} (α_{PCM} and $n_{\text{eff}_{\text{PCM}}}$) are the absorption coefficient and the effective index of the mode propagating in the ring section without PCM (with PCM).

For a typical SOI ring resonator, $n_{\text{eff}} = 2.21$, $t = 0.986$ and $\alpha = 4 \text{ cm}^{-1}$. In order to determine $n_{\text{eff}_{\text{PCM}}}$ and α_{PCM} , the waveguide structure shown in Fig.4.5(a) is simulated in FIMMWAVE. An SiO_2 layer of thickness t_{SiO_2} is introduced between the GST and the SOI waveguide, to control the overlap of the propagating mode with the GST film.

The material parameters used in these simulations are shown in table 4.1. Although, the GST covered section of the ring can in the general case be a bent waveguide, we only simulate straight waveguides in FIMMWAVE (for a ring resonator with a bending radius $> 5 \mu\text{m}$, this is assumed to be accurate enough).

In table 4.2, the output of our FIMMWAVE simulations when varying t_{SiO_2} from 20 to 400 nm is presented. We also display this data graphically in Fig.4.6 and Fig.4.7.

As expected from the very high contrast in the imaginary part k of GST's refractive index at $\lambda = 1550 \text{ nm}$ upon phase switching ($\times 13$, cf. Fig.4.4), the absorption coefficient α_{PCM} of the mode propagating in the GST covered waveguide is dramatically modified (up to $\times 57$) when changing the phase of the GST. The fact

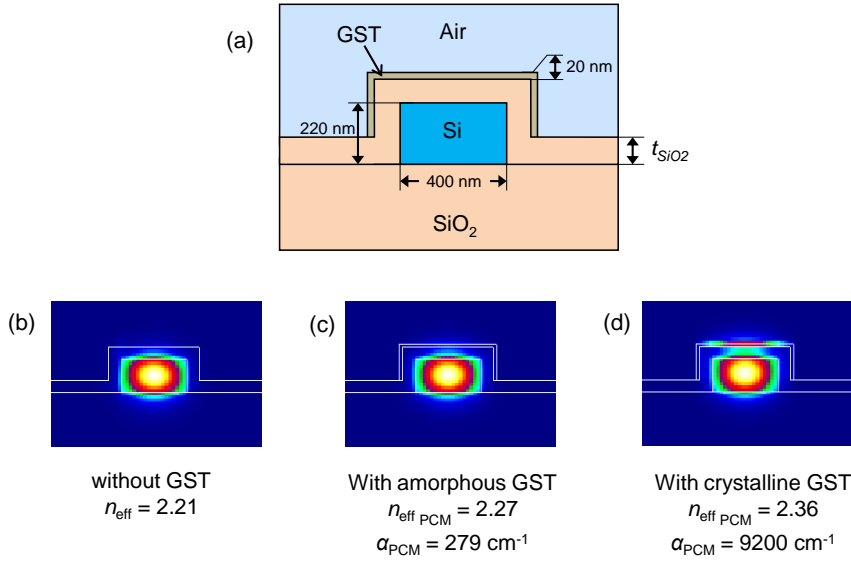


Figure 4.5: (a) Cross-section of the waveguide structure simulated in FIMMWAVE to calculate $n_{\text{eff PCM}}$ and α_{PCM} . (b-d) Intensity profiles of the fundamental TE mode in SOI waveguides, respectively without GST (b), with amorphous GST (c), and with crystalline GST (d), for $t_{\text{SiO}_2} = 80$ nm and $\lambda = 1550$ nm.

	Air	SiO ₂	Si	amorph. GST	cryst. GST
Refractive index	1.00	1.45	3.48	4.0	6.5
Absorption [cm ⁻¹]	0	0	0	8100	113000

Table 4.1: Material parameters used in the simulation of the structure shown in Fig.4.5. The absorption of bulk GST is obtained from the imaginary part k of its refractive index (cf. Fig.4.4), using the relation $\text{Absorption} = \frac{4\pi k}{\lambda}$.

that the relative change in α_{PCM} upon crystallization is even higher than the relative change in k results from the simultaneous increase in n (the real part of the refractive index), which increases the overlap of the mode with the GST. This appears clearly in the calculated intensity profiles shown in Fig.4.5, where the intensity of the light in the GST film is much more important when the GST is crystalline (d) than when it is amorphous (c). Thanks to this effect, the sensitivity of our device to GST switching is increased.

The effective index $n_{\text{eff PCM}}$ of the mode is also affected upon GST switching but to a lesser extent (less than 10 %). This suggests that the change in the resonance wavelength λ_{res} of the final device will be less pronounced than the change in its extinction ratio. When $t_{\text{SiO}_2} > 400$ nm, the mode propagating in the SOI waveguide doesn't feel the GST film, therefore $n_{\text{eff PCM}} \simeq n_{\text{eff}}$, and $\alpha_{\text{PCM}} \simeq \alpha$.

t_{SiO_2} (nm)	amorphous GST		crystalline GST		relative change	
	n_{effPCM}	$\alpha_{\text{PCM}}(\text{cm}^{-1})$	n_{effPCM}	$\alpha_{\text{PCM}}(\text{cm}^{-1})$	n_{effPCM}	α_{PCM}
20	2.340	677	2.598	15960	0.11	22.6
40	2.307	518	2.494	13850	0.08	25.7
60	2.285	400	2.419	11760	0.06	28.5
80	2.269	280	2.362	9230	0.04	32.1
120	2.249	143	2.290	5970	0.02	40.8
180	2.236	56	2.245	2890	0.004	50.5
240	2.231	23	2.232	1330	0.001	56.7
320	2.228	6.6	2.228	342	0	50.8
400	2.228	2.1	2.228	98	0	45.7

Table 4.2: Simulated absolute and relative change in n_{effPCM} and α_{PCM} upon crystallization of the GST film in the structure of Fig.4.5, as a function of the thickness t_{SiO_2} of the SiO₂ layer. This data is represented graphically in Fig.4.6 and Fig.4.7.

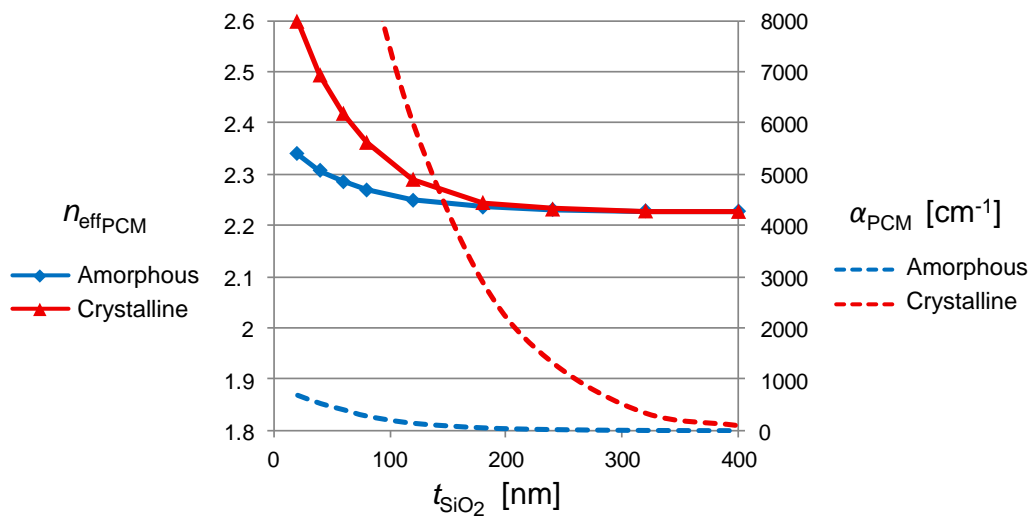


Figure 4.6: Calculated values of n_{effPCM} and α_{PCM} before and after crystallization of the GST film in the structure of Fig.4.5, as a function of the thickness t_{SiO_2} of the SiO₂ layer.

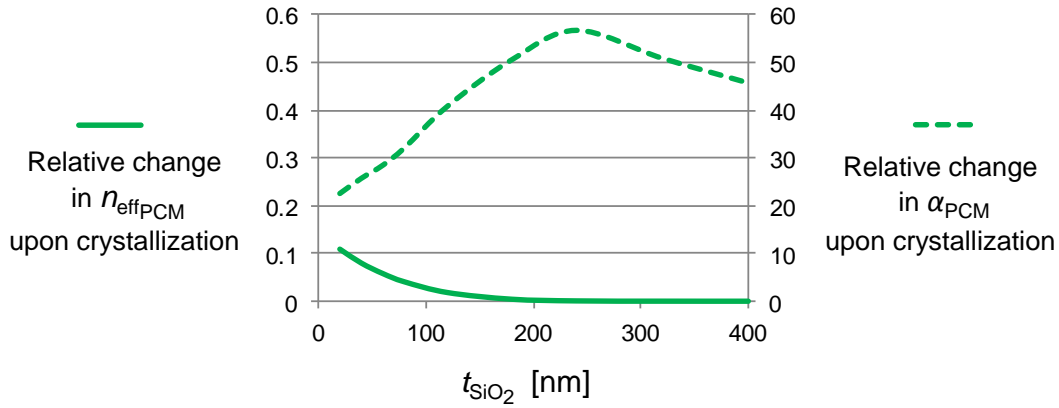


Figure 4.7: Simulated relative change in n_{effPCM} and α_{PCM} upon crystallization of the GST film in the structure of Fig.4.5, as a function of the thickness t_{SiO_2} of the SiO_2 layer.

Using the simulation results of table 4.2 and equations (4.1)-(4.3), we can plot the expected transmission spectrum of the memory element before and after switching. Fig.4.8 shows the transmission of a typical SOI ring resonator (dashed curve), together with the simulated transmission of the memory element created by covering a section of length $x = 0.5 \mu\text{m}$ of this ring with 20 nm of GST, and switching the GST between its amorphous and crystalline phases (blue and red curves, respectively).

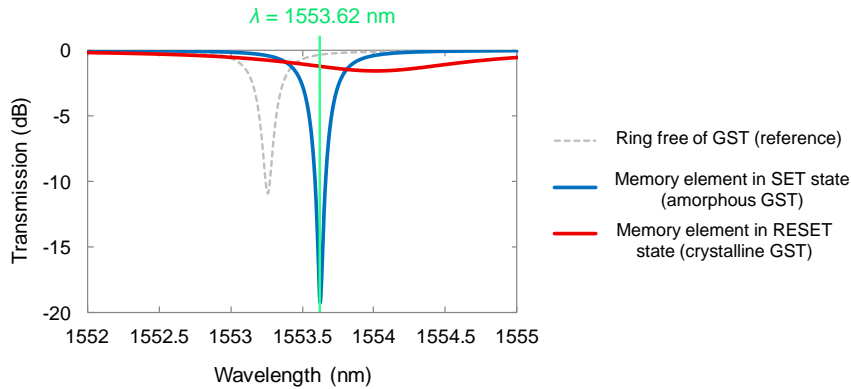


Figure 4.8: Simulated transmission spectrum of the memory element in the SET (amorphous GST) and RESET (crystalline GST) states, showing a modulation of 18 dB at $\lambda = 1553.6 \text{ nm}$. The chosen device parameters are: $L = 37.25 \mu\text{m}$, $x = 0.5 \mu\text{m}$, $t_{\text{SiO}_2} = 120 \text{ nm}$, $t = 0.986$, and $n_{\text{eff}} = 2.21$ in the ring section without GST.

As expected from the relatively small change in the effective index n_{effPCM} upon GST switching reported in table 4.2, the resonance wavelength λ_{res} of the structure with GST in its crystalline phase (red curve) differs by only 0.39 nm from that of the structure with GST in its amorphous phase (blue curve). However, due to the large relative change in the absorption coefficient α_{PCM} , the transmission spectrum exhibits a dramatic change in shape (width and depth of the resonance) when switching the GST from one phase to the other. In this case, the device's Q factor drops from 6600 to 1000, and its extinction ratio from 19.3 dB to 1.6 dB.

Remark: Although the extinction ratio of the ring with amorphous GST (blue curve) is larger than that of the reference ring without GST (dashed curve), the Q factor of the former is lower than that of the latter ($Q = 7700$ and 6600 , respectively). This is because amorphous GST has a non negligible absorption, increasing the round-trip loss of the ring covered with GST.

At a wavelength of $\lambda = 1553.62$ nm, the combination of the wavelength shift with the drop in extinction ratio makes the device function as a reversible and non-volatile memory switch, whose transmission can be modulated by 18 dB. The following sections describe how the device is fabricated and characterized.

4.3 Fabrication

The memory element is fabricated on an SOI chip already containing ring resonators, by depositing GST locally on top of certain rings using the following EBL lift-off process:

1. First, an SiO₂ layer of thickness t_{SiO_2} is deposited on top of the SOI circuit by PECVD.
2. Subsequently, (positive) polymethylmethacrylate resist (950 PMMA A4) is spun on the sample and the area where the GST is to be deposited is exposed and developed using EBL.
3. A 20 nm thick film of amorphous GST is sputtered on the sample from two stoichiometric targets of GeTe and Sb₂Te₃. To avoid oxidation of this GST layer, a 20 nm film of SiN is added on top in the same deposition run.
4. The sample is then put in acetone for 30 minutes to dissolve the PMMA layer and lift-off the excess material.
5. Finally, the device is rinsed with isopropanol and blow-dried.

Fig.4.9 shows both a microscope overview and a SEM close-up of the fabricated memory element. A ring free of GST is placed in series with the memory element, so that the transmission spectra of both rings can be recorded at the same time. This is very useful to ensure that thermal drift, or other environmental parameters affecting the rings, can be decoupled from the transmission changes created when switching the GST.

The SEM picture in Fig. 4.9 shows some remaining “fences” of GST/SiN at the edges of the GST rectangle. This extra material is not totally removed after the lift-off process, because the PMMA e-beam resist doesn’t have a sufficiently negative profile after development. There are ways of avoiding these “fences” by optimizing the EBL process to make the resist edge profile more negative (e.g. using a lower beam energy, or even a double resist scheme [33]). However, due to their small size with respect to the full GST section area, we expect only minimal effect from these “fences” on the operation of the device. Another issue is that there seem to be some sticking problems. The GST pattern on the ring waveguide is not uniform. This

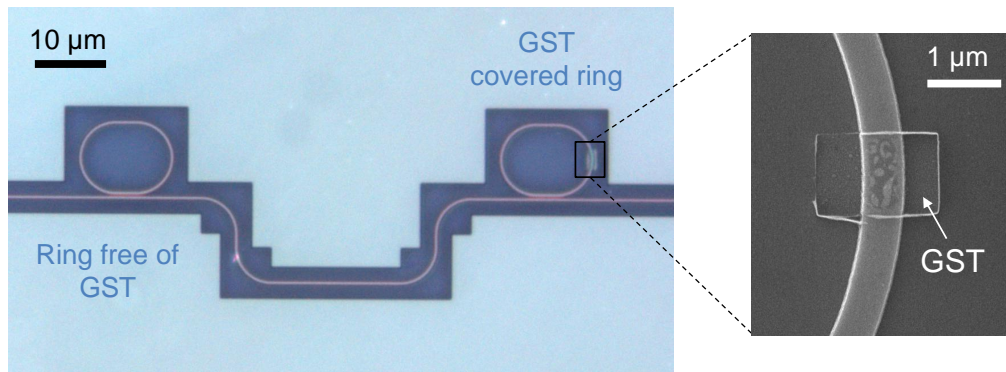


Figure 4.9: (Left) Microscope overview of a ring free of GST (used as a reference during characterization), in series with a ring covered with GST (the memory element). (Right) Close-up SEM picture of the GST rectangle deposited on top of the ring.

may explain why the switching of the fabricated device is less strong than that of the simulated one (cf. Section 4.4.3).

In the following section, we describe the setup used to characterize the fabricated memory element, and report the measured performance.

4.4 Characterization

4.4.1 Optical switching setup

In order to characterize the memory element, we monitor the transmission of the two rings (with and without GST) shown in Fig.4.9, while switching the phase of the GST film using optical pulses. In order to focus and position the switching laser beam, the standard IMOS transmission measurement setup described in Section 2.4 had to be extended and adapted as shown in Fig.4.10.

Switching (pump) laser Phase transitions in the GST layer are triggered by heating a 1 μm spot with focused laser radiation at $\lambda = 975$ nm, where GST is strongly absorbing (cf. Fig.4.4). The electrical current driving the pump laser is maintained at a sub-threshold level during most of the experiments, except when electrical pulses with tunable length and amplitude generated in a function generator (Agilent 33220A, 20 MHz) are sent to the laser through a bias-T circuit. The optical pulses are collimated and focused on the sample surface using a 0.6 NA (50×) long-working distance microscope objective. The working distance of the microscope objective needs to be long enough to allow sufficient space underneath for the two fibers used to record the transmission of the device.

Transmission measurements Fibers are used to couple probe light from an amplified spontaneous emission (ASE) source (1520 to 1580 nm) into the chip, and record the transmitted spectrum with an OSA. Optimal coupling to and from the chip is achieved using two 3-axis micropositioners (cf. Section 2.4).

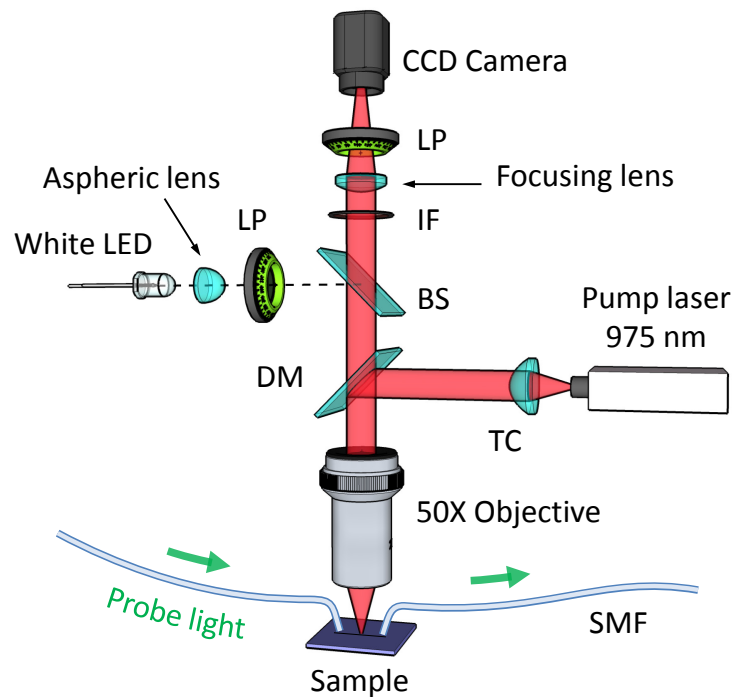


Figure 4.10: Schematic of the experimental setup used to characterize the memory element. (LP: Linear polarizer, IF: Infrared filter, BS: Beam splitter, DM: Dichroic mirror, TC: Triplet collimator, SMF: single-mode fiber.)

A special compact holder, shown in Fig. 4.11, was designed to fit the fibers under the microscope objective, while ensuring 10° incidence with the sample's normal.

Alignment The reflection of the switching laser spot on the sample surface is monitored with a CCD camera, and a 3-axis stepper motorized stage is used to position and focus the 975 nm laser radiation on the GST section. A short-pass infrared filter (cut-off = 950 nm) is added to attenuate the intensity of the switching laser's reflected light and avoid damage to the camera.

Illumination Homogeneous illumination of the sample is achieved using a white LED, an aspheric condenser lens, and cross-polarizers to optimize the contrast of the image.

Temperature Finally, SOI microrings are notoriously sensitive to external variations in temperature. As shown in Section 4.4.3, the typical resonance wavelength shift obtained upon total crystallization of the GST film is equivalent to a 3°C temperature change. Therefore, the temperature of the chip during the experiments is fixed at $22 \pm 0.02^\circ\text{C}$, using a thermoelectric cooler (TEC).

4.4.2 Switching parameters determination

The laser pulse time and power for crystallization and reamorphization of the GST film are strongly dependent on the film composition, thickness and on the thermal

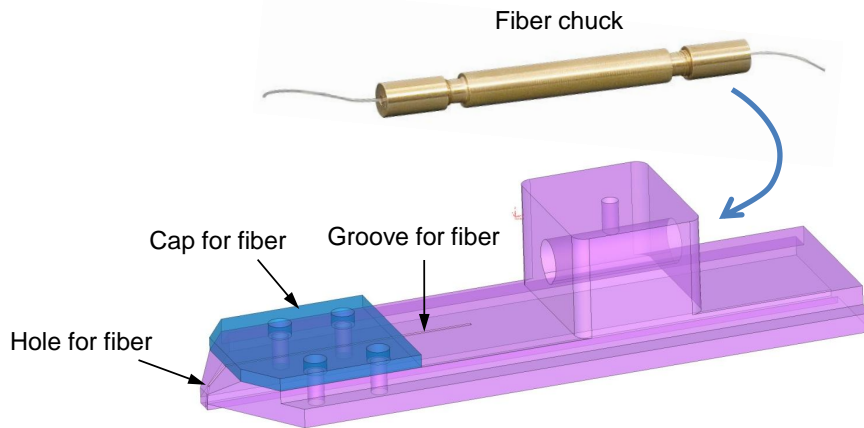


Figure 4.11: Drawing of the compact mechanical holder used to fit the in/out-coupling fibers under the microscope objective.

properties of the surrounding material. In order to determine the optimal switching parameters on our chip, a large area of GST is deposited on an empty part of the SOI chip. The laser pulse duration and power are iteratively increased while scanning the laser position, until a color change can be observed on the sample surface.

In Fig. 4.12(a), the position of the switching laser spot is scanned from bottom to top (along the white arrow) and from right to left. At first, the image is completely blue (amorphous GST's color in these conditions), however for pulses of 300 ns with a power in excess of 12 mW, the sample color is locally changed from amorphous GST's blue to crystalline GST's brighter beige. Therefore, on this chip a pulse of 12 mW and 300 ns can be used to crystallize amorphous GST.

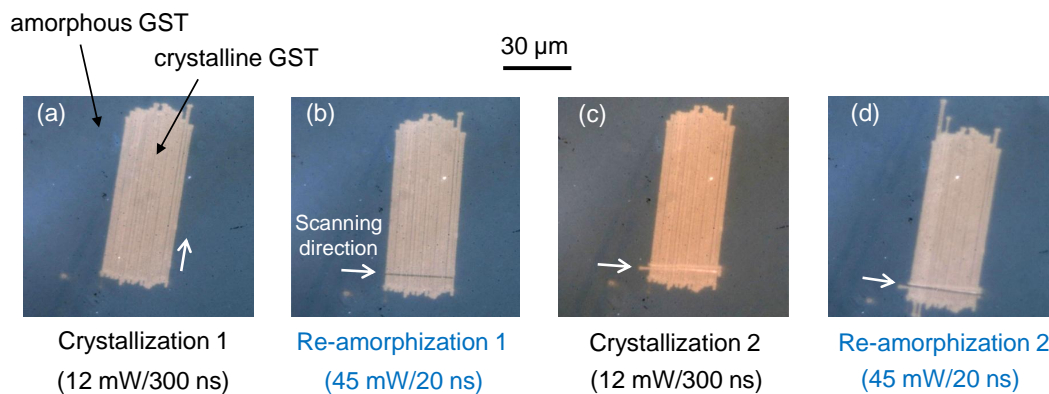


Figure 4.12: Top-view microscope images of the GST area used to determine the optimal optical pulses switching parameters. Crystalline GST appears brighter than amorphous GST. In each picture (a-d), the switching laser had the power and duration given in parentheses, and the position of the switching laser spot was scanned along the direction of the white arrow.

In order to determine the pulse parameters for re-amorphization of crystalline GST, the same procedure is repeated on the previously created crystalline GST area.

This time the position of the switching laser spot is scanned from left to right. For pulses of 20 ns with a power of 45 mW, a blue line is created on the beige crystalline GST area (cf. Fig.4.12(b)). As expected, the amorphization pulse is shorter and more powerful than the crystallization pulse. Since GST can be switched reversibly, it is possible to recrystallize the amorphized line using crystallization pulses (12 mW/300 ns), as shown in Fig.4.12(c), and reamorphize it again using amorphization pulses (45 mW/20 ns), as shown in Fig.4.12(d).

Finally, the diameter of the crystallized/amorphized spots is found to be approximately the same as the focused pump laser waist, i.e. 1 μm .

4.4.3 Results

Two chips are processed, respectively with $t_{\text{SiO}_2} = 120$ nm and 50 nm. The switching behavior for the chip with $t_{\text{SiO}_2} = 120$ nm is weaker than expected from the simulations (cf. Fig.4.8). We attribute this to the fact that the GST deposited in our sputtering machine has a different refractive index than reported in [32], or that the film was not perfectly uniform (cf. Fig.4.9). The results presented in the following paragraphs are all taken from the chip with $t_{\text{SiO}_2} = 50$ nm.

Static measurements

Fig.4.13 shows the full transmission spectrum of the structure pictured in Fig.4.9, with the GST set in its amorphous phase. Since the measured structure contains two resonators in series, the resonances in the graph appear grouped in pairs. The left one in each pair corresponds to the ring with GST and is modified upon phase transitions, while the right one, corresponding to the ring free of GST, is used as a control.

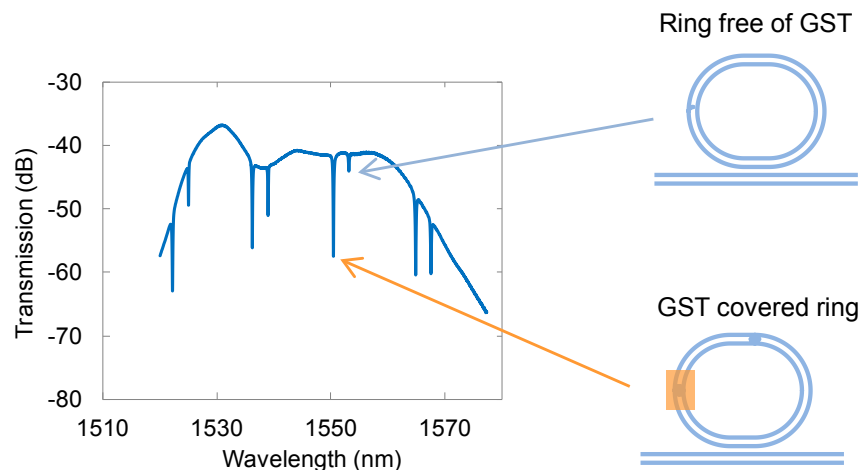


Figure 4.13: Transmission spectrum of the two rings of Fig.4.9 (with and without GST), between 1520 and 1580 nm.

Since the GST area ($1.5 \mu\text{m} \times 3 \mu\text{m}$) is larger than the pump laser spot (1 μm diameter), it is necessary to move (1 μm steps) the laser across the area and repeatedly apply the crystallization pulse until the complete area of GST is crystallized. In practice, this can be achieved in just 3 shots along the waveguide axis.

Chapter 4. A ring-based memory element

Fig.4.14(a) and (b) show the evolution of a resonance of the ring free of GST, and covered with GST respectively, during GST crystallization. The resonance of the ring without GST remains the same throughout the crystallization process. This means that environmental parameters such as temperature didn't vary during the measurements. Therefore, the changes observed in Fig.4.14(b) are purely due to the GST phase transitions.

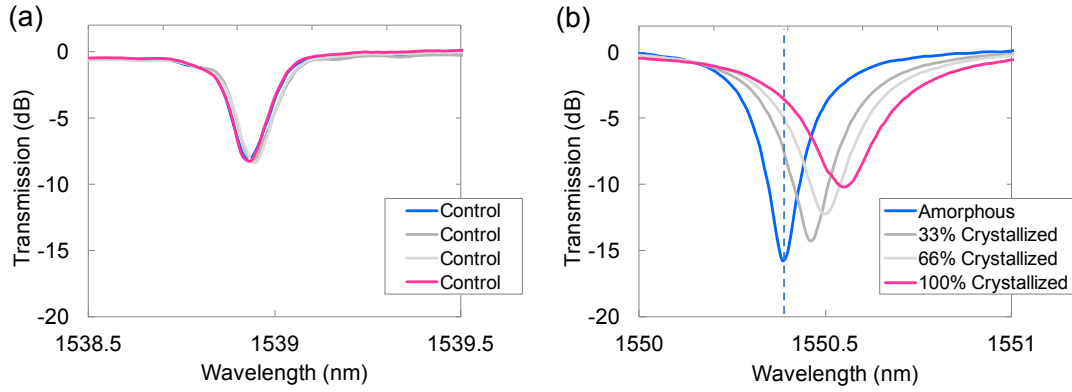


Figure 4.14: Evolution of the resonance of the ring free of GST (a), and the ring covered with GST (b) shown in Fig.4.9, during crystallization of the GST film.

As expected from the simulation results shown in Fig.4.8, crystallization of the GST leads to a red-shift of the memory element resonance, as well as a drop in the Q factor. When the GST is fully crystallized, the resonance wavelength is red-shifted by 0.17 nm, and the Q factor drops from ~ 5500 to ~ 3500 . The combination of these two effects results in a 12.4 dB modulation of the memory device's transmission at $\lambda = 1550.38$ nm.

After crystallizing the GST area, the process was repeated using reamorphization pulses, in order to complete a full SET-RESET cycle (cf. Fig.4.15). Using equation (4.1), the resonator parameters are then extracted from the graphs in Fig.4.14(b) and Fig.4.15(b), and gathered in table 4.3.

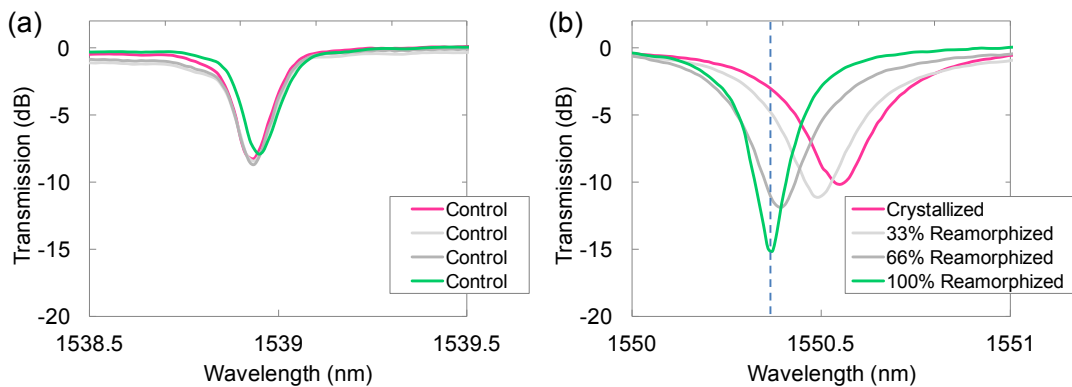


Figure 4.15: Evolution of the resonance of the ring free of GST (a), and the ring covered with GST (b) shown in Fig.4.9, during reamorphization of the GST film.

State	λ_{res} (nm)	n_{eff}	τ	t	Q
Amorphous	1550.384	2.3204	0.986	0.983	5656
33% Crystallized	1550.456	2.3205	0.977	0.983	4433
66% Crystallized	1550.492	2.3206	0.974	0.983	4115
Crystallized	1550.552	2.3207	0.968	0.983	3641
33% Reamorphized	1550.492	2.3206	0.972	0.983	3922
66% Reamorphized	1550.396	2.3205	0.974	0.983	4051
Reamorphized	1550.372	2.3204	0.986	0.983	5411

Table 4.3: Evolution of the resonator parameters during the SET-RESET cycle.

The reamorphized state is nearly, but not fully, identical to the original as-deposited amorphous state (with maximum differences around 5%). This is in accordance with other devices based on GST, which sometimes require more than 100 SET-RESET cycles before exhibiting perfectly reproducible properties [31].

Finally, the intermediary states (33% and 66% crystallized) are also stable at room temperature and could in principle be used to store multiple bits in a single memory element.

High-speed measurements

For any memory element, the switching speed is a key parameter. Therefore, the transient behavior of our memory element is investigated using a tunable laser (HP 8168F) instead of the ASE source, and a fast photodiode (ThorLabs PDA8GS, <1 ns rise time) instead of the OSA. The laser is tuned at the respective λ_{res} of the amorphous/crystalline state and using 0.4 mW of optical power, the response of the device during one crystallization/reamorphization cycle is monitored with an oscilloscope (see Fig. 4.16).

The dynamics of this response result from the light-induced structural phase transition of the GST film as well as thermal effects in the SOI resonator following light absorption in the GST.

When the switching laser pulse reaches and is absorbed by the amorphous GST, it heats it up, thus starting to induce crystallization, and at the same time causing a red-shift of the resonance (observed as an increase in transmission in Fig. 4.16(a)ii). As a consequence of this red-shift, the resonating optical power of the probe in the ring is reduced, as well as the heating due to its absorption in the GST. Therefore, a blue-shift of the resonance follows, causing a drop in transmission (cf. Fig. 4.16(a)iii). This blue-shift once again increases the optical power resonating in the ring and the heat caused by probe absorption in the GST, therefore a new red-shift occurs, until, after approximately 5 μs , all the induced effects have reached a steady-state condition (cf. Fig. 4.16(a)iv).

When the initial phase is crystalline, the dynamics are similar except that they are generated with a shorter pump pulse (20 ns), and that the final resonance wavelength is shorter than the probe wavelength (cf. Fig. 4.16(b)viii).

In conclusion, our memory element can be switched in about 5 μs . The tran-

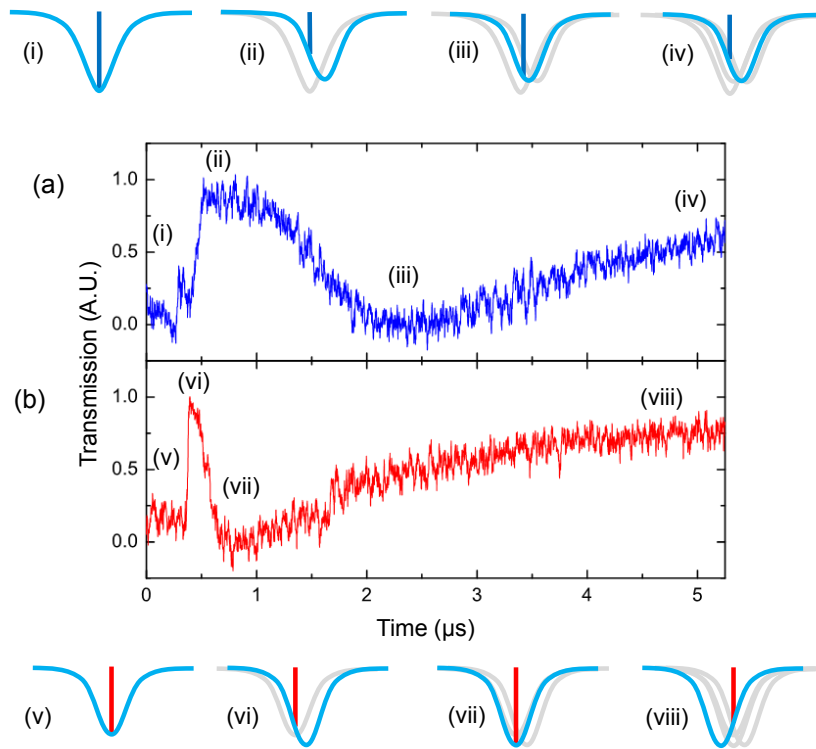


Figure 4.16: Time response of the device during (a) a crystallization pulse ($\lambda_{\text{probe}} = 1550.384 \text{ nm}$) and (b) a reamorphization pulse ($\lambda_{\text{probe}} = 1550.552 \text{ nm}$). Diagrams (i)-(iv) and (v)-(viii) represent the expected change in the device spectrum with respect to λ_{probe} at different moments during the crystallization and reamorphization respectively.

sient behavior is mostly due to thermal effects. Therefore, by placing heat-sinking structures with high-thermal conductivity next to the device, its time response could be enhanced and limited only by the GST phase transition time (a few hundred nanoseconds).

4.5 Conclusion

In this chapter, we have described a memory element based on the combination of a microring resonator with a phase-change material (GST). The measurements performed on a fabricated device show that its transmission at $\lambda = 1550.38 \text{ nm}$ can be reversibly modulated by 12.4 dB, using optical pulses. The switching time was shown to be around $5 \mu\text{s}$, limited by the speed of the heat dissipation from the structure, rather than the switching speed of GST.

This device can be used as an optical memory element on SOI and IMOS, and for the trimming of newly printed ring resonator circuits.

Chapter 5

A Polarization conversion device

5

Polarization handling is a fundamental issue in PICs. Since the propagation properties of the TE and TM polarized modes often differ strongly, most devices only function well for a single polarization. A polarization diversity scheme is then required in order to process the orthogonally polarized light [13]. Furthermore, polarization can be taken advantage of, e.g. for light intensity modulation or polarization bit interleaving [34]. For all these applications, an efficient broadband polarization converter is the key component.

Recently, several polarization rotators with conversion lengths below $< 50 \mu\text{m}$ have been demonstrated, mostly on the silicon-on-insulator (SOI) platform. The shortest ones ($\sim 10 \mu\text{m}$) are based on L-shaped cross-section waveguides [35], or waveguides with two sub-wavelength trenches of different depths [36]. However, these two designs both rely on relatively tight fabrication accuracies (alignment between two etching steps for the former, and nm-resolution lithography for the latter). A more tolerant device based on the cross-polarization coupling effect has shown good performance [37], but at the price of a longer conversion length ($44 \mu\text{m}$). Finally, an ultra-short ($2 \mu\text{m}$ long) polarization converter design based on a triangular waveguide etched at 45° was proposed in [38], showing very good simulated performance, but with a high sensitivity to the etching angle.

In this chapter, we introduce a polarization converter in IMOS similarly based on triangular waveguides for a short device, but optimized for high tolerance to fabrication errors. This polarization converter is the world's smallest InP polarization converter made to date ($0.4 \mu\text{m} \times 0.8 \mu\text{m} \times 7.5 \mu\text{m}$). In the following sections, we describe successively the design, fabrication and characterization of this new device.

5.1 Design

5.1.1 Principle

Fig.5.1 shows the schematic of the IMOS polarization converter design, and the Poincaré sphere diagram of the TE-to-TM polarization conversion. As described in [39], the Poincaré sphere is a graphical tool in real, three-dimensional space that allows a convenient description of polarized signals and of polarization transformations caused by propagation through devices. Linear polarizations are located on the equator. Circular states are located at the poles, with intermediate elliptical states continuously distributed between the equator and the poles. The evolution of polarization for light traveling through a birefringent medium is represented by a circular arc about an axis drawn through the two points representing the eigenmodes of the medium.

The idea behind the use of asymmetrical cross-section waveguides in polarization converters is to create a new set of eigenmodes which are not aligned with the TE and TM polarization of normal rectangular waveguides, and which propagate with different propagation constants β_1 and β_2 . The incoming polarization state, e.g. TE in Fig.5.1, is projected on these two tilted eigenmodes. As the eigenmodes propagate with different speeds, a phase-shift is created between the two that linearly increases with the propagation length L (the same birefringence principle as in bulk half-wave plates). By choosing the length L of the triangular section and coupling light back to a rectangular waveguide, different elliptical and linear polarization states can be obtained.

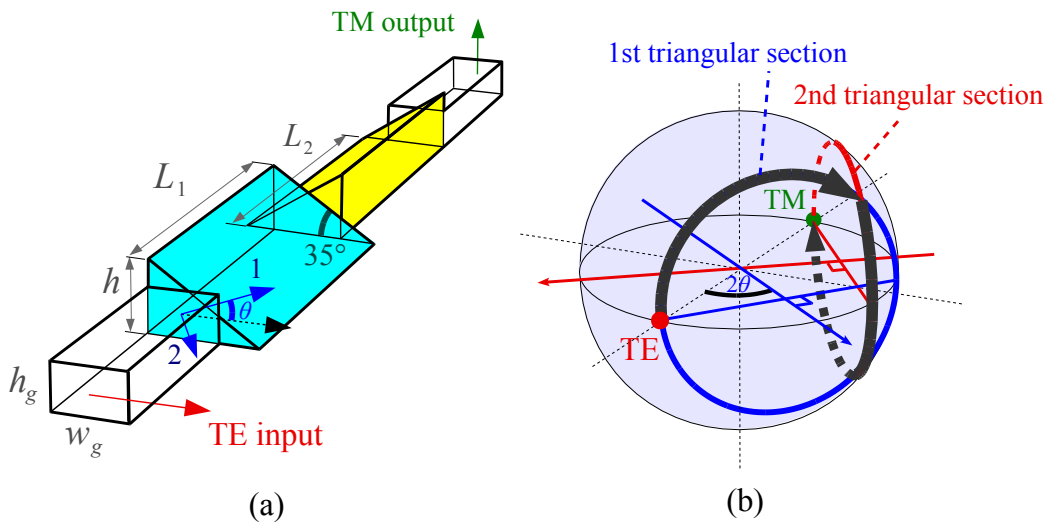


Figure 5.1: (a) Schematic of the IMOS polarization converter design. (b) Poincaré sphere diagram of the TE-to-TM polarization conversion.

In this work, we consider triangular InP waveguides that can be obtained by dry etching of the vertical wall and HCl-based wet etching of the slanted wall at an angle of 35° with respect to the (001) plane [40]. Other chemicals can in principle be used to create sloped sidewalls in InP, such as Br_2 -methanol which creates a slanted

wall at 55° from the substrate plane. However, in order to achieve a good coupling between the triangular waveguides and standard rectangular waveguides, a smaller angle is preferred.

The asymmetry resulting from the triangular waveguide geometry yields a tilt θ of its eigenmodes w.r.t. the standard TE/TM orientation (cf. Fig. 5.1(a)). As a consequence, the polarization states attainable by varying the length of the first triangular waveguide are all the states represented by the blue circle on the Poincaré sphere in Fig. 5.1. We see that in order to achieve full TE to TM conversion, one triangular section is not enough. Therefore, we add another triangular section, mirrored w.r.t. the first one, which enables to reach the TM polarization state by rotating along the red circle on the sphere in Fig. 5.1. The two black arrows in the sphere show how the polarization is gradually converted from TE to TM.

The lengths L_1 and L_2 of the two triangular sections leading to a full TE to TM conversion can be obtained by simple geometric calculations in the Poincaré sphere, and expressed as:

$$L_1 = \frac{L_\pi}{\pi} \times \left[\arcsin \left(\frac{1}{(\tan 2\theta)^2} \right) + \frac{\pi}{2} \right] = 2L_\pi - L_2, \quad (5.1)$$

with θ the tilt angle of the triangular waveguide's two eigenmodes, and L_π their half-beat length, defined as:

$$L_\pi = \frac{\pi}{(\beta_1 - \beta_2)}. \quad (5.2)$$

The device has a total length of $2L_\pi$. Therefore, the stronger the birefringence of the triangular waveguide, the shorter the device.

5.1.2 Design optimization

To design the polarization converter, we first model the triangular waveguide in FIMMWAVE, taking into account the BCB and air claddings of a fabricated device (see Section 5.2). Fig. 5.2 shows the mode profiles of the triangular waveguide's two eigenmodes at $\lambda = 1550$ nm.

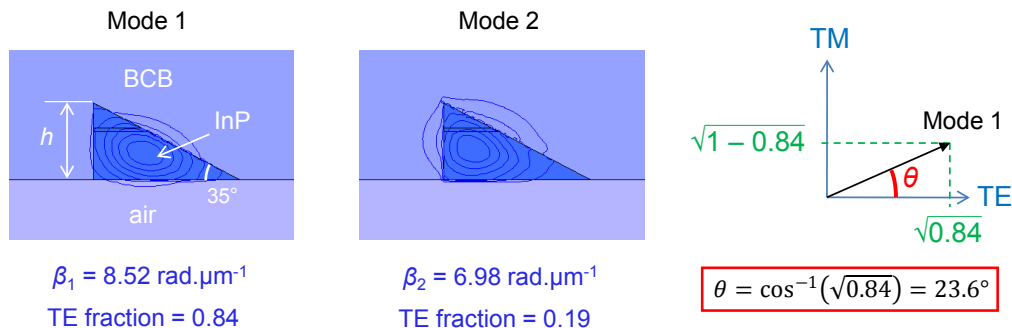


Figure 5.2: Intensity profiles of the triangular waveguide's two eigenmodes, for $h = 400$ nm. The calculated propagation constants β_1 and β_2 , and TE fractions of these modes are indicated. The diagram on the right describes how the TE fraction of the first eigenmode can be used to estimate the tilt angle θ .

The simulation provides the propagation constants β_1 and β_2 of the two eigenmodes, from which the half-beat length L_π can be derived, using equation (5.2). In Fig. 5.3, the calculated half-beat length L_π is represented as a function of the triangular waveguide height h .

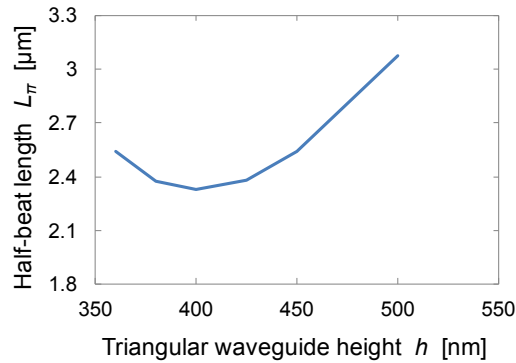


Figure 5.3: Calculated half-beat length L_π of the two eigenmodes in the triangular waveguide, as a function of the triangular waveguide height h .

We observe a local minimum in L_π for $h = 400$ nm. Setting the value of h at this local minimum of L_π brings two advantages. First, according to equation (5.1), this enables to make our device shorter (only $4.7 \mu\text{m}$). As a consequence, the device will be more broadband (since less affected by dispersion), and more suitable for applications where TE and TM absorption are different (such as POLIS [17]). Second, at this local minimum, the first order derivative is 0. Therefore, the effect of small variations in h (and by extension, of other geometrical parameters such as L_1 and L_2) is reduced, making the device more fabrication-tolerant.

The mode solver simulation also provides the approximate TE (power) fractions of both eigenmodes. The first mode is a quasi-TE mode (TE fraction = 0.84), whereas the second is mostly TM (TE fraction = 0.19). The diagram on the right hand side of Fig. 5.2 shows how the TE fraction of the first eigenmode can be used to estimate the tilt angle of the eigenmodes θ . In this case, $\theta \sim 24^\circ$. However, the fact that the sum of the TE fractions of the two eigenmodes is not equal to 1 ($0.84 + 0.19 = 1.03$), as would be expected from orthogonal modes, shows that these values are not accurate enough. In order to determine L_1 and L_2 accurately, the full device is modeled in FIMMPROP, the propagation module of FIMMWAVE.

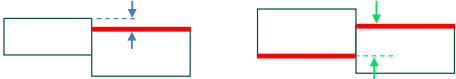
After setting h to 400 nm, the cross-section dimensions h_g and w_g of the input/output rectangular waveguides (see Fig. 5.1), as well as the lateral offsets between the different sections are optimized to maximize the coupling efficiency. For this, each parameter is varied separately and then set to the value that gives the maximum transmission. It is found that the coupling between rectangular and triangular waveguides is optimized for $h_g/h \sim 2/3$. This suggests the use of a very thin etch-stop layer in the membrane to enable a simple and accurate definition of these two heights. A 20 nm-thick InGaAsP etch-stop layer is therefore included in the simulation of the triangular waveguides.

The simulations show that the device works best for $L_1 = L_2 = 2.35 \mu\text{m}$. This suggests that the real value of the tilt angle θ is close to 22.5° , meaning that the

blue and red circles on the Poincaré sphere of Fig.5.1 intersect on the equator of the sphere. After optimization of the different parameters (cf. table 5.1), the device exhibits an insertion loss of -0.54 dB, and a polarization conversion efficiency, defined as

$$\text{PCE} = \frac{P_{\text{TM}}^{\text{out}}}{P_{\text{TE}}^{\text{out}} + P_{\text{TM}}^{\text{out}}} \quad (5.3)$$

for a fully TE polarized input wave, of more than 99.99 %. Fig.5.4 shows how TE light (horizontally polarized) is gradually converted to TM light (vertically polarized) when passing through the two triangular sections of the device.



h	L_1	L_2	w_g	h_g	offset 1	offset 2
[nm]	[μm]	[μm]	[nm]	[nm]	[nm]	[nm]
400	2.35	2.35	400	250	30	340

Table 5.1: Dimensions of the polarization converter design, after optimization in FIMM-PROP. As shown in the top-view diagrams above the table, “offset 1” is the lateral offset between a rectangular waveguide and the vertical sidewall of a triangular waveguide (in red), whereas “offset 2” is the offset between the vertical sidewalls of two triangular waveguides.

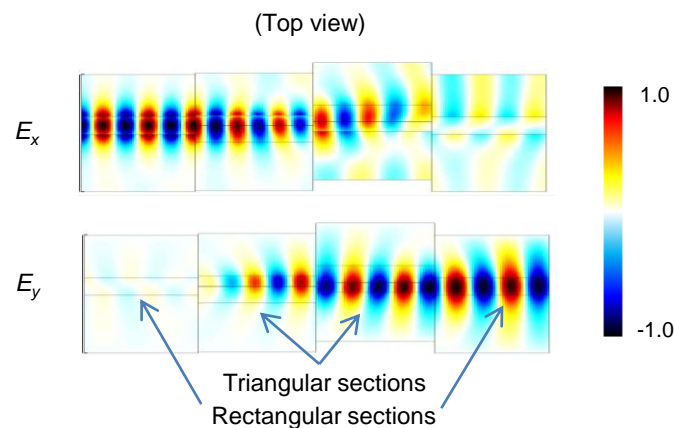


Figure 5.4: Top-view field mapping of the horizontal (E_x) and vertical components (E_y) of the electric field in the device when injecting TE light from the left hand side. ($L_1 = L_2 = 2.35 \mu\text{m}$.)

5.1.3 Wavelength behavior and tolerances

Next, the wavelength behavior of the device is investigated by sweeping the wavelength from 1300 to 1700 nm. As seen on the spectrum graph in Fig.5.5, the short length of this polarization converter makes it very broadband. For the 1400 to

1600 nm wavelength range, the device insertion loss is less than -0.6 dB and the PCE is more than 98 %.

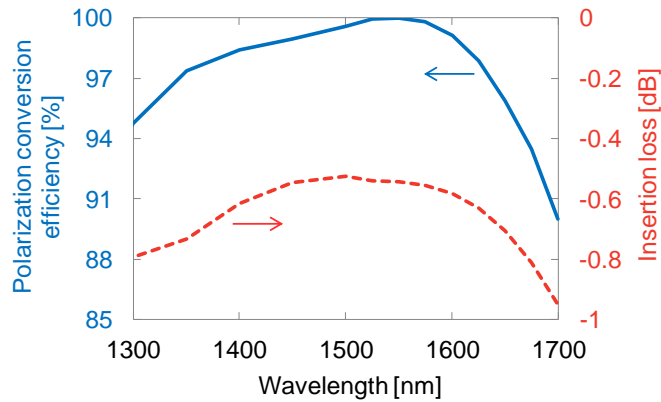


Figure 5.5: Simulated spectral behavior of the IMOS polarization converter. The polarization conversion efficiency is > 98 % and the insertion loss < -0.6 dB in the 1400 to 1600 nm wavelength range.

The use of wet-etching, which enables to set the slope of the slanted wall of the triangular waveguides very accurately to 35° and to define precisely the two heights h and h_g , makes our design intrinsically tolerant. Using a single EBL step to define the rectangular waveguides and triangular waveguides' straight sidewalls also greatly reduces the errors in L_1 , L_2 , offset 1 and offset 2. However, a small overetch of the SiN triangular waveguides sidewall protection can still lead to a reduction in h , while a small mistake in the dose factor used in the EBL can make w_g deviate from the design. Therefore, using our FMM model of the device, we simulate the tolerance of our polarization converter design to variations in the triangular waveguide height h , and the input/output waveguide width w_g . The results are plotted in Fig.5.6 and Fig.5.7, respectively.

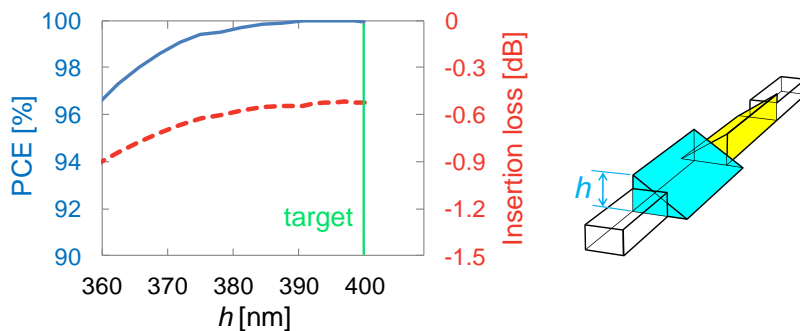


Figure 5.6: Simulated tolerance to variations in the polarization converter's triangular waveguides height h .

As seen on these plots, an error of 20 nm in the definition of the triangular waveguides height h (respectively, an error of 100 nm in the rectangular waveguides width w_g) increases the losses by only 0.1 dB without degrading noticeably the PCE. Such levels of error are relatively easy to control in our fabrication process.

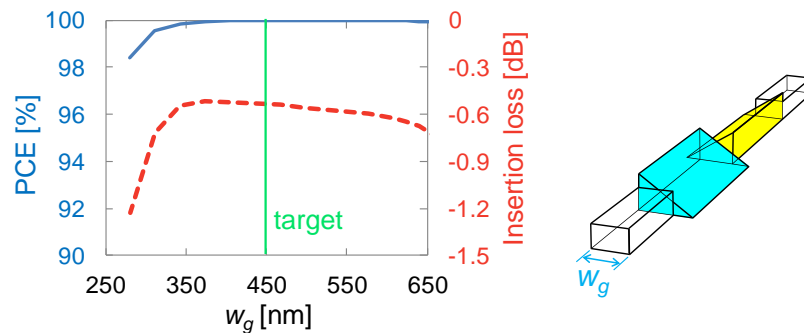


Figure 5.7: Simulated tolerance to variations in the polarization converter's input/output waveguides width w_g .

5.2 Fabrication

5.2.1 Process-flow

The polarization converter is fabricated using the IMOS pre-bonding fabrication scheme [10]. Fig.5.8 describes the main steps of the fabrication.

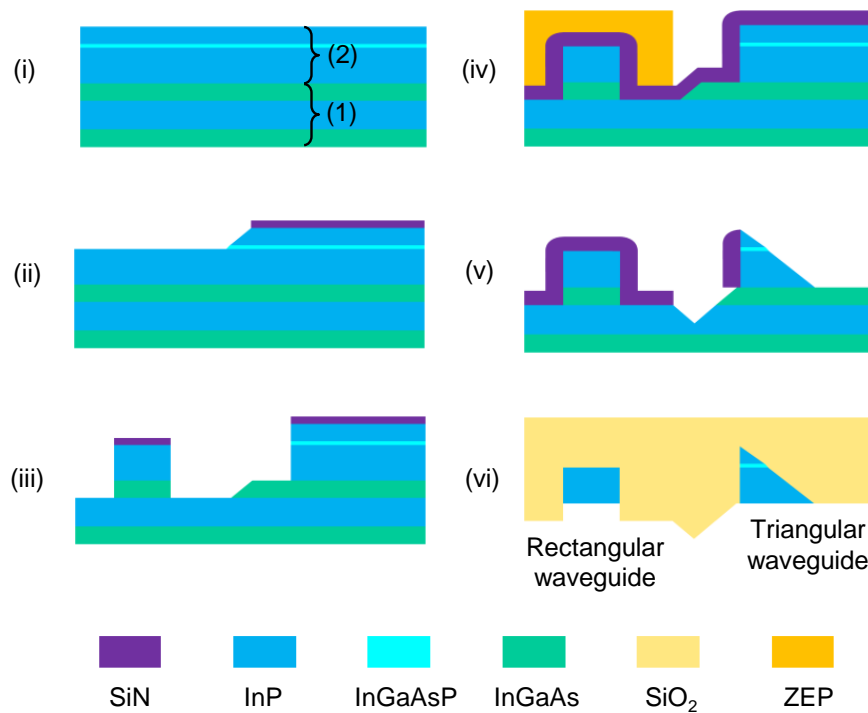


Figure 5.8: (i-vi) Process-flow used to fabricate the polarization converter. (1) (100 nm InGaAs / 200 nm InP / 100 nm InGaAs), (2) (250 nm InP / 20 nm InGaAsP / 130 nm InP)

- (i) First, a layer-stack is grown by MOVPE on an InP substrate. This layer-stack can be separated into stack (1) (100 nm InGaAs / 200 nm InP /



100 nm InGaAs), which is used to protect the membrane during substrate removal, and stack (2) (250 nm InP / 20 nm InGaAsP / 130 nm InP), which forms the membrane and will contain the device. As mentioned in Section 5.1, the 20 nm-thin InGaAsP layer in the membrane is used to define accurately h and h_g , with minimum damage to the material.

- (ii) After depositing a 50 nm thick SiN layer on the sample by PECVD, an EBL step, with ZEP resist, is used to open the SiN in the areas where the membrane thickness should be h_g . The sample is then etched chemically first in solution (A) 1HCl: 4H₃PO₄ and subsequently in solution (B) 1H₂SO₄: 1H₂O₂: 10H₂O, to selectively remove the (130 nm InP / 20 nm InGaAsP) layers from the areas opened in the SiN.
- (iii) In the following step, the rectangular waveguides and the vertical sidewalls of the triangular waveguides of the future polarization converter are defined simultaneously, by EBL on a new SiN layer. The pattern is transferred to the III-V layers using a CH₄-H₂ reactive ion etching (RIE) process.
- (iv) A new 200 nm-thick SiN layer is deposited, and a final EBL is used to open locally the areas of the future triangular waveguides. The SiN layer is then etched in a CHF₃-O₂ RIE process, controlling the etching time in such a way that the SiN is removed from the horizontal areas but not from the vertical sidewalls defined previously. This is rendered possible by the good conformality of the SiN PECVD deposition and the strong verticality of the SiN RIE process used.
- (v) The stack (2) is then etched wet-chemically in the regions opened in the SiN layer, using the solutions (A) and (B) mentioned in step (ii). Since the etching produced by these solutions stops on the (112) plane of InP, a 35° slope running from the top of the SiN covered sidewall to the first InGaAs etch-stop layer below is obtained.
- (vi) After the triangular waveguides have been created, the SiN layer is removed by BHF. The InP chip is then covered with a SiO₂ cladding to reduce the effect of sidewall roughness (cf. Section 3.3.2) and improve adhesion to BCB. The chip is subsequently bonded upside-down to a silicon carrier wafer using a 100-nm thick BCB layer. Finally, the substrate and the stack (1) are removed by wet-etching to create the high-contrast IMOS circuit.

Fig. 5.9 shows the cross-section of an IMOS polarization converter just before bonding (corresponding to step (v) of the fabrication process-flow shown in Fig. 5.8). In this picture, the layer-stack of Fig. 5.8(i) is clearly visible, as well as the two well-defined oppositely-loaded triangular waveguides. As seen on the left of the triangular waveguide in the foreground, the first two etch-stop layers of stack (1) are locally etched during the wet-etching of the triangular waveguides' slopes. However, the

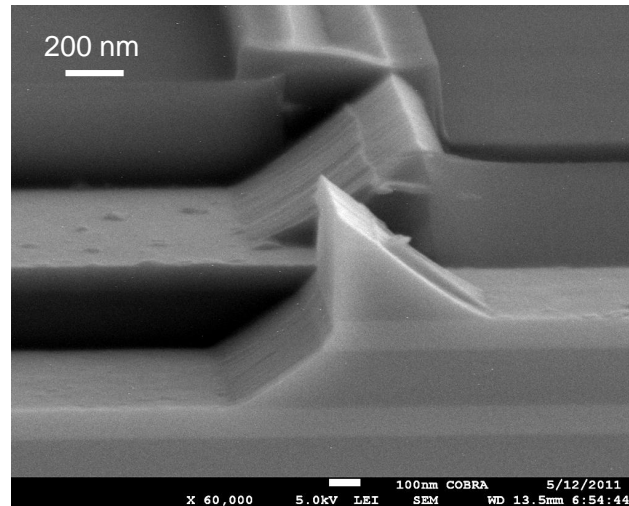


Figure 5.9: Cross-section of a polarization converter just before bonding.

last (InGaAs) etch-stop layer is still present to protect the devices during substrate removal. Incidentally, the SiN vertical sidewall protection is still visible in the background triangular waveguide, but was removed from the triangular waveguide in the foreground during the cleaving process preceding this picture. The only serious problem that occurred during this fabrication run is a damage at the junction between both triangular sections (see also Fig.5.11(a) for a clearer view).

As shown in Fig.5.10, this problem can be solved by keeping a ~ 200 nm wide SiN protection rectangle on top of the junction in step (iv) of the process-flow. Note that in Fig.5.10 since the epitaxial layers of the real device were not present, the step (ii) of the process-flow described above was skipped.

Important issues to consider during fabrication

When fabricating the IMOS polarization converter, the orientation of the printed pattern with respect to the crystal directions of the InP wafer is of paramount importance. For a (100)-oriented InP wafer, the triangular waveguides can only be printed parallel ($\pm 1^\circ$) to the primary flat.

As mentioned earlier, another important point to take into account during fabrication is the junction between the two triangular waveguides. Fig.5.11(a) shows how the junction between two triangular waveguides is damaged during the triangular waveguide slope wet-etching. This problem has been solved by keeping a rectangle of SiN on top of the junction. However, due to the small size of this rectangle, extra care has to be taken in controlling the EBL dose, and the EBL resist reflow bake duration/temperature (cf. Section 3.3.1). The design also has to be slightly adjusted when using this technique.

Finally, the SiN RIE etching time in step (iv) of the fabrication process-flow has to be controlled carefully. If this time is too short, a thin SiN layer will remain on top of the area of the triangular waveguides and prevent the slope wet-etching from taking place. This can be seen in Fig.5.11(b), where a thin layer of SiN has prevented the slope wet-etching, except in the corners of the light gray area and in

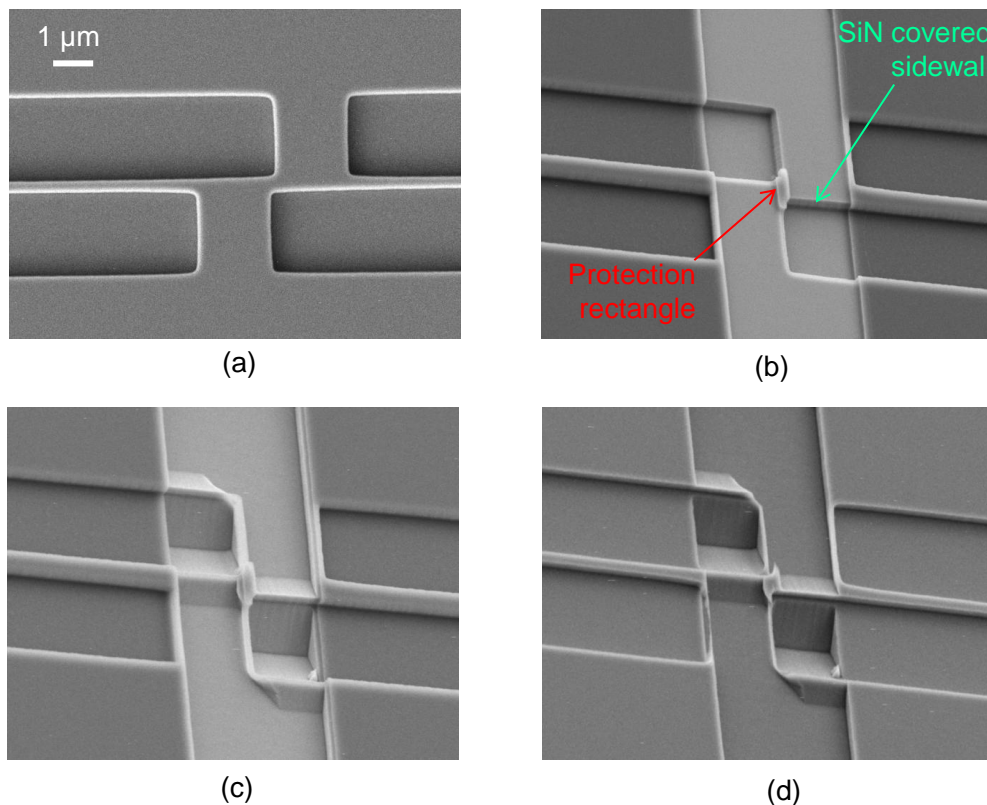


Figure 5.10: SEM pictures taken during a fabrication test of the polarization converter on a dummy InP wafer. (a) Top-view of the device after waveguide etch [step (iii)]. (b) Device after SiN deposition and local dry-etching in order to open the future triangular waveguide sections for wet-etching [step (iv)]. (c) Device after wet-etching of the triangular waveguides. (d) Final device, after SiN removal in BHF, but before bonding [step (v)].

the trenches, where the SiN layer must have been originally thinner. On the other hand, etching the SiN for too long will reduce the height of the sidewall protection. As a consequence, the triangular waveguides height will be less than the designed value h , and the device performance will deviate from the design.

Changes to go to post-bonding processing

In principle, the process-flow described in Fig.5.8 can be used as well for post-bonding processing. However, two points require attention. First, the cleaved edge of a bonded InP membrane is usually partially damaged after bonding. It is important to still be able to determine the direction of the primary flat in order to align the pattern properly. Second, as usual in post-bonding processing, the SiO₂/BCB bonding stack has to be protected from all steps involving HF.

After taking care of the aforementioned issues, the polarization converter is successfully fabricated (with pre-bonding processing). The characterization of the device is described in the next section.

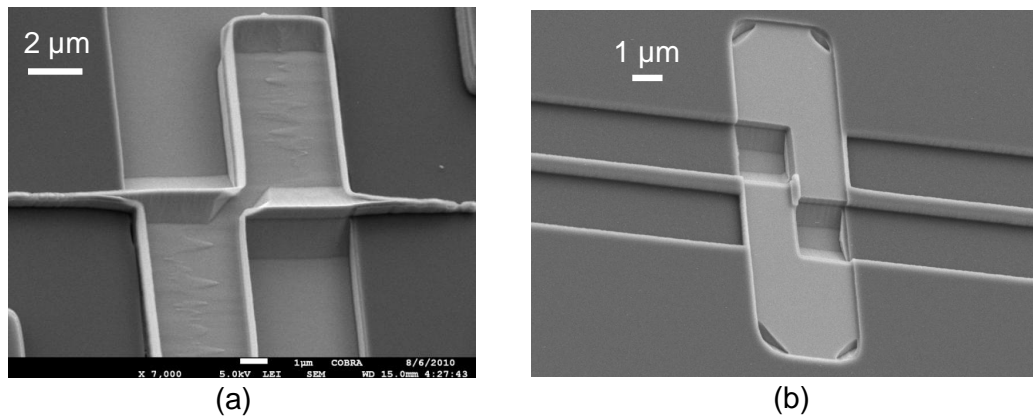


Figure 5.11: (a) Junction between two triangular waveguides damaged during the slope wet-etching. (b) Unsuccessful slope wet-etching due to the remaining of a thin SiN layer on top of the triangular waveguides.

5.3 Characterization

5.3.1 Characterization technique

As explained in Section 2.4, transmission measurements on passive IMOS devices are usually performed using grating-couplers. Due to their diffractive nature, grating-couplers are optimized to couple one polarization into the chip, and suppress the orthogonally polarized light with a 50 dB extinction ratio [35]. As a consequence, when grating-couplers are used, it is not possible to directly measure the polarization state of the output light while rotating the input polarization. In order to measure the device's polarization conversion characteristics, while coupling only TE light in and out of the chip, we used an alternative technique, based on the variation of the length L_{rec} of a rectangular section introduced between the two triangular sections (see Fig. 5.12).

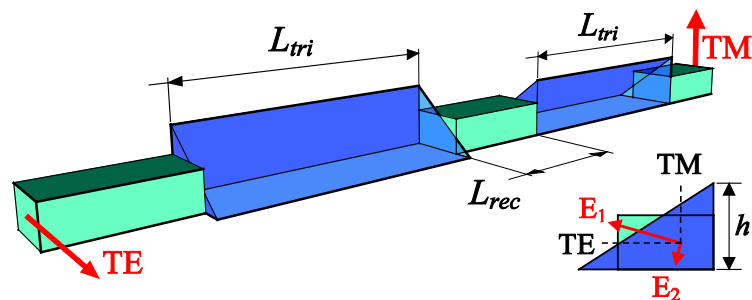


Figure 5.12: Diagram of the structure used to characterize the IMOS polarization converter.

As described in the Poincaré sphere diagram of Section 5.1.1, for a TE-polarized input light, the polarization state after propagating through the first triangular section is a complex superposition of the TE and TM modes. Since the TE and TM modes propagate at different speed in the rectangular waveguide, a phase-shift is created

between them that linearly increases with L_{rec} . This phase-shift will distinctly modify the designed behavior of the polarization converter, and cause the polarization state of the light leaving the device after propagating through the second triangular waveguide to contain a partial TE component, instead of the fully TM polarized state predicted by design. Fig.5.13 shows the simulated transmission of this structure as a function of L_{rec} , for a TE polarized input signal.

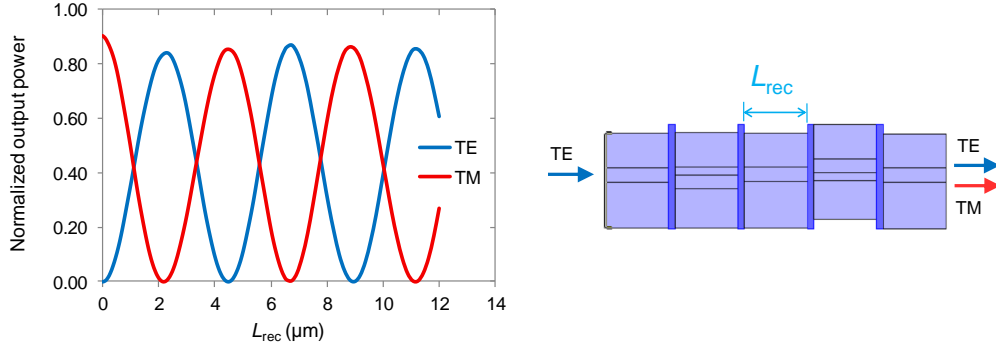


Figure 5.13: Simulated transmission of the structure of Fig.5.12 as a function of L_{rec} , for TE polarized input light.

When L_{rec} is an odd multiple of

$$L_{\pi}^{\text{rec}} = \frac{\pi}{\beta_{\text{TE}} - \beta_{\text{TM}}} \quad (5.4)$$

(where β_{TE} , β_{TM} are the propagation constants of the TE and TM modes in the rectangular waveguide), the conversion in the second triangular section is reversed with respect to the first one, therefore the output polarization state should be fully TE-polarized. Conversely, when L_{rec} is an even multiple of L_{π}^{rec} , the polarization state is the same before and after the rectangular section, and the device again functions as a TE-to-TM polarization converter. As expected from the wave nature of light, the linear relation between the phase-shift created in the rectangular section and its length L_{rec} is translated into a $(\cosine)^2$ variation of the TE-TE transmission versus L_{rec} . Thus, by measuring this transmission T as a function of L_{rec} , and fitting the result to

$$T = T_0 \cos^2(a \cdot L_{\text{rec}} + \varphi), \quad (5.5)$$

the performance parameters of the polarization converter can be obtained.

5.3.2 Results

Three sets of 16 structures each are fabricated. For each set, the length of the triangular waveguides is kept constant ($L_{\text{tri}} = 2.1 \mu\text{m}$, $2.35 \mu\text{m}$ and $2.6 \mu\text{m}$, respectively), while the length L_{rec} of the central rectangular waveguide is varied from 4 to $11.5 \mu\text{m}$ in steps of $0.5 \mu\text{m}$. Fig.5.14 shows the layout of one of these sets of 16 structures. In order to reduce the writing time of the EBL steps, 1×2 MMI power splitters are used to connect a common input waveguide to four structures.

The TE-TE transmission of each structure is measured separately using the

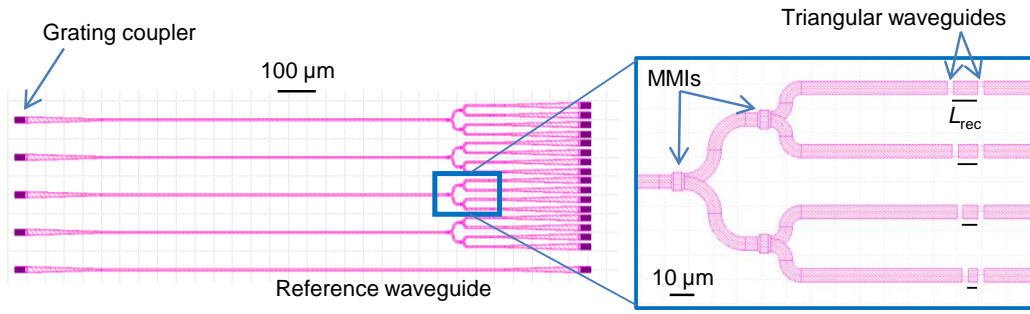


Figure 5.14: Layout of a set of 16 structures used to characterize the polarization converter.

standard IMOS transmission setup (cf. Section 2.4), and normalized to the average transmission through the 4 ports of a reference MMI tree containing only waveguides. The transmission results are plotted as a function of L_{rec} in Fig. 5.15.

Each set of data is fitted with a $10\log_{10}(\cos^2)$ function, in order to give sufficient weight to the low power points which provide the essential information on the polarization conversion. The fitting is then used to determine the PCE and insertion loss of each set at maximum conversion (i.e. with L_{rec} optimized for full TE to TM conversion). The usual definition of the PCE shown in equation (5.3) has to be rewritten here in terms of the extinction ratio ER of the $(\cosine)^2$ function. At a minimum (T_{min}) of the $(\cosine)^2$ function, we measure exactly $P_{\text{TE}}^{\text{out}}$ in equation (5.3). $P_{\text{TM}}^{\text{out}}$ cannot be measured directly, but is by design equal to the maximum (T_{max}) of the $(\cosine)^2$ function (cf. Fig. 5.13). Therefore, the definition of the extinction ratio,

$$\text{ER} = 10\log \frac{T_{\text{max}}}{T_{\text{min}}}, \quad (5.6)$$

can be rewritten here as:

$$\frac{P_{\text{TM}}^{\text{out}}}{P_{\text{TE}}^{\text{out}}} = 10^{\text{ER}/10}, \quad (5.7)$$

which, when replaced in equation (5.3), yields:

$$\text{PCE} = \frac{1}{1 + 10^{-\text{ER}/10}}. \quad (5.8)$$

Again by considering the maximum (T_{max}) and the minimum (T_{min}) of the $(\cosine)^2$ function respectively as $P_{\text{TM}}^{\text{out}}$ and $P_{\text{TE}}^{\text{out}}$ at maximum conversion for a unit power TE input signal, the insertion loss of the polarization converter can be written as:

$$\begin{aligned} \text{Insertion loss (in dB)} &= 10\log \left(\frac{P_{\text{TM}}^{\text{out}} + P_{\text{TE}}^{\text{out}}}{P_{\text{total}}^{\text{in}}} \right) \\ &= 10\log (T_{\text{max}} + T_{\text{min}}). \end{aligned} \quad (5.9)$$

For each of the three sets, we measure a maximum PCE of $> 99.2 \pm 0.2 \%$ at $\lambda = 1530 \text{ nm}$ ($\text{ER} > 21 \pm 1 \text{ dB}$). Furthermore, the insertion loss for two sets ($L_{\text{tri}} =$

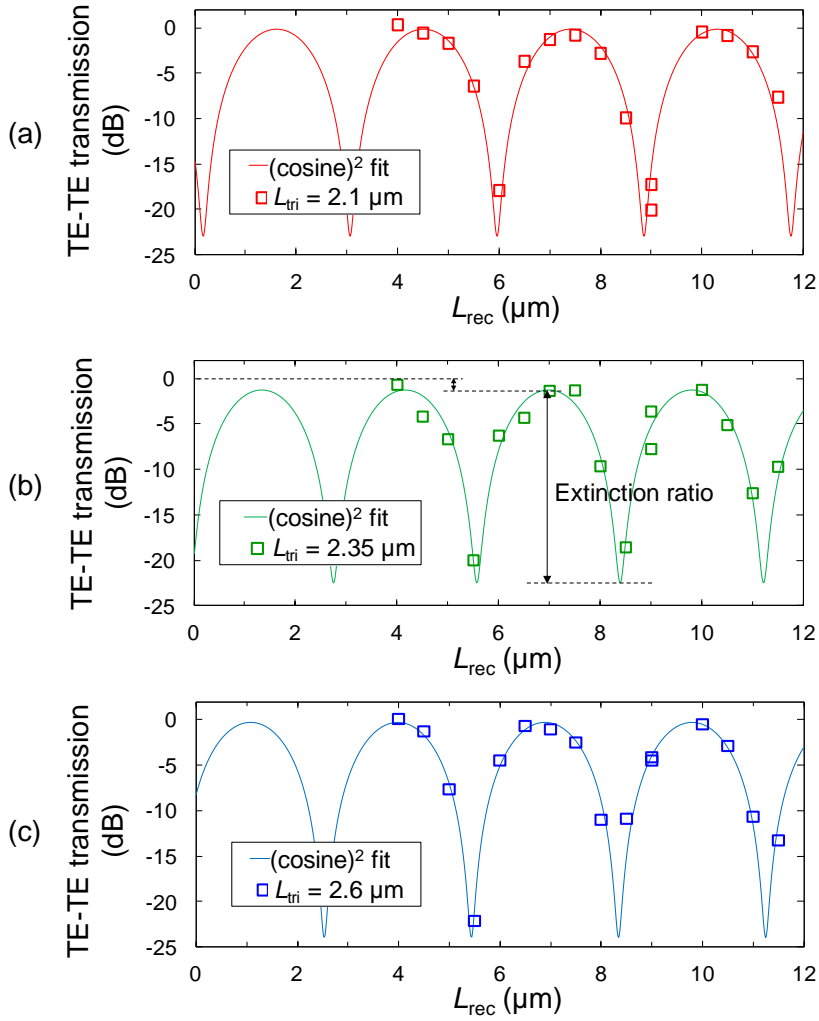


Figure 5.15: Measured TE-TE transmission of the structure of Fig.5.12 at $\lambda = 1530 \text{ nm}$ as a function of the length L_{rec} of the central rectangular section. Graphs (a), (b) and (c) correspond to three sets of structures with $L_{\text{tri}} = 2.1 \mu\text{m}$, $2.35 \mu\text{m}$ and $2.6 \mu\text{m}$, respectively.

2.1 and $2.6 \mu\text{m}$) is found to be lower than $< 0.2 \pm 1 \text{ dB}$. The uncertainty in the values of both the insertion loss and the PCE derives from variations ($\pm 1 \text{ dB}$) observed in the transmissions of reference waveguides and MMI trees distributed over the chip. We attribute these variations to unbalance in the MMIs, and local non-uniformities in the BCB bonding layer thickness which, while having no effect on the polarization conversion, are known to influence the coupling efficiency of the grating-couplers.

As expected from the design, the point $L_{\text{rec}} = 0 \mu\text{m}$ corresponds to a minimum in TE-TE transmission for the set $L_{\text{tri}} = 2.35 \mu\text{m}$. The two other sets, which do not exhibit a minimum at $L_{\text{rec}} = 0 \mu\text{m}$, will still perform well without a rectangular waveguide in between the triangular sections, but their operation wavelength will be slightly shifted.

Spectral behavior

Although limited by the bandwidth of the grating-couplers, the wavelength behavior of the three sets of devices is studied using a broadband high-power Super Luminescent Diode (SLED) source and an OSA.

The spectra of each set's 16 devices are recorded and then analyzed at each wavelength in the same way as in Fig. 5.15. The fitted (cosine)² functions obtained for each wavelength give the insertion loss and PCE versus wavelength (λ), and can be used to determine the TE-TE transmission spectrum of a device with any given L_{rec} value. Fig. 5.16 shows the PCE and insertion loss versus λ , for $L_{\text{tri}} = 2.6 \mu\text{m}$ and $L_{\text{rec}} = 2.6 \pm 0.05 \mu\text{m}$. This graph shows that for these parameters, the PCE is above $> 92\%$ and the losses below $< 1.5 \pm 1 \text{ dB}$ over the whole C-band, with a $\pm 50 \text{ nm}$ tolerance on L_{rec} .

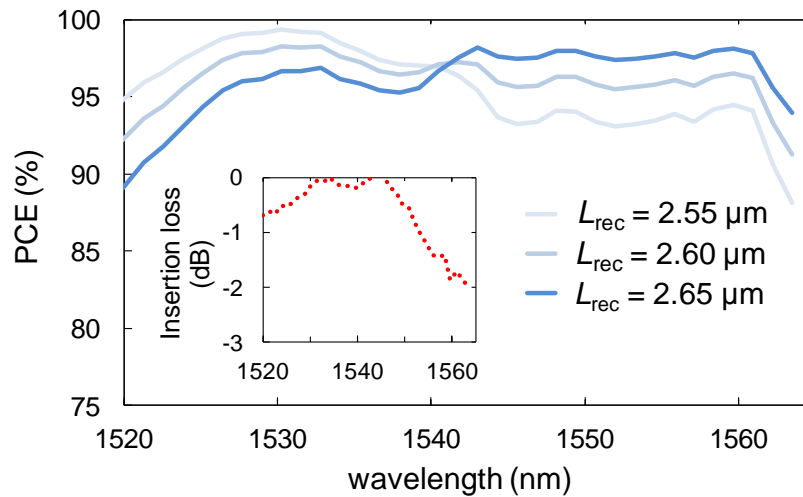


Figure 5.16: PCE and insertion loss (Inset) as a function of wavelength for the device $L_{\text{tri}} = 2.6 \mu\text{m}$ and $L_{\text{rec}} = 2.6 \pm 0.05 \mu\text{m}$.

This 35 nm bandwidth is narrower than the bandwidth predicted in the simulation section (cf. Fig. 5.5). This is attributed in part to the rectangular section introduced between the two triangular sections, which increases the effect of dispersion, and secondly to the rounding of the polarization converter pattern during fabrication (cf. Section 3.3.1), which can cause parasitic reflections and deviations from the designed polarization conversion.

5.3.3 Conclusion

In this chapter, we have presented the design of a new IMOS component, used for efficient TE to TM conversion. The device is performing very well over the whole C-band, is inherently tolerant and can be fabricated using standard InP membrane technology. The fabricated device is only $10 \mu\text{m}$ long (with less than $< 5 \mu\text{m}$ possible without the central rectangular section). The maximum measured polarization conversion efficiency is more than $> 99\%$, with losses $< 1.2 \text{ dB}$.

Chapter 5. A Polarization conversion device

This device will be used in Chapter 7 to introduce an active-passive integration scheme in IMOS, based on the polarization behavior of strained quantum wells.

Chapter 6

Wavelength selective components

In the same way as a photonic platform requires devices to control the polarization of light (cf. previous chapter), there must also be devices which act on the wavelength of light. In particular, one of the fundamental functions required for on-chip optical interconnects is wavelength (de)multiplexing. Using demultiplexers, the different signals propagating in a given waveguide can be separated (demultiplexed) into different output waveguides according to their wavelength. Conversely, demultiplexers allow signals of different wavelengths propagating in different waveguides to be combined (multiplexed) into a single waveguide.

The two devices mostly used in PICs for wavelength demultiplexing are the arrayed waveguide grating (AWG) and the planar concave grating (PCG). Both devices have been investigated in IMOS.

Another wavelength selective component, the distributed Bragg reflector (DBR), is of particular interest to create optical cavities where lasing can occur. In the following sections, we describe the DBRs and demultiplexers realized in IMOS.

6.1 Distributed Bragg Reflectors (DBRs)

A distributed Bragg reflector (DBR) is a reflector based on Bragg's law. In PICs, DBRs are implemented by varying the effective index of a waveguide periodically, along the propagation direction. As shown in Fig. 6.1, this can be achieved by a periodic variation of the waveguide width or height. Each periodic discontinuity creates a partial reflection of the guided light. For guided waves with a wavelength close to twice the optical period of the DBR, these partial reflections interfere constructively

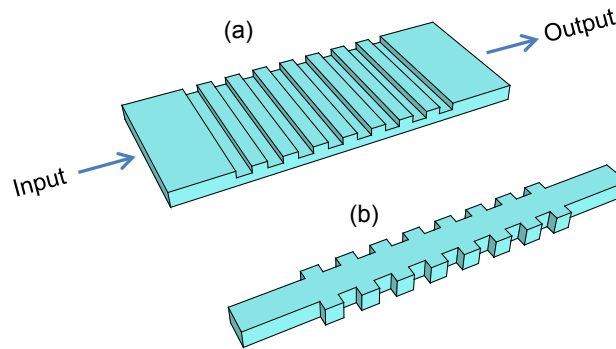


Figure 6.1: Diagrams representing IMOS distributed Bragg reflectors (DBRs) implemented using top-corrugation (a), and sidewall-corrugation (b), respectively.

and add up, creating a strong reflection. If the DBR contains enough periods, there is a range of wavelengths for which light is fully reflected and cannot propagate further in the structure. The DBR then acts as a 1D photonic crystal, and this range of wavelengths is called "photonic stopband".

Due to their controllable and potentially high reflectivity, DBRs are often used to create laser cavities [7, 8]. Furthermore, the wavelength dependence of the DBR behavior makes them interesting for wavelength demultiplexing applications. In IMOS, the first targeted application of DBRs is a strong reflector for creating laser cavities. Therefore, we describe below the design and fabrication of DBRs with reflectivities of 50 % to 99 %, at $\lambda = 1550$ nm, for TE or TM polarization.

6.1.1 Design

In this work, we focused on the top-corrugation DBR design. Top-corrugation DBRs are designed using CAMFR, the 2D eigenmodes expansion simulation tool also used for designing grating-couplers, (cf. Chapter 2). In Fig.6.2, we show the results obtained during the design of a top-corrugation DBR for TE polarization at $\lambda = 1550$ nm. The membrane thickness is set to 300 nm, one of the standard IMOS membrane thickness values. By choosing the same etch depth for the DBR grooves and the grating-couplers, the DBR can be fabricated in IMOS without adding any extra step to the standard passive process-flow. Therefore, the DBR grooves etch depth is set to 120 nm. After setting the DBR filling factor to 50 %, the pitch size is swept from 0.28 to 0.36 μm (cf. Fig.6.2(a)), to locate the maximum in reflectivity at $\lambda = 1550$ nm. This maximum is found to occur at a pitch of around 0.30 μm . After setting the pitch size to this value, we sweep the wavelength to obtain the spectral response of the device, for 10, 20 and 25 periods (cf. Fig.6.2(b)).

The resulting spectrum shows that the device has a ~ 100 nm-wide reflection stopband centered at $\lambda = 1540$ nm, with reflectivities between 60 % and 90 %, depending on the number of periods. As expected, the higher the number of periods, the stronger the reflectivity. However increasing the number of periods beyond 25 doesn't increase the reflectivity much. Therefore, a strong DBR reflector in IMOS can be as short at 7.5 μm . Furthermore, the simulated DBR loss is always below 1 dB, and can be as low as 0.1 dB near the maximum of the reflection stopband

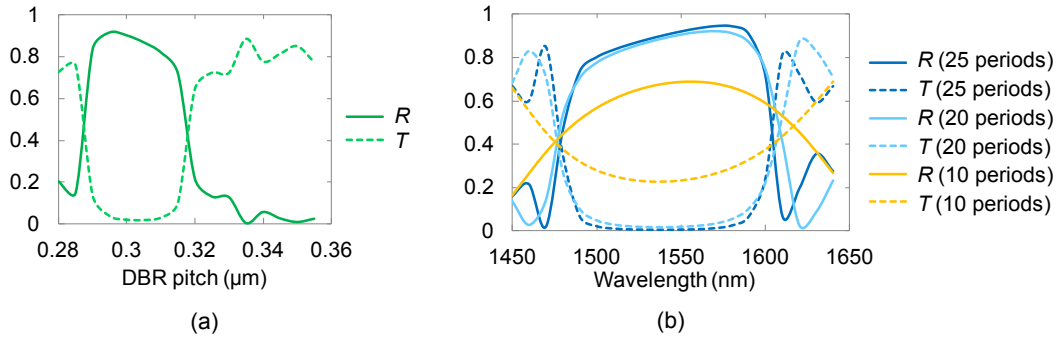


Figure 6.2: Design of a top-corrugation DBR using CAMFR. (a) Change in the reflectivity and transmissivity of a 20 period DBR at $\lambda = 1550$ nm, when sweeping the pitch size from 0.28 to 0.36 μm . (b) Spectral response of the DBR for different numbers of periods after setting the pitch size to 0.30 μm .

Memb.thick.	pol.	pitch	etch.depth	fill.fac.	#periods	Rmax	3dB bandw.
[nm]	-	[nm]	[nm]	[%]	-	[%]	[nm]
300	TE	300	120	50	10	69	1465-1635
					25	94	1480-1605
250	TE	315	100	50	25	96	1475-1605
	TM	440	100	50	25	62	1525-1580
					50	98	1540-1570

Table 6.1: Interesting DBRs for IMOS, simulated with CAMFR.

($\lambda = 1570$ nm).

In table 6.1, we sum up the dimensions of a few interesting top-corrugation DBR designs for IMOS.

Since our CAMFR simulations are only able to represent 2-dimensional structures, the width of the DBR is not taken into account during the design. However, fabricated DBRs have a finite width which influences the device's performance. In theory, the wider the device, the closer its fundamental mode is to a plane wave and the better its interaction with the DBR corrugation. This is confirmed by measurements carried out on fabricated DBRs, which showed 90 % reflectivity for a DBR of width $w = 2.5$ μm , whereas almost no reflection was observed for an otherwise identical DBR of width $w = 0.45$ μm (the standard IMOS waveguide width). This means that in the circuit layout, tapers have to be used to connect standard IMOS waveguides to a top-corrugation DBR, leading to a longer device length.

In the following sections, we describe the fabrication and characterization of a top-corrugation DBR with a width of $w = 2.5$ μm . The device is connected to the standard IMOS waveguides using 30 μm long linear tapers.

6.1.2 Fabrication

As mentioned in the previous section, top-corrugation DBRs in IMOS can be fabricated using the standard passive process-flow. The lateral trenches of the DBRs

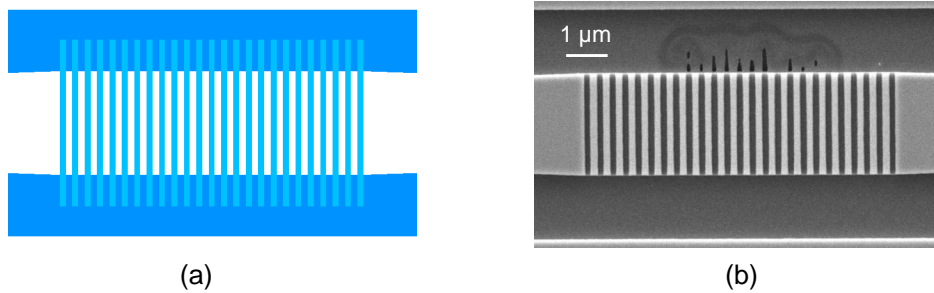


Figure 6.3: (a) GDS layout, and (b) top-view SEM picture of a 25-period top-corrugation DBR with a pitch of 300 nm, fabricated in IMOS.

are etched together with the trenches of the passive circuit. Subsequently, the DBR grooves are etched at the same time as the grating-couplers. Fig. 6.3 shows the GDS layout and a SEM picture of a top-corrugation DBR, fabricated in IMOS.

As usual when using EBL in nanofabrication, an important factor to consider is the dose applied to different parts of the design. To fabricate top-corrugation DBRs on a pre-bonded IMOS membrane using ZEP as the resist, we found that the trenches could be printed with $38 \mu\text{C}/\text{cm}^2$ (the same dose as the one used for printing standard IMOS waveguide trenches), while the DBR grooves require a higher dose of 42–46 $\mu\text{C}/\text{cm}^2$, depending on the DBR pitch.

The alignment accuracy between the two EBL steps can be relaxed by making the grooves overlap with the trenches by a few hundred nanometers. In this way, any misalignment smaller than this overlap dimension will result in the DBR grooves being printed over the entire waveguide width. However, one has to keep in mind that the regions where trenches and grooves overlap are etched twice. This means that in these regions, there is no InP left on top of the SiO₂ undercladding. Since SiO₂ is etched in BHF, subsequent BHF wet etching (e.g. for SiN hard mask removal), will attack the SiO₂ undercladding. Such an attack can be seen in Fig. 6.3, where regions etched twice (appearing black) are surrounded by rings of dark gray color indicating a 1 μm underetch of the SiO₂ undercladding. To avoid this problem, one has to limit the number of steps involving HF, following the DBR fabrication. (For instance, the SiN hard mask can be removed by dry etching.)

6.1.3 Characterization

4-port characterization structure

In order to determine the performance of the fabricated DBRs, we used the 4-port structure presented in Fig. 6.4. Such a structure enables to acquire two independent measurements of the power reflected by the DBR, and two independent measurements of the power transmitted through the DBR. Assuming that the losses in the DBR are negligible (this will be shown to be legitimate close to the maximum of the stopband), an adequately chosen ratio of these four measurements can then be used to clear off the unknown loss contributions in the structure's four arms (α_1 , α_2 , α_3 and α_4), and obtain the actual reflection coefficient R of the DBR.

With α_{MMI} (~ 0.5) the power transmission through the MMI, P_{in} the power

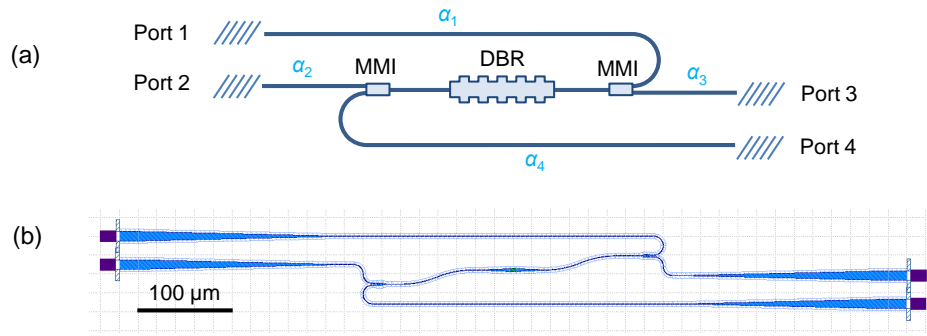


Figure 6.4: (a) Schematic and (b) actual layout of the 4-port structure used for DBR characterization.

coming from the input fiber, and R , T , the reflection and transmission coefficients of the DBR, the powers P_{ij} measured when placing the fibers between port i and port j can be written as:

$$\begin{cases} P_{13} = \alpha_1 \alpha_3 \alpha_{\text{MMI}}^2 R P_{\text{in}} \\ P_{14} = \alpha_1 \alpha_4 \alpha_{\text{MMI}}^2 T P_{\text{in}} \\ P_{23} = \alpha_2 \alpha_3 \alpha_{\text{MMI}}^2 T P_{\text{in}} \\ P_{24} = \alpha_2 \alpha_4 \alpha_{\text{MMI}}^2 R P_{\text{in}} \end{cases} \quad (6.1)$$

If one then assumes that the losses in the DBR are negligible (in the design section, this is shown to be true close to the maximum of the stopband), we have $R + T \simeq 1$. Thus, we can write:

$$B = \frac{P_{14} P_{23}}{P_{13} P_{24}} = \frac{(1 - R)^2}{R^2}. \quad (6.2)$$

This is a simple quadratic equation in R , of which only one solution is physically significant (we must have $R \in [0, 1]$ and $B > 0$). This solution is:

$$R = \frac{1 - \sqrt{B}}{1 + B}. \quad (6.3)$$

Results

A 25-period top-corrugation DBR designed for TE polarization is fabricated in a 300 nm InP membrane, with a pitch of 300 nm, a filling factor of 45%, and an etch depth of 120 nm, and characterized using the 4-port characterization structure described above.

Fig. 6.5(a) and (b) show the transmission data acquired when feeding the ASE light of an EDFA in a 4-port characterization structure without DBR, and with the fabricated DBR respectively. By symmetry of the structure, we always have $P_{13} \simeq P_{24}$, while, due to the 0.65 mm length difference in the ports 1-to-4 and ports 2-to-3 paths (cf. Fig. 6.4(b)), $P_{23} > P_{14}$.

For the control 4-port characterization structure without DBR (see Fig. 6.5(a)), P_{23} (respectively P_{14}) is equivalent to the transmission through a 0.85 mm long (respectively 1.5 mm long) waveguide with 6 dB extra loss due to the two MMI cou-

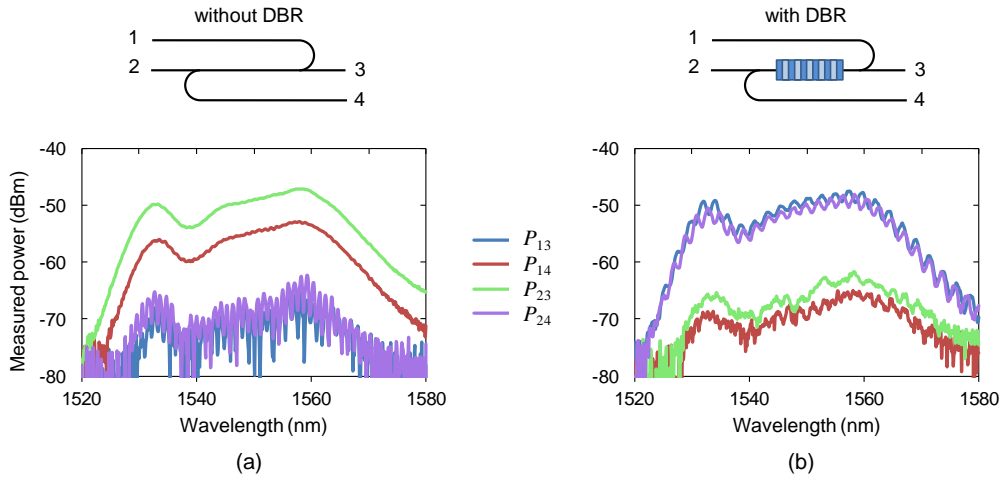


Figure 6.5: Measured transmission spectra of a control 4-port characterization structures without DBR (a), and of a 4-port characterization structure with DBR (b), using the ASE of an EDFA as the input signal. The 25-period DBR was fabricated in a 300 nm thick InP membrane, with a 300 nm pitch, a 45% filling factor, and an etch depth of 120 nm.

plers. That is why P_{23} and P_{14} are relatively strong signals. The passive losses on the chip were measured independently to be around $\alpha_{\text{dB}} = 2 \text{ dB}\cdot\text{mm}^{-1}$. Therefore, the difference in transmission between P_{23} and P_{14} should be around $\alpha_{\text{dB}} \times 0.65 \text{ mm} = 1.3 \text{ dB}$. The measured transmission difference of 6 dB suggests either a difference in coupling during the measurements, or a damage in the waveguide of port 1 or port 4.

Since no DBR is present in this control structure, P_{13} and P_{24} are expected to be close to 0. However, for both of them, a weak signal can still be picked up, caused by parasitic reflection in the MMI couplers. Indeed, the fringes appearing in both P_{13} and P_{24} have a period of $\Delta\lambda = 1.08 \text{ nm}$, corresponding to the resonances of a Fabry-Pérot cavity of length* $L = \frac{\lambda^2}{2N_{\text{group}}\Delta\lambda} = 0.291 \text{ mm}$, which corresponds to the waveguide distance between the two MMI splitters (cf. Fig. 6.4(b)).

For the 4-port characterization structure containing a DBR (see Fig. 6.5(b)), the trend is reversed. P_{13} and P_{24} are now powerful signals with a level comparable to the P_{23} transmission of the case without DBR, whereas, P_{23} and P_{14} are about 15 dB lower. This indicates that the fabricated DBR has a strong reflection coefficient, and a low insertion loss. The ripples appearing in P_{13} and P_{24} are due to the Fabry-Pérot cavities formed between the right MMI coupler and the DBR, and between the left MMI coupler and the DBR, respectively. Furthermore, this time the difference between P_{23} and P_{14} is closer to the value of 1.3 dB calculated using α_{dB} and the length difference between the ports 2-to-3 and ports 1-to-4 paths.

In order to obtain a quantitative estimate of the fabricated DBR's reflection and transmission coefficients R and T , the data presented in Fig. 6.5 is processed as follows:

- The ratio $T_{\text{meas}} = \frac{P_{23}^{\text{with DBR}}}{P_{23}^{\text{without DBR}}}$ provides a direct measurement of T .

* N_{group} was determined using ring resonators and MZIs (cf. Section 3.2), fabricated on the same chip.

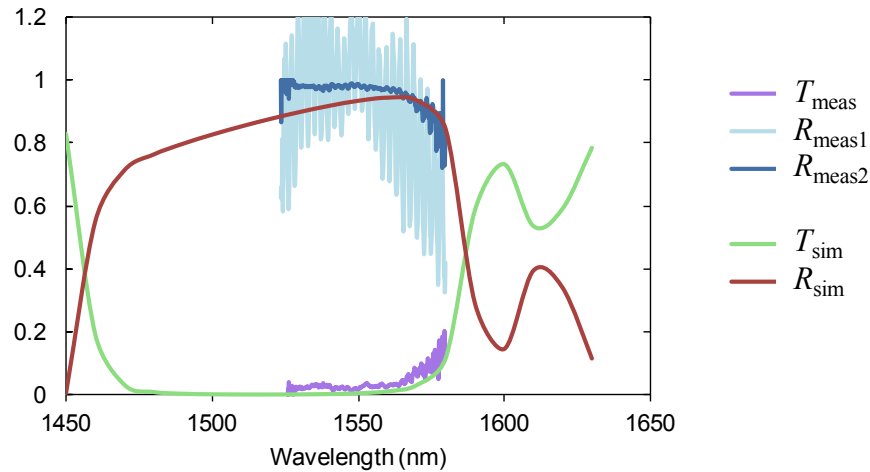


Figure 6.6: Wavelength dependence of the reflection and transmission coefficients of an IMOS DBR, obtained by processing of the measurement data shown in Fig.6.5 (T_{meas} , R_{meas1} and R_{meas2}), and CAMFR simulations (T_{sim} and R_{sim}).

- R can also be directly estimated by the quantity $R_{\text{meas1}} = \frac{P_{13}^{\text{with DBR}} \times 10^{\alpha_{\text{dB}} \Delta L / 10}}{P_{23}^{\text{without DBR}}}$, where $\alpha_{\text{dB}} = 2 \text{ dB} \cdot \text{mm}^{-1}$ is the independently measured waveguide propagation loss, and $\Delta L = 0.3 \text{ mm}$ is the length difference between the ports 1-to-3 and ports 2-to-3 paths.
- Finally, as shown in the previous section, the quantity $R_{\text{meas2}} = \frac{1 - \sqrt{B}}{1 - B}$, with $B = \frac{P_{14}^{\text{with DBR}} P_{23}^{\text{with DBR}}}{P_{13}^{\text{with DBR}} P_{24}^{\text{with DBR}}}$, provides an other estimate of R , which is more robust since it intrinsically cancels the loss contributions in each port, but at the price of neglecting the losses in the DBR.

In Fig.6.6, these three quantities T_{meas} , R_{meas1} and R_{meas2} are plotted alongside their simulated counterparts T_{sim} and R_{sim} , obtained using CAMFR.

We observe a near-perfect agreement between T_{meas} and T_{sim} over the measured wavelength range (1520 to 1580 nm). In particular, the end of the DBR reflection stopband after $\lambda = 1560 \text{ nm}$, where T starts to increase, matches very well the simulated spectrum. R_{meas1} also follows the trend of R_{sim} , however the noise due to the parasitic reflections in the MMI splitter makes it hard to read precise values of the reflection coefficient on the graph. Finally, the graph of quantity R_{meas2} also follows the simulated shape of the DBR reflection stopband. Since the FP resonances are contained in the parameters α_1 , α_2 , α_3 and α_4 , they cancel out during post-processing, making R_{meas2} much smoother than R_{meas1} . However, R_{meas2} of course deviates from the simulated spectrum R_{sim} , when the losses inside the DBR are shown by the simulations to be non-negligible (away from the stopband maximum at $\lambda = 1560 \text{ nm}$).

6.1.4 Conclusion

We have designed and fabricated a top-corrugation DBR for TE polarization in IMOS. The maximum of the measured reflectivity is on the order of 90% at $\lambda = 1550 \text{ nm}$,

and the spectrum matches the design closely. Since it can be fabricated in the same steps as the standard IMOS waveguides and grating-couplers, this device doesn't add any extra step to the IMOS fabrication process-flow. This device will be used in Section 7.3.2 to demonstrate the first IMOS laser realized in our group. Finally, it is expected that by varying the geometrical properties of this device (pitch, filling factor and number of periods), TE and TM reflectors of varying strengths and bandwidths can be produced to fit the requirements of different applications.

In the next section, we describe two devices that can be used for wavelength demultiplexing in IMOS.

6.2 Wavelength demultiplexers

6.2.1 Arrayed Waveguide Grating (AWG)

First demonstrated in 1988 [41], the Arrayed Waveguide Grating (AWG) is the most commonly used demultiplexer device in PICs. It uses the imaging and dispersion properties of an array of waveguides to image the different wavelengths present in an input waveguide onto different output waveguides.

The mask layout of an AWG is shown in Fig. 6.7(a). The device consists of two symmetric un-etched free propagation regions (FPRs) connected through an array of delay waveguides. The light diffracting out of the input waveguide spreads in the first FPR with a diverging curved phase-front, and is picked up by the array of delay waveguides placed on this phase-front. The length increment ΔL between the delay waveguides is chosen such that for the center wavelength λ_0 of the AWG, the phase delay in each arm equals $m \cdot 2\pi$, where m is an integer. Therefore, the field distribution at the output aperture is the same as the field at the input aperture, except that the phase-front is now a converging one. The λ_0 light coming out of the array therefore focuses in the center of the image plane, where it can be collected by an output waveguide. For other wavelengths near λ_0 , the phase delay in each arm is not a multiple of 2π anymore and the phase-front at the end of the array of delay waveguides is tilted. As a result, the focusing of the light occurs at other positions, where it can be collected by different output waveguides.

Fig. 6.7(b) shows two identical AWGs fabricated on the IMOS platform. The designed channel spacing of the device[†] is 500 GHz (4 nm) and the FSR, 32 nm. Fig. 6.8 shows the measured transmission spectrum of the device. A demultiplexing behavior can be observed, with an FSR of 32.6 nm and a channel spacing of 3.96 nm, very close to their design values. However, the spectrum is very distorted and the losses very high (~ -15 dB). The most probable cause for this is that sidewall roughness and EBL stitching in the array of delay waveguides create phase noise which disrupts the imaging performance of the AWG.

This problem can be solved by improving the fabrication technology in order to significantly reduce the roughness of the waveguides and the stitching. Alternatively, another demultiplexer design called Planar Concave Grating (PCG), where the dispersion is achieved using a planar grating, can be considered to circumvent the use

[†]Muhammad Muneeb (Ghent University – IMEC) designed this AWG, as well as the PCG described in the next section.

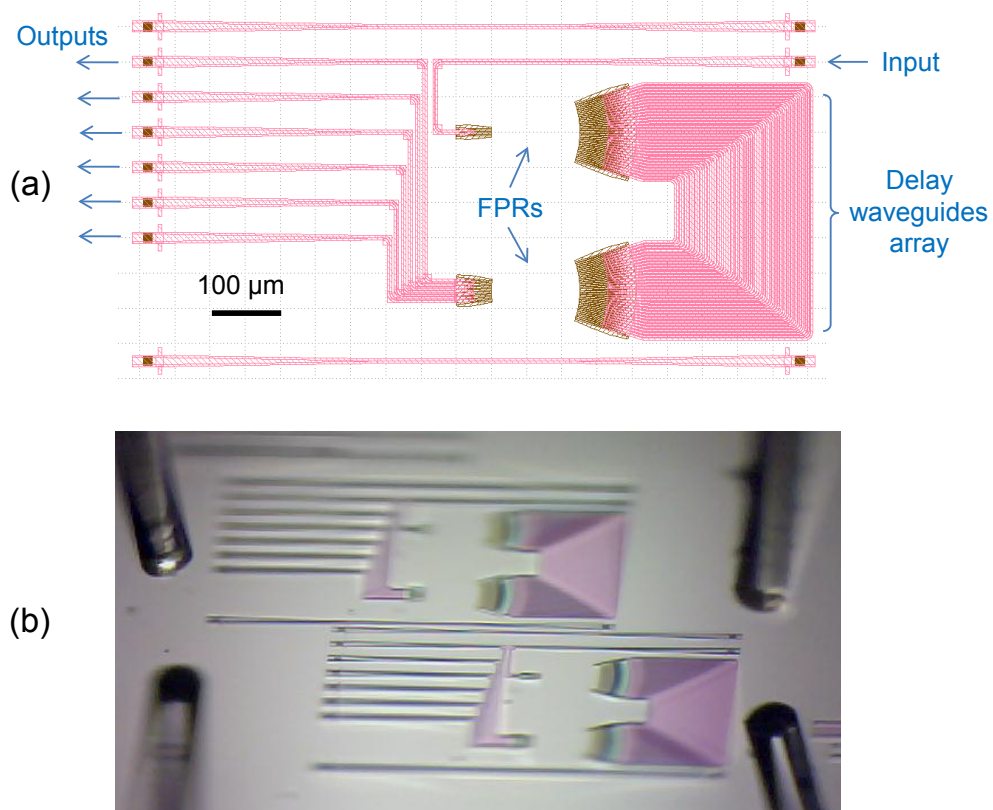


Figure 6.7: (a) Layout of an IMOS AWG demultiplexer (FPR = free propagation region). (b) 45° aerial microscope image of two fabricated AWGs.

of waveguides altogether.

6.2.2 Planar Concave Grating (PCG)

Design

A PCG demultiplexer (also referred to as Echelle grating, or etched diffraction grating) functions by combining the high dispersion of a large period grating, with the focusing power of a concave mirror. As shown in Fig. 6.9, the light coming from the input waveguide spreads in an un-etched free-propagation region (FPR) and reaches the PCG, where it is simultaneously reflected and diffracted by the grating corrugation, and re-focused by its curvature. Due to the inherent dispersion of the grating, different wavelengths are diffracted in different directions, and can therefore be collected separately by several output waveguides placed on the so-called Rowland circle (see [42], for more detail on the design and behavior of PCG demultiplexers).

An eight-channel PCG demultiplexer is designed for TE-polarized light, with a central wavelength of 1550 nm, and a channel spacing of 4.0 nm. In order to reduce the insertion loss of the device, the transitions between waveguides and the FPR are optimized using deep and shallow etching (cf. Fig. 6.10(i)), and the reflectivity of the PCG's facets is maximized using DBRs (cf. Fig. 6.10(ii)). According to CAMFR simulations, a six-period DBR with 350 nm period, 50% filling factor, and 250 nm

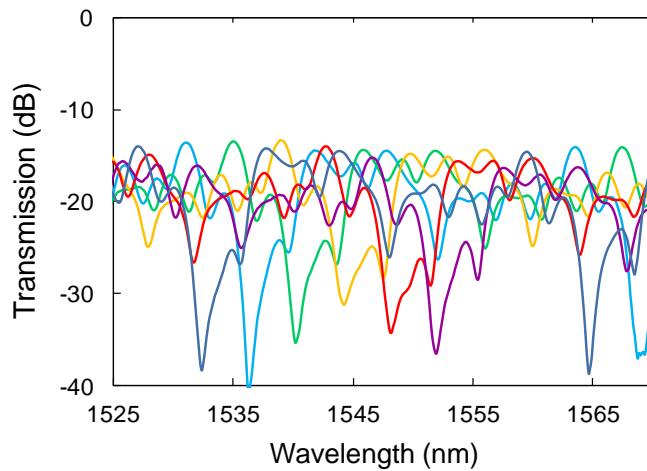


Figure 6.8: Measured transmission spectrum through the 6 ports of the AWG pictured in Fig.6.7.

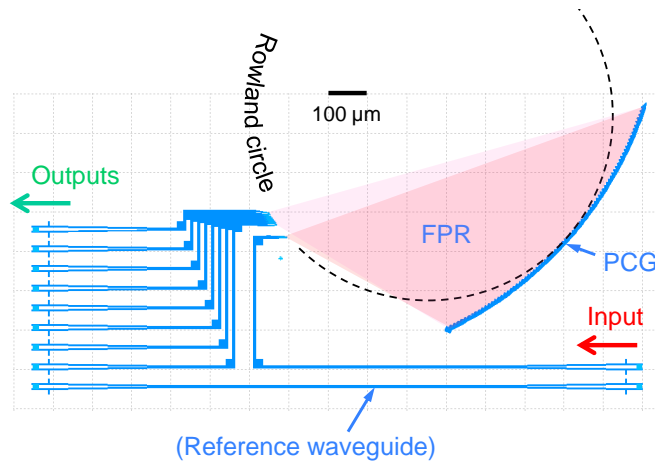


Figure 6.9: Layout of an IMOS PCG demultiplexer

etch depth can provide above 90% power reflection in the 1520 to 1620 nm wavelength range.

Fabrication

Like other devices demonstrated on the IMOS platform [12], the PCG demultiplexer is fabricated in a 300 nm thick InP membrane after the latter has been bonded to a silicon carrier wafer (see Section 2.3 for more detail on the IMOS post-bonding fabrication scheme).

Fig.6.10 shows a 45° aerial microscope image (as seen during the measurements) of the PCG demultiplexer fabricated according to the layout of Fig.6.9. Fig.6.10(i) shows the deep-shallow transition designed to optimize the coupling from the input waveguide to the FPR of the PCG. The overlap regions between shallow and deep areas have been etched twice. Therefore there is no InP left in these overlap regions and the underlying SiO₂ cladding is exposed to the air, charging and showing up bright on the SEM picture. In this case, it is very important to avoid prolonged exposure of

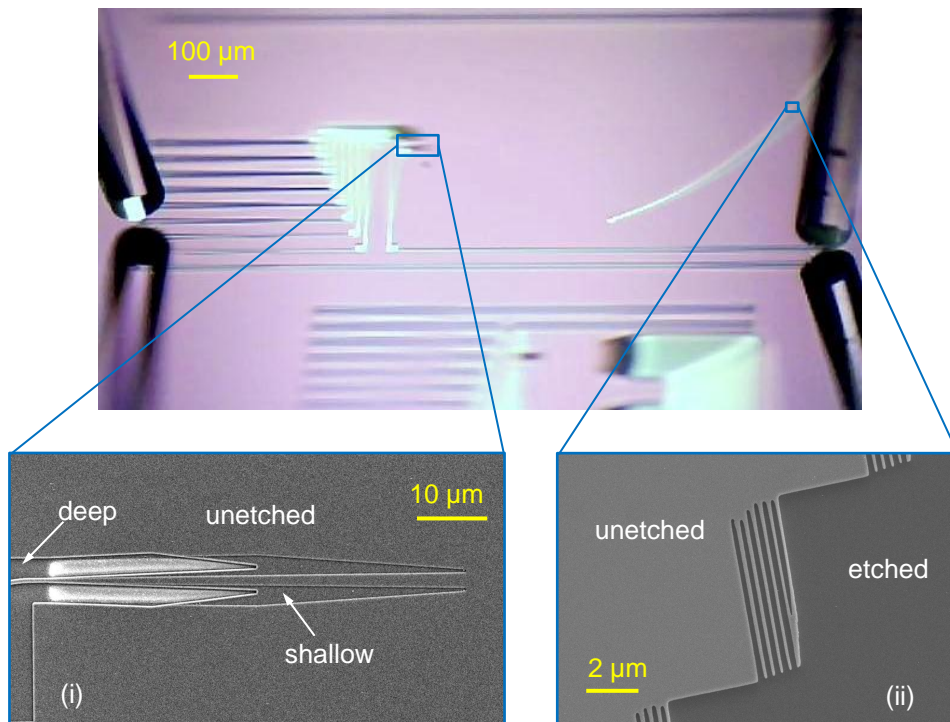


Figure 6.10: 45° aerial microscope image of the fabricated PCG demultiplexer. (i) SEM picture of the PCG input waveguide-to-FPR transition. (ii) SEM picture of a DBR facet of the PCG.

the chip to HF, as it will etch the SiO₂ cladding under the waveguides and damage the III-V structure during drying, due to strong capillary forces [43] (see Fig.6.11).

Fig.6.10(ii) shows a DBR facet of the PCG. In order to obtain a high reflection, it is important for the fabricated DBR to match closely its designed dimensions (in this case, 350 nm period, 50% filling factor, and 250 nm etch depth). Since EBL is prone to proximity effects [44], the exposure dose of the DBR grooves has to be adjusted to obtain an acceptable dimension control (see Fig.6.12). The exposed pattern after correction is still not matching perfectly the design, especially in the top-left and bottom-right corners of the DBR (cf. Fig.6.10(ii)), where the effective exposure dose is still too low, and too high, respectively. However, as will be shown in the characterization section, the well-defined central part of the DBR is good enough to create the high reflection needed.

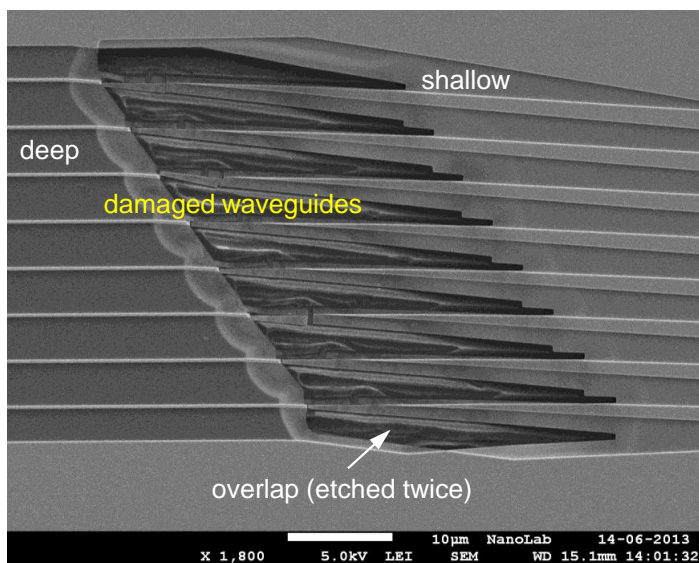


Figure 6.11: Output waveguides of the PCG destroyed by the strong capillary forces occurring after removal of the SiO₂ under-cladding by HF, subsequent rinsing in DI water, and blow-drying of the sample.

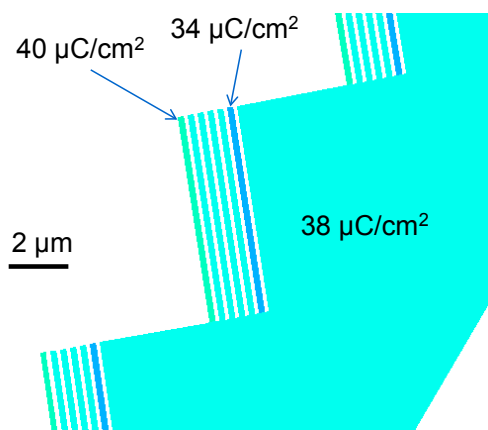


Figure 6.12: Excerpt of the GDS file used to print the DBR depicted in Fig. 6.10(i), showing the proximity effect correction (PEC) applied to improve the printed pattern.

Characterization

In order to assess the performance of the fabricated PCG demultiplexer, the light of an amplified spontaneous emission source covering the C-band (1530 to 1565 nm) is fed into the device's input. The spectrum of the light collected by each of the device's output ports is then recorded using an OSA, and normalized to the spectrum of a reference waveguide fabricated next to the PCG demultiplexer (cf. Fig. 6.9).

Fig. 6.13 shows both the designed (a), and the measured (b) transmission spectrum of the device. In the measured spectrum, each channel's central lobe matches very well the predicted Gaussian shape. The channel spacing of the measured device (3.96 nm) is close to the designed value of 4.0 nm. The spectrum is blue-shifted by 4.1 nm with respect to the designed spectrum, and the insertion losses (2.8 dB) are higher than the value predicted in our simulations (0.2 dB).

The wavelength shift is caused by a deviation of the membrane thickness from the design value. The extra insertion loss arises due to fabrication imperfections in the PCG's DBRs, including trench width variation, roughness, e-beam proximity effects (cf. Fig. 6.10(ii)), and to a lesser extent, non-verticality [45]. Furthermore, each channel of the measured spectrum presents sidelobes on both sides of the central transmission peak, which can best be seen when superimposing the eight output channels of the device, as in Fig. 6.14. These sidelobes originate from the phase noise created by membrane thickness non-uniformity, and by the DBRs fabrication imperfections described above. However, their transmission level does not exceed -21.3 dB, meaning that the cross-talk figure for our device is better than -18 dB. Finally, the power non-uniformity between the different channels is below 1.2 dB.

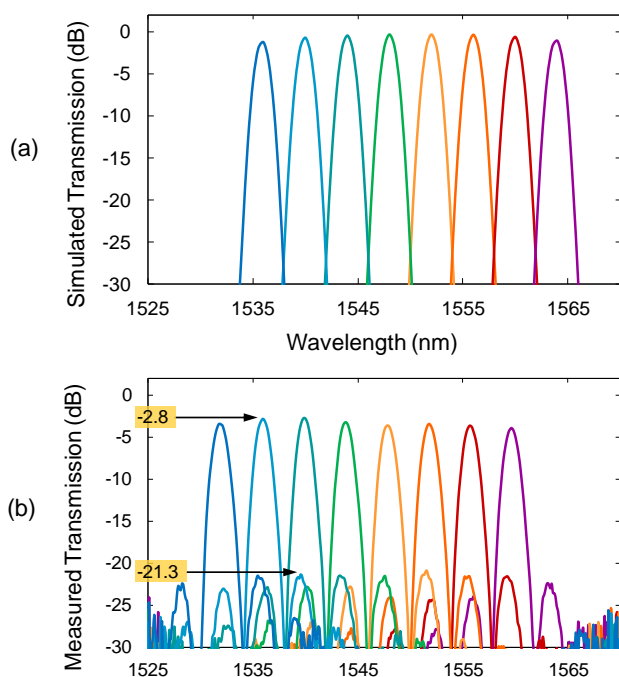


Figure 6.13: (a) Designed transmission spectrum of the IMOS PCG demultiplexer. (b) Measured transmission spectrum of the fabricated device. (Axes scales in both graphs are identical to facilitate comparison.)

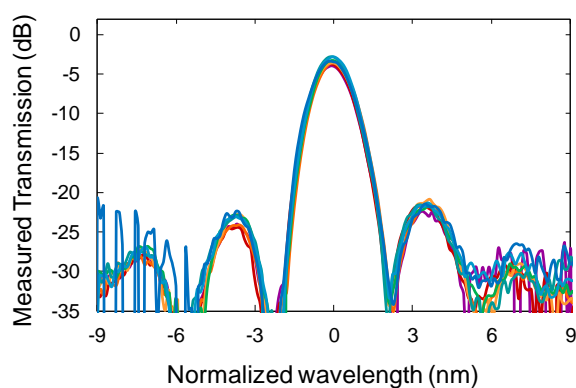


Figure 6.14: Superimposed transmission spectra of the fabricated PCG demultiplexer's eight channels, showing a very good overlap and a maximum transmission power non-uniformity of 1.2 dB.

6.2.3 Conclusion

In order to provide IMOS with a demultiplexing device, an AWG and a PCG were designed and fabricated. The first attempt at making an AWG in IMOS failed due to the sidewall roughness and EBL stitching during fabrication. However, we have demonstrated the first successful PCG demultiplexer fabricated on an InP-based photonic membrane platform. The device shows 2.8 dB insertion loss, 1.2 dB channel non-uniformity and -18 dB cross-talk. It is a key component that can be applied in WDM signal processing, and in multi-wavelength lasers.

Chapter 7

The POLIS active-passive integration scheme

In the previous chapters, we have demonstrated a number of devices used for light guiding, memory applications, polarization conversion, and wavelength control. The final step to create a full photonic platform is to demonstrate devices able to generate and amplify light. As explained in Chapter 2, several active-passive integration schemes are available in IMOS. In this thesis, we focused on the POLIS scheme, because the regrowth technology for butt-joint integration in membranes was not yet available in COBRA, and because it connects smoothly with the processing developed for the polarization converter (cf. Chapter 5).

In the following sections, a detailed description of the POLIS material and its properties is given, then some laser designs are described for integration in this scheme, and finally, preliminary experimental results are presented, including the demonstration of the first IMOS laser fabricated in the PhI group.

7.1 POLIS Material analysis

7.1.1 POLIS principle

As mentioned in the introduction of this chapter, the POLIS integration scheme relies on the polarization behavior of strained QWs. In semiconductors, TM absorption is caused by light hole transitions, while TE absorption is caused both by light hole ($\sim 25\%$) and heavy hole ($\sim 75\%$) transitions [46, 17]. Fig. 7.1 represents qualitatively the separation of the light hole and heavy hole subbands for compressive, zero and tensile strain, respectively. Under compressive strain, the heavy hole subband lies

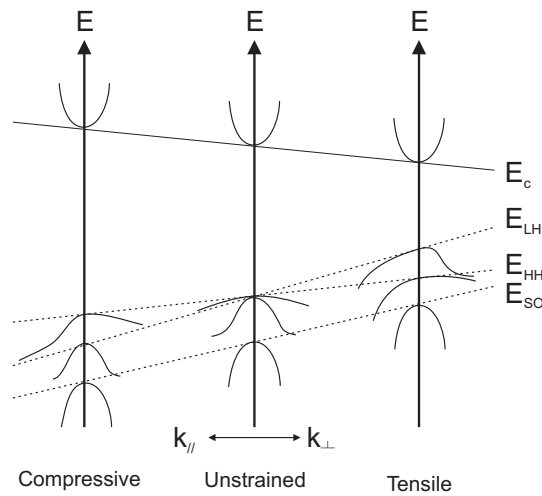


Figure 7.1: Influence of strain on the band structure of quantum wells [47]

above the light hole subband. Therefore, there is a range of energies in which only heavy hole transitions are possible. For this wavelength region, TM-transparency and TE-absorption are achieved simultaneously. Note that under tensile strain, the light hole subband is raised above the heavy hole subband. The bandgap is then the same for the two polarizations. Therefore, the POLIS concept can only work with compressive strain.

The higher the strain in the QW, the larger the separation between the light hole and heavy hole subbands. However, if the strain in the QW is too high, local relaxation will occur in the material, causing optical loss. In order to benefit from the POLIS effect over a wide wavelength range, while maintaining the quality of the QW, a strain of 0.9 % is a good compromise [17]. This strain, as well as an emission centered around $\lambda = 1550$ nm, can be obtained in a ~ 2 nm thick $\text{Ga}_{0.34}\text{In}_{0.66}\text{As}$ quantum well. With these parameters, an optical bandwidth of 150 nm can be obtained in which the POLIS effect exists.

7.1.2 POLIS layer-stack

In order to realize the first POLIS experiments on the IMOS platform, the layer-stack shown in table 7.1 is grown on an InP substrate*. Layer 1 is a sacrificial layer used to protect the bonded membrane during substrate removal. Layers 4-8 form the membrane used for standard IMOS waveguides. Layer 2 is lightly n-doped, to be used both as n-contact for electrical pumping, and for the fabrication of polarization converters (cf. Chapter 5). Layers 9-11 were designed for creating the p-contact of active devices. However, as will be shown in Section 7.2.3, carrier injection in the QW can be improved by modifying these layers.

*Epitaxy realized by René van Veldhoven, from the PSN group (TU/e)

Layer	Material	Function	Thickness [nm]	Doping [cm^{-3}]
12	InP	cap layer	30	n.i.d.
11	InGaAs	p-contact	100	$p = 1 \times 10^{19}$
10	InP	p-contact	10	$p = 5 \times 10^{17}$
9	Q(1.25)	p-contact	130	graded to $p = 1 \times 10^{18}$
8	InP	membrane	115	n.i.d.
7	Q(1.25)	barrier	10	n.i.d.
6	$\text{Ga}_{0.34}\text{In}_{0.66}\text{As}$	strained QW	1.8	n.i.d.
5	Q(1.25)	barrier	10	n.i.d.
4	InP	membrane	115	n.i.d.
3	Q(1.25)	etch-stop	20	n.i.d.
2	InP	n-contact	130	$n = 5 \times 10^{18}$
1	InGaAs	sacrificial	500	n.i.d.
	InP	substrate		

Table 7.1: Layer-stack of the wafer used for the experiments shown in Section 7.3. The POLIS quantum well is highlighted in red.

7.1.3 Photoluminescence (PL)

Photoluminescence (PL) is a useful technique to characterize the quality of semiconductor materials. When light with a photon energy larger than the bandgap energy E_g is entering the material, photons are absorbed and electrons are raised to higher energy states. These electrons eventually return to the ground state, thereby emitting a photon when the transition is radiative. These emitted photons form the photoluminescence (PL) of the material, and their spectral distribution shows a peak at the bandgap energy. Fig. 7.2 shows the PL spectrum of the POLIS QW at room temperature. Since the PL excitation light is emitted in the direction normal to the wafer, we

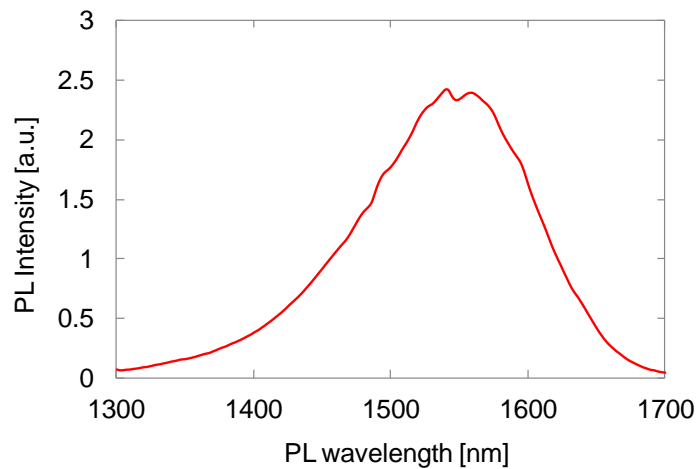


Figure 7.2: Room temperature photoluminescence (PL) spectrum of the POLIS QW.

can only monitor the TE emission of the QW. The peak of the TE emission spectrum appears at $\lambda = 1550$ nm, where future lasers should operate.

While the POLIS scheme has been shown to function on a bulk InP platform [17], one of the concerns when moving to IMOS is whether the strain, and thus the POLIS effect, can be conserved after bonding the membrane and removing the substrate. In order to investigate this, a piece of the layer-stack shown in table 7.1, with only layers 4 to 8 (all contact layers removed), is bonded on silicon. Waveguides of different lengths are printed on the sample, with either TE or TM grating couplers.

Fig. 7.3 shows the measured TE absorption spectrum of the fabricated waveguides. Since SEM inspection of the waveguides didn't reveal any important rough-

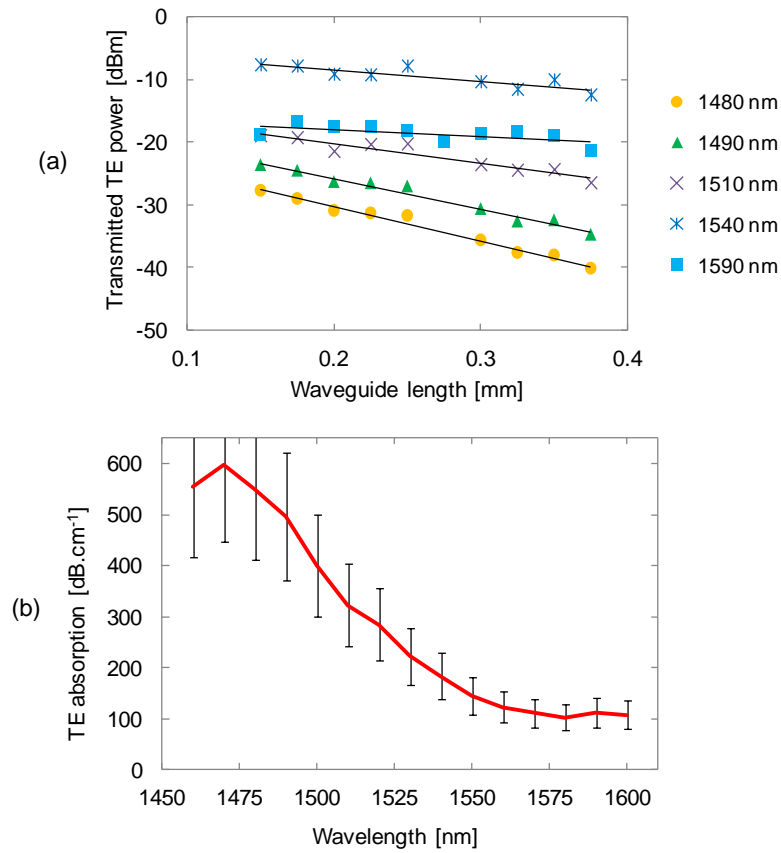


Figure 7.3: (a) TE power transmitted through POLIS waveguides of different lengths. (b) TE modal absorption in the POLIS waveguide as a function of wavelength (obtained by fitting the data shown in (a)).

ness or defects, the waveguide scattering loss is expected to be below 20 dB.cm^{-1} (cf. Section 3.2). The measured modal absorption of $100\text{-}600 \text{ dB.cm}^{-1}$ between $\lambda = 1460$ and 1600 nm is thus almost entirely caused by the strained QW. The overlap of the waveguide mode with the QW is around 1 %. Therefore, the measured modal absorption corresponds to a QW absorption in this wavelength range of $2\text{-}14 \times 10^3 \text{ cm}^{-1}$. This is comparable to the values reported for POLIS in bulk InP [17].

Furthermore, the absorption increases strongly below $\lambda = 1550$ nm, suggesting that the bandgap of the QW has not changed much after bonding and substrate

removal. Since the bandgap is dependent on the strain in the QW, there was a possibility that strain relaxation in the membrane after substrate removal could shift the bandgap. In order to completely reject this possibility, a PL spectrum of the QW after bonding should be recorded. However, time constraints prevented us from doing this.

In order to demonstrate that the strain and the POLIS effect are still present after bonding, we have to show a wavelength range with TE-absorption and TM-transparency. Unfortunately, the TM grating couplers didn't perform well on this chip (they had high losses and a distorted spectrum, which may indicate overcoupling and should be redesigned with an adjusted filling factor). Therefore, it was not possible to repeat the measurements for the TM polarization with the same precision as for TE. A rough estimate would put the TM modal absorption around 35 ± 20 dB.cm⁻¹ at $\lambda = 1550$ nm, hinting at a useful POLIS behavior still being present after bonding and substrate removal. However, more experiments are required to confirm this.

In the next section, we describe the design of lasers to be fabricated using the POLIS scheme.

7.2 Laser design

A laser is a device that emits light through a combination of light amplification and feedback. They are the most used type of optical source in PICs, because they can be made small (a few μm to hundreds of μm), their output power can be relatively high (tens of mW), and they provide good spectral purity.

7.2.1 Laser principle

Light of a specific wavelength that passes through a semiconductor gain medium can be amplified if the the gain medium is supplied with energy. The energy is typically supplied as an electrical current (electrical pumping) or as light at a lower wavelength (optical pumping). In both cases, the goal is to create electron-hole pairs in the gain material. When an electron and a hole are present at the same place, they can recombine in a non-radiative (no photon emission) or radiative way (one photon is emitted with an energy equal to the difference between the energy states of the electron and the hole involved). If a photon of the appropriate frequency passes through the medium, it can stimulate the electron-hole pair to recombine while emitting an additional photon of the same phase, frequency, polarization and direction. This is called stimulated emission, and is the fundamental principle behind optical gain.

If a gain material is supplied with energy and placed in an optical cavity, light can be amplified during each round-trip through the cavity. Above a certain pumping power (the lasing threshold), the light amplification becomes larger than the cavity losses (caused mainly by absorption, scattering and outcoupling). The power of the recirculating light can then rise exponentially, making the device *lase*. In that case however, since each stimulated emission returns an atom from its excited state to the ground state, the net gain (gain minus losses) reduces to unity, and the laser reaches a steady-state operating point.

Electrical pumping in semiconductor lasers requires processing steps (doping, isolation, metallization) which can be skipped when using optical pumping. Therefore, optical pumping is often used for first laser demonstrations [8]. In the next sections, the laser concepts for both optical and electrical pumping are described.

7.2.2 Optically pumped lasers

In this section, we present four simple laser designs for POLIS: a DBR laser, a DFB laser, a DBR laser with a ring etalon, and a ring laser.

POLIS DBR laser

The first lasers ever constructed were formed by a pair of mirrors on either end of a gain medium. As shown in Chapter 6, a high-quality mirror can be made in IMOS using a DBR. Therefore, a simple POLIS laser can be created using the configuration shown in Fig. 7.4. This DBR laser functions as follows. A TM-polarized pump signal

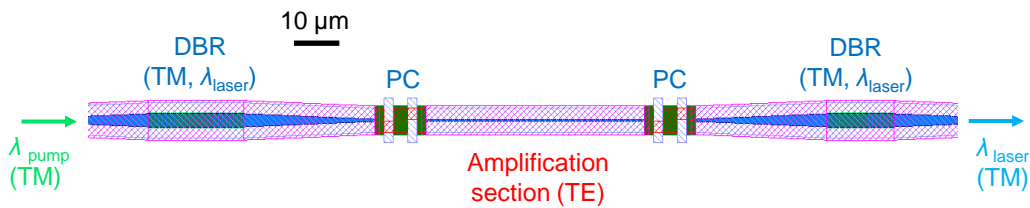


Figure 7.4: POLIS DBR laser design. (PC = polarization converter.)

with a wavelength of λ_{pump} (within the TM transparency range of the POLIS QW) is fed from the left-hand side of the device. The first DBR is designed to transmit λ_{pump} and reflect λ_{laser} , the maximum of the QW gain spectrum, and the expected operation wavelength of the laser. The pump light then reaches the first polarization converter and its polarization is converted to TE. It is subsequently absorbed, due to the POLIS effect and creates electron-hole pairs in the amplification section. These electron-hole pairs recombine to emit TE photons at a wavelength close to λ_{laser} . When these photons reach either polarization converter, their polarization is switched to TM. They can thus propagate without being absorbed and reach the DBR designed to reflect them. Thus a cavity is created between the two DBRs for λ_{laser} photons. The right-hand DBR has a smaller number of periods than the left-hand one, therefore a fraction of the light can escape there and laser emission can be measured.

Since the laser cavity length is much longer than λ_{laser} , the cavity supports several longitudinal modes. Usually, the DBR reflection spectrum is so narrow that only one longitudinal mode can lase. However, as shown in Section 6.1.3, IMOS top-corrugation DBRs, even with a large number of periods, are rather broadband. Therefore, a potential problem faced by this laser is multi-mode operation. To solve this problem, one of the solutions is to reduce the length of the cavity until only one mode can lase. This can be achieved in a DFB laser.

POLIS DFB laser

In the POLIS DFB laser shown in Fig. 7.5, the two DBRs are separated by a quarter-wave shift (160 nm in this case). As in the DBR laser's case, the pump signal is sent

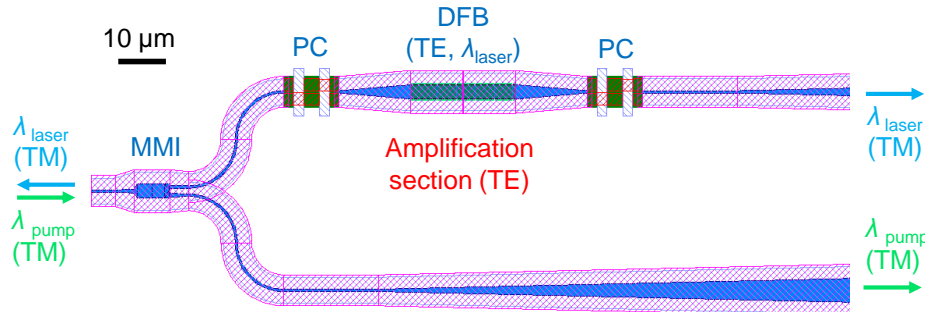


Figure 7.5: POLIS DFB laser design. (PC = polarization converter.)

in the TM polarization from the left-hand side. It is then converted to TE and pumps the QW in the amplification section. Emission at λ_{laser} is amplified and oscillates between the two closely positioned TE DBRs. Finally, some of the λ_{laser} light leaves the cavity, is converted to TM by the polarization converter, and can be detected.

Due to the limited bandwidth of the grating-couplers used to couple light in and out of the chip, it is in general only possible to measure λ_{laser} or λ_{pump} in any given port. The MMI coupler, on the left of the structure in Fig. 7.5 sends half of the pump power to the lower-right port. There, a grating-coupler centered at λ_{pump} can confirm that the fiber on the left is correctly aligned, and thus that the DFB laser is receiving pump light.

Another way to limit the multi-mode operation of a DBR laser is to add a wavelength-selective etalon in the cavity.

POLIS DBR laser with a ring etalon

In Fig. 7.6, we show a POLIS DBR laser with a ring resonator etalon in the cavity. By placing a high-reflectivity DBR at the drop port of the ring resonator, we limit the

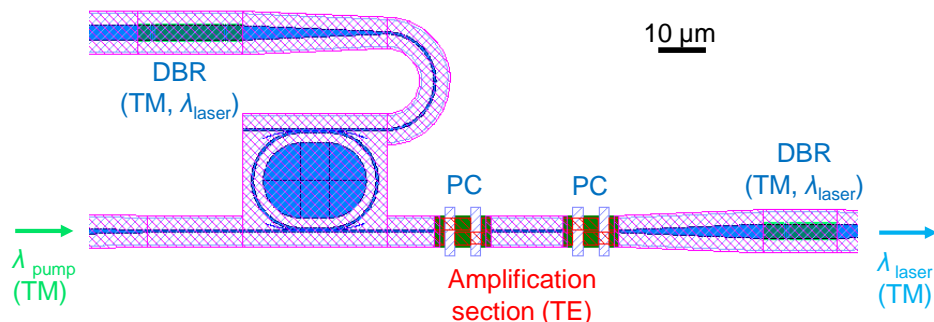


Figure 7.6: POLIS DBR laser design with a ring etalon. (PC = polarization converter.)

range of wavelengths that can oscillate in the laser cavity to the longitudinal modes of the cavity which match the resonant wavelengths of the ring resonator.

Another advantage of the present configuration is that the pump signal can reach the amplification section without having to pass through a DBR. This will increase the pumping power received by the amplification section.

POLIS ring laser

The final laser design considered for the first POLIS fabrication run is a ring laser design, shown in Fig.7.7. This time, the λ_{laser} light generated in the amplification

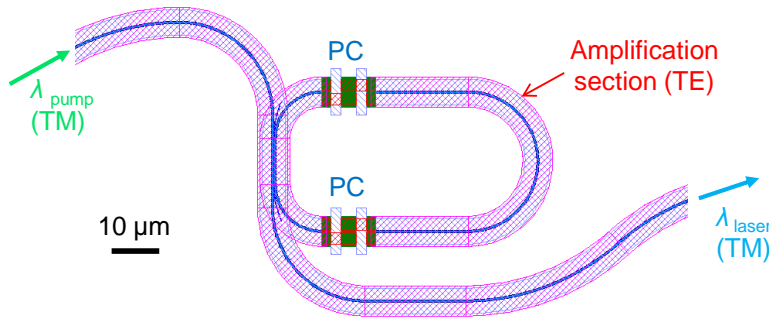


Figure 7.7: POLIS ring laser design. (PC = polarization converter.)

section doesn't reflect back and forth between two DBRs. Instead, it resonates in the ring, provided it matches one of the resonance wavelengths of the ring. Like the POLIS DBR laser described earlier, this laser design is potentially multimode, because several of the ring resonances will fit in the gain band.

7.2.3 Electrical pumping and contacting

Although electrical pumping requires more processing steps than optical pumping, it is the way to go for miniaturization and mass production of semiconductor active devices, especially if they are to be integrated with transistors. Since electrical pumping requires doped layers, it is of particular importance to adjust the layer-stack and the geometry of the amplifier cross-section to reduce the optical loss caused by doping. At the same time, the resistance of the carrier injection path has to be minimized to ensure efficient pumping, and avoid thermal problems which are especially threatening for membrane lasers.

Layer-stack optimization

In an electrically pumped amplifier or laser, gain is achieved by injecting charge carriers (electrons and holes) into the active region. Holes are brought from the p-doped regions, and electrons from the n-doped regions. For the signal to be amplified, the electron-hole pair recombinations have to occur inside the gain medium. In a QW laser, the small bandgap of the QW acts as a trap for both electrons and holes. However, when simulating[†] the first POLIS layer-stack designed for electrical pumping (see table 7.1) under a forward bias of 2.0 V, the band diagram shown in Fig.7.8(a) is obtained. Further analysis shows that the electrons are not trapped in the QW, but

[†]Simulations realized by dr. D. Heiss (PhI), using non-commercial software.

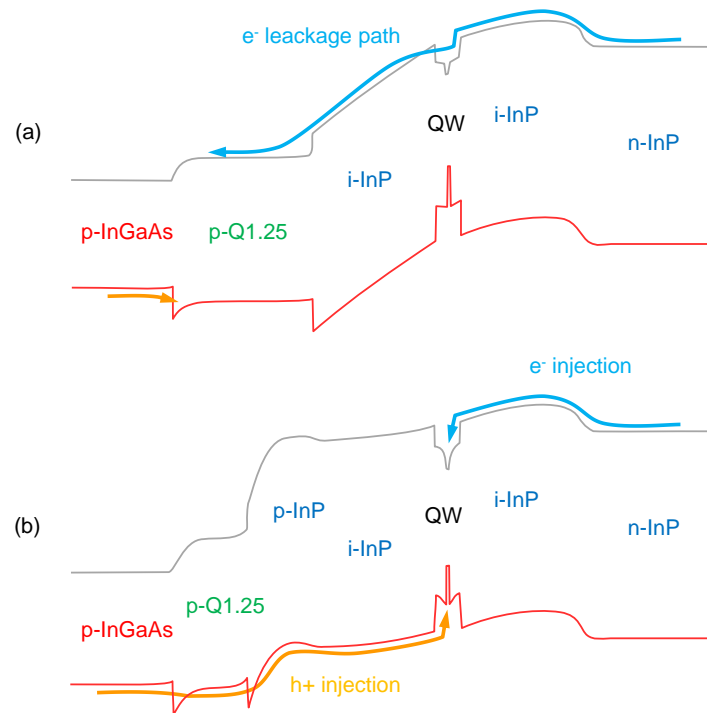


Figure 7.8: Redesign of the p-contact for successful carrier injection in the QW. (a) Band diagram of the POLIS layer-stack under 2.0 V forward bias, with only p-InGaAs and p-Q1.25 in the p-contact, and (b) with an added p-InP layer.

tunnel through the barrier and leak away from it. As a consequence, most of the electron-hole recombinations occur in the p-contact region, and do not contribute to the gain at all.

This problem can be solved by adding a layer of p-doped InP between the intrinsic InP and the p-doped Q1.25 layer. As shown in the band diagram of Fig. 7.8(b), this raises the conduction band on the left-hand side of the QW, effectively preventing injected electrons from tunneling to the p-side. It is estimated that with this new layer-stack, around 90 % of the electron-hole recombinations will occur in the QW region.

Amplifier design

After optimizing the layer-stack, the geometry of the amplifier also has to be designed in order to efficiently inject holes and electrons into the active region. In this work, the diode structure of Fig. 7.9 is chosen to avoid short-circuiting by spatially separating the n and p doped injection paths. Another technique relying on the partial oxidation of an Aluminium containing layer has been investigated previously in IMOS [48]. However, this approach leads to some problems linked to strain, high-temperature and susceptibility to damage by HF.

To reduce the optical mode loss, doped and absorbing layers (InGaAs absorbs strongly at $\lambda = 1550$ nm) have to be placed as far away as possible from the optical mode. However, doping is needed to reduce the resistance of the path followed by carriers to reach the active region. If the resistance is too high, heat will be

generated, potentially leading to permanent damage to the amplifier. In order to find a good compromise between these two effects, the structure of Fig.7.9 is simulated in FIMMWAVE.

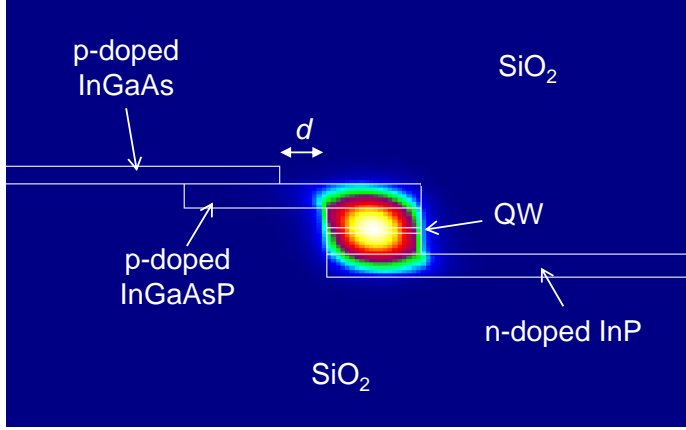


Figure 7.9: Cross-section of the SOA structure simulated in FIMMWAVE.

The QW is placed in the center of the membrane layer-stack. Since this is where the field is strongest, the overlap of the optical field with the QW is maximized, and the efficiency of the amplifier is improved. Furthermore, the non-dominant (TE) field components of the TM polarized mode are absorbed by the POLIS QW. Since these non-dominant components are zero in the center of a symmetric waveguide layer, placing the QW in the center of the membrane stack simultaneously reduces the propagation loss in the passive sections [17].

Due to the very high absorption of InGaAs at $\lambda = 1550$ nm, the most critical geometrical parameter in this structure is the distance d (cf. Fig.7.9) between the p-doped InGaAs contact layer and the active region (QW). A sweep is performed in FIMMWAVE to determine $\Gamma_{p\text{-InGaAs}}$, $\Gamma_{p\text{-InGaAsP}}$ and $\Gamma_{n\text{-InP}}$, the overlaps of the optical mode with each contact layer, as a function of d . The mode loss in $\text{dB}\cdot\text{cm}^{-1}$ is then calculated using:

$$\alpha_{\text{doping}} = 4.34 \times (\Gamma_{p\text{-InGaAs}} \alpha_{p\text{-InGaAs}} + \Gamma_{p\text{-Q1.25}} \alpha_{p\text{-Q1.25}} + \Gamma_{n\text{-InP}} \alpha_{n\text{-InP}}) \quad (7.1)$$

with α_x the material absorption of layer x . The series resistance for each layer is calculated using [17]:

$$R_{s,x} = \frac{d_x}{e \mu_x N_x A_x} \quad (7.2)$$

where d_x is the distance carriers have to travel in layer x , e the electronic charge, μ_x the carrier mobility, N_x the carrier concentration in layer x , and $A_x = t_x \times L$ the cross-section area perpendicular to the carrier path (t_x is the thickness of the layer, and $L = 100 \mu\text{m}$ is the device length chosen for preliminary design).

The result of the simulation is presented in Fig.7.10. As expected, a compromise has to be found. In order to keep the loss below $20 \text{ dB}\cdot\text{cm}^{-1}$, we choose $d = 0.35 \mu\text{m}$. The total series resistance is then around $R_{s, \text{total}} = 70 \Omega$.

In the following section, we describe the first experimental results obtained on

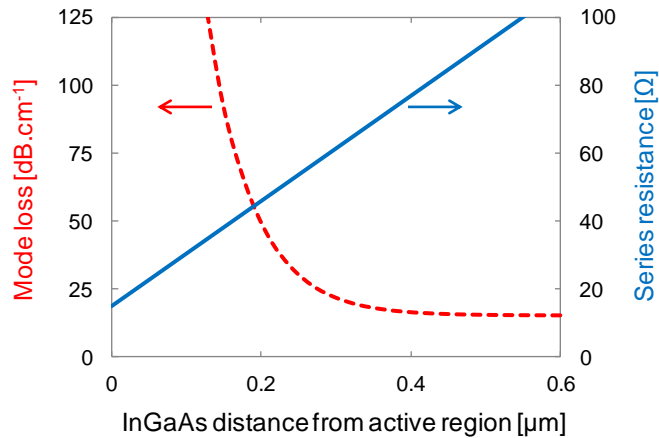


Figure 7.10: POLIS Amplifier mode loss and series resistance as a function of the distance between the InGaAs p-contact and the active region.

an optically pumped laser on an IMOS chip with a POLIS quantum well. Electrical pumping could not be demonstrated because of time constraints.

7.3 Experimental results

7.3.1 Fabrication

A piece of the layer-stack shown in table 7.1, with only layers 4 to 8 (i.e. without any contact layer), was bonded on silicon. The process-flow used for fabricating the polarization converter (see Section 5.2) was then reproduced to create the 4 types of lasers presented in Section 7.2.2. However, all the polarization converters of the chip were damaged in the last step, due to the unexpected high etch-rate of the strained POLIS quantum well in the standard InGaAs/InGaAsP wet etching solution[‡], and possibly also in the standard InP wet etching solution[§].

Fig. 7.11 shows the SEM picture of a polarization converter damaged after etching the slopes of the triangular waveguides. The dashed lines in the bottom right inset indicate the expected shape of the triangular waveguide. The bottom layers (QW / 10 nm InGaAsP / 115 nm InP) have been completely removed. Since this did not happen in the fabrication of the polarization converter without QW, we have to conclude that the problem is caused by the strained POLIS QW. During the slope etch of the triangular waveguides, the QW was most probably etched very quickly, opening the way for the subsequent chemical solutions to etch the underlying layers (see Fig. 7.12(b)).

For future processing of IMOS chips with POLIS material, it is advisable to avoid any wet etching of the strained QWs. One might consider the waveguide cross-section of Fig. 7.12(c), and use it to redesign a polarization converter using the method described in Chapter 5.

[‡] 1H₂SO₄: 1H₂O₂: 10H₂O

[§] 1HCl: 4H₃PO₄

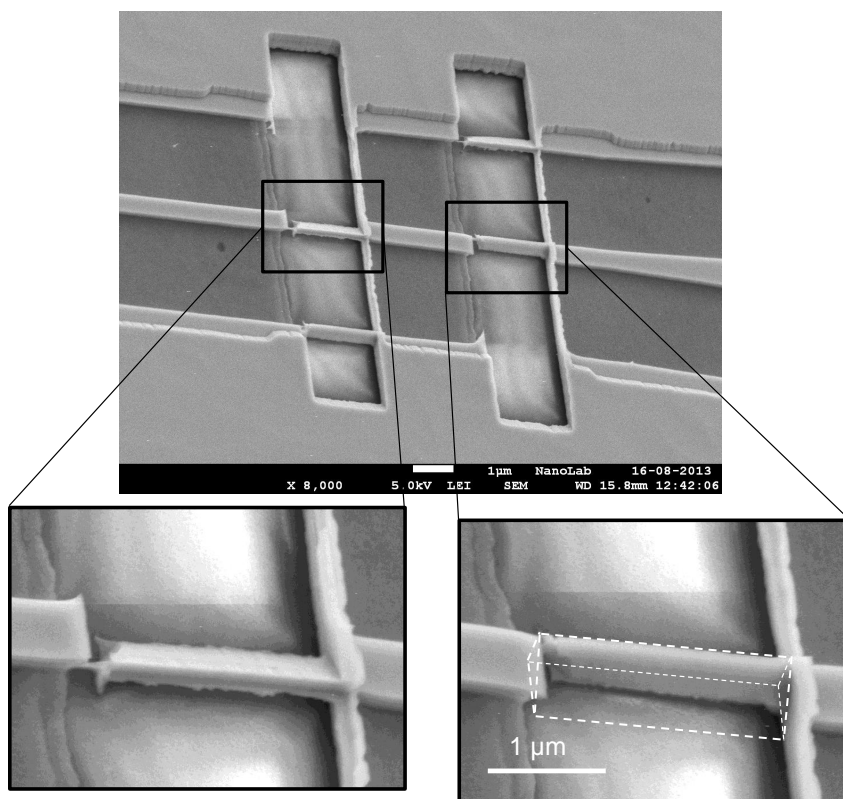


Figure 7.11: Damage to the polarization converter triangular sections, caused by total under-etching of the strained QW during the slope etch.

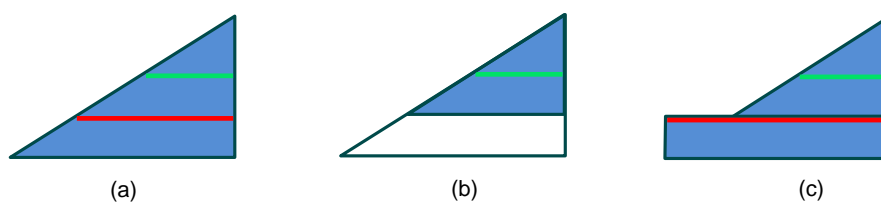


Figure 7.12: (a) Ideal triangular waveguide cross-section. (b) Triangular waveguide obtained with total under-etch of the strained QW (cf. Fig. 7.11). (c) Cross-section considered for a new polarization converter design in POLIS, without QW wet etching.

Because of this unexpected problem, all the devices on the chip were unusable for optical pumping through the waveguide. However, optical pumping from the top was still possible for the DFB lasers. Since also the waveguide path for the laser light was now blocked, only the light scattered out of the cavity in the direction normal to the chip could be detected.

7.3.2 First IMOS laser

In this section, we describe the first successful IMOS laser realized in our group. A SEM picture of the laser is shown in Fig.7.13, while its dimensions are given in table 7.2.

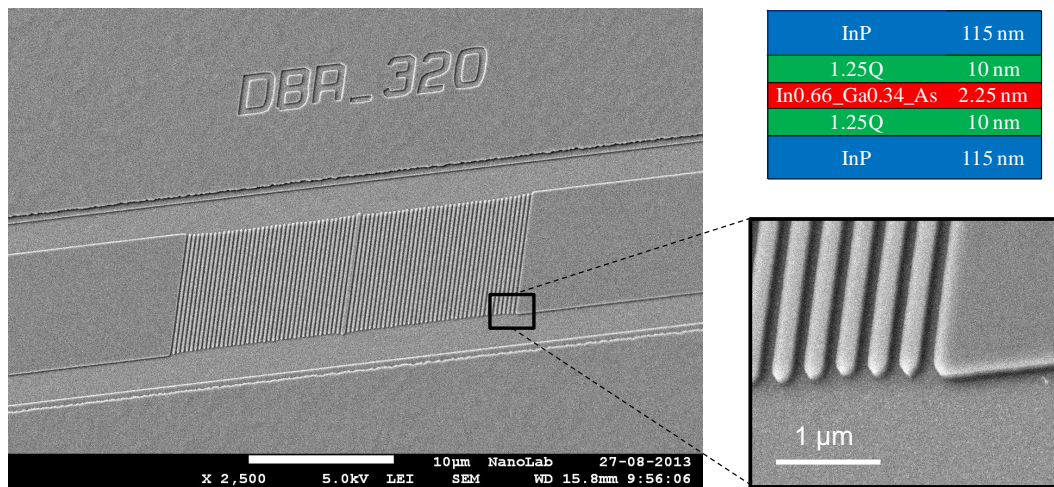


Figure 7.13: SEM picture of the first IMOS DFB laser. (Inset) Layer-stack of the membrane used to print the device.

Parameter	Value
Membrane thickness	252 nm
Waveguide width	10 μm
Waveguide trench depth	105 nm
DBR period	320 nm
DBR etch depth	105 nm
DBR filling factor	55 %
Number of periods	40 × 2

Table 7.2: Dimensions of the fabricated DFB laser shown in Fig.7.13

The DFB cavity is pumped optically from the top using a pulsed laser at $\lambda = 532$ nm (Nd:YAG laser, frequency doubled). with an average optical power of 500 W reaching the sample. A linear polarizer is placed in front of the pump laser, and rotated to reduce in a controllable way the power of the pulses reaching the sample.

The part of the DFB laser emission scattered at the sample surface is also detected from the top, using the same objective lens as the one used to send the pump pulses.

Fig. 7.14 shows the qualitative efficiency curve (normalized emitted power as a function of the normalized pumping power) of the DFB laser, and the spectral distribution of the device emission above threshold[¶].

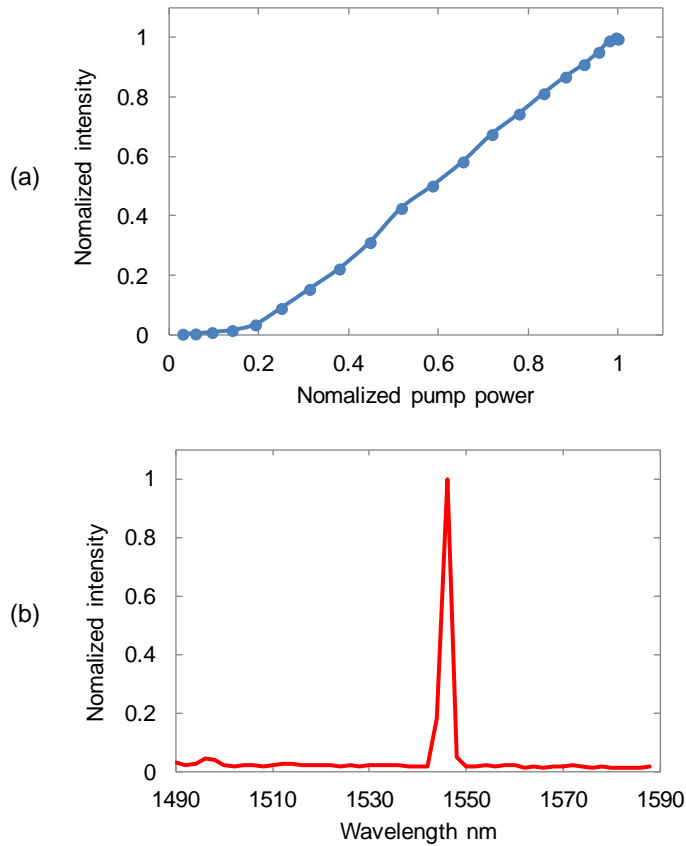


Figure 7.14: (a) Qualitative efficiency curve of the first IMOS DFB laser, showing the typical laser threshold characteristic. (b) Spectral distribution of the light emitted by the device (2 nm resolution).

The efficiency curve shows a clear laser characteristic, with the output power showing a linear dependence with the pump power beyond a certain threshold value. The emission of the laser is centered around $\lambda = 1546$ nm, which is close to the designed value (1550 nm), and well within the telecommunication window.

Considering a QW absorption of 5000 cm^{-1} (cf. Section 7.1), a reflection of 32 % at the air/semiconductor interface, and an overlap of the (circular) pumping spot with the (rectangular) device of around 30 %, a rough estimate of the threshold power gives a value of ~ 20 mW. This estimated threshold is comparable to that reported for similar devices in other InP membrane platforms [8].

Since the DFB laser emission detected in the experiment is only the part scattered at the surface of the chip, the real output power of the laser cannot not be

[¶]Measurements realized by L. Shen (PhI), using setups from the PSN group (TU/e), and Ghent University – imec.

estimated. A useful experiment to carry out would be to pump the DFB laser through the waveguide from one side of the device, and to record the emitted power at the other side, using suitably designed grating couplers.

7.4 Conclusion

In this chapter, we have describes the use of POLIS as an active-passive integration scheme in IMOS. The first IMOS laser realized in our group is reported. This laser is operating at telecommunication wavelengths, and the optically pumped prototype was fabricated in a single etch step. Although more work is needed to realize electrical pumping of low-power lasers in IMOS, this demonstration represents an important step towards the creation of active-passive IMOS chips.

Chapter 8

Conclusions and outlook

8.1 Conclusions

The integration of photonic circuits on top of conventional CMOS computer chips is considered a promising options for the IC industry to continue progressing in accordance with Moore's law. In this thesis, the aim is to demonstrate high-quality devices to generate, guide and control light in circuits fabricated on an Indium phosphide-based membrane bonded on silicon (IMOS). The project has produced the following main achievements:

Technology The IMOS fabrication process-flow is extended to allow post-bonding or double-sided processing of high-quality nanometer and micrometer-sized photonic devices. Waveguide propagation losses as low as 3 dB.cm^{-1} are obtained.

Memory and trimming A memory element based on the combination of a microring resonator with a phase-change material (PCM) is introduced. The measurements performed on a fabricated device show that its transmission at $\lambda = 1550.38 \text{ nm}$ can be reversibly modulated by 12.4 dB, using optical pulses, with a switching time around $5 \mu\text{s}$. This switching time is limited by the heat dissipation dynamics of the structure, rather than by the switching speed of the PCM itself. This device can be used both as an optical memory element, and for the trimming of parameters in photonic integrated circuits.

Polarization conversion A new concept is developed for a $10 \mu\text{m}$ long IMOS polarization converter. A device for efficient TE to TM conversion is designed

and fabricated. The device performs very well over the C-band, and is inherently tolerant to fabrication variations. The device's measured polarization conversion efficiency is more than $> 99 \%$, with losses < 1.2 dB.

Wavelength selection The design and fabrication of a top-corrugation distributed Bragg reflector (DBR) in IMOS are demonstrated, for wavelength filtering or to build laser cavities. The reflectivity of the fabricated device reaches 90% at $\lambda = 1550$ nm, which agrees well with the simulations. Since it can be fabricated in the same steps as the standard waveguides and grating-couplers, this device doesn't require adding extra steps to the standard IMOS fabrication. Furthermore, the first planar concave grating demultiplexer fabricated on an InP-based photonic membrane platform is demonstrated. The device shows 2.8 dB insertion loss, 1.2 dB channel non-uniformity and -18 dB cross-talk. It is a key component for wavelength-division multiplexing (WDM) signal processing, and for creating multi-wavelength lasers.

Light generation Finally, we have carried out the first experiments to apply the POLIS active-passive integration approach in IMOS. Using POLIS material, and the DBR mentioned before, a distributed feedback (DFB) laser is demonstrated. This laser is operating at telecommunication wavelengths and the optically-pumped prototype is fabricated in a single etch step.

8.2 Outlook and recommendations

The work described in this thesis shows the potential of IMOS for providing full photonic functionality in an InP-based membrane. High-quality building blocks necessary for creating complex active-passive circuits have been demonstrated. However, at this point in the development of the IMOS platform, several technological issues remain.

1. During this work, the bonding process has proven to be one of the major bottlenecks. Further improving the quality and yield of the bonding process will lead to a significant increase in the development speed of IMOS circuits.
2. For on-chip interconnection, with circuit lengths on the order of 1 cm, the propagation loss should be decreased further to about $1 \text{ dB}\cdot\text{cm}^{-1}$. One of the most promising directions of research to do this is to further develop the use of the ZEP/C₆₀ or Hydrogen silsesquioxane (HSQ) EBL resists to define waveguides with even lower sidewall roughness.
3. In order to implement the POLIS active-passive integration scheme in IMOS, the essential requirement is a working polarization converter. Since the existing polarization converter design and fabrication scheme leads to unacceptable damage to the device during fabrication on a sample containing a strained POLIS quantum well, a new polarization converter has to be designed and tested. The best option for this is to limit the slanted sidewall of the asymmetric waveguides to the layers above the quantum well.

4. Lasing has been demonstrated in IMOS using optical pumping. However, for interconnect applications, where high-density integration and connections with transistors are required, lasers will need to be electrically pumped. This leads to several new issues requiring attention, including: the isolation between n and p layers, the quality of the metal contacts, and the heat dissipation characteristics. Careful design and extensive testing will be needed to take care of this.

Once the above-mentioned technological issues are fully solved, the next challenge will be to prove that IMOS is a viable solution for on-chip optical interconnects. For this, the energy consumed per bit of data transmitted in the circuit has to be dramatically lowered, in order to legitimize the move from purely electronic IC circuits to photonic/electronic ones. Design of low-power laser sources will be necessary, for example using high-confinement photonic crystal, metallic or plasmonic structures.

Furthermore, the scalability of IMOS devices into very dense circuits has to be studied, and ways have to be found to avoid thermal and optical cross-talk. Finally, the coupling of the light in and out of the photonic membrane will have to be improved if inter-chip optical connections are envisaged.

Bibliography

- [1] D. Miller, “Optical interconnects to electronic chips,” *Applied optics*, vol. 49, no. 25, pp. 59–70, 2010. [Online]. Available: <http://www.opticsinfobase.org/abstract.cfm?URI=ao-49-25-F59>
- [2] P. Kogge, “The tops in flops,” *IEEE Spectrum*, vol. 48, no. 2, pp. 48–54, 2011.
- [3] D. Miller, “Device requirements for optical interconnects to silicon chips,” in *Proceedings of the IEEE*, 2009, pp. 1166 – 1185.
- [4] S. Assefa, F. Xia, and Y. a. Vlasov, “Reinventing germanium avalanche photodetector for nanophotonic on-chip optical interconnects.” *Nature*, vol. 464, no. 7285, pp. 80–84, Mar. 2010. [Online]. Available: <http://www.ncbi.nlm.nih.gov/pubmed/20203606>
- [5] F. Xia, L. Sekaric, and Y. Vlasov, “Ultracompact optical buffers on a silicon chip,” *Nature Photonics*, vol. 1, pp. 65–71, Jan. 2007. [Online]. Available: <http://www.nature.com/doi/10.1038/nphoton.2006.42>
- [6] G. Li, J. Yao, H. Thacker, A. Mekis, X. Zheng, I. Shubin, J.-H. Lee, K. Raj, J. E. Cunningham, and A. V. Krishnamoorthy, “Ultralow-loss, high-density SOI optical waveguide routing for macrochip interconnects,” *Optics Express*, vol. 20, no. 11, pp. 12 035–12 039, 2012. [Online]. Available: <http://www.opticsinfobase.org/abstract.cfm?URI=oe-20-11-12035>
- [7] S. Keyvaninia, G. Roelkens, D. Van Thourhout, C. Jany, M. Lamponi, A. Le Liepvre, F. Lelarge, D. Make, G.-H. Duan, D. Bordel, and J.-M. Fedeli, “Demonstration of a heterogeneously integrated III-V/SOI single wavelength tunable laser,” *Optics Express*, vol. 21, no. 3, pp. 3784–3792, 2013. [Online]. Available: http://www.photonics.intec.ugent.be/download/pub_3099.pdf
- [8] S. Arai, N. Nishiyama, T. Maruyama, and T. Okumura, “GaInAsP/InP Membrane Lasers for Optical Interconnects,” *IEEE Journal of Selected Topics in Quantum Electronics*, vol. 17, no. 5, pp. 1381–1389, 2011.
- [9] Y. Ikku, M. Yokoyama, O. Ichikawa, M. Hata, M. Takenaka, and S. Takagi, “Low-driving-current InGaAsP photonic-wire optical switches using III-V CMOS photonics platform,” *Optics Express*, vol. 20, no. 26, pp. B357–B364, 2012. [Online]. Available: <http://www.opticsinfobase.org/abstract.cfm?URI=ECEOC-2012-Tu.4.E.5>

Bibliography

- [10] J. Van Der Tol, R. Zhang, J. Pello, F. Bordas, G. Roelkens, H. Ambrosius, P. Thijs, F. Karouta, and M. Smit, "Photonic integration in indium-phosphide membranes on silicon," *IET Optoelectronics*, vol. 5, no. 5, pp. 218–225, 2011. [Online]. Available: <http://digital-library.theiet.org/content/journals/10.1049/iet-opt.2010.0056>
- [11] M. Smit, X. Leijtens, E. Bente, J. Van der Tol, H. Ambrosius, D. Robbins, M. Wale, N. Grote, and M. Schell, "Generic foundry model for InP-based photonics," *IET Optoelectronics*, vol. 5, no. 5, pp. 187–194, Oct. 2011. [Online]. Available: <http://digital-library.theiet.org/content/journals/10.1049/iet-opt.2010.0068>
- [12] J. Pello, P. Saboya, S. Keyvaninia, J. Van Der Tol, G. Roelkens, H. Ambrosius, and M. Smit, "Post-bonding fabrication of photonic devices in an Indium phosphide membrane bonded on glass," in *Proc. 16th Annual symposium of the IEEE Photonics Benelux Chapter*, Ghent, Belgium, 2011, pp. 213–216. [Online]. Available: http://photonics.intec.ugent.be/download/pub_2846.pdf
- [13] H. Fukuda, K. Yamada, T. Tsuchizawa, T. Watanabe, H. Shinojima, and S.-i. Itabashi, "Silicon photonic circuit with polarization diversity," *Optics Express*, vol. 16, no. 7, pp. 4872–4880, 2008.
- [14] L. Augustin, "Polarization Handling in Photonic Integrated Circuits," Ph.D. dissertation, Eindhoven University of Technology, 2008.
- [15] G. Roelkens, D. Vermeulen, F. Van Laere, S. Selvaraja, S. Scheerlinck, D. Taillaert, W. Bogaerts, P. Dumon, D. Van Thourhout, and R. Baets, "Bridging the Gap Between Nanophotonic Waveguide Circuits and Single Mode Optical Fibers Using Diffractive Grating Structures," *Journal of Nanoscience and Nanotechnology*, vol. 10, no. 3, pp. 1551–1562, Mar. 2010. [Online]. Available: <http://openurl.ingenta.com/content/xref?genre=article&issn=1533-4880&volume=10&issue=3&spage=1551>
- [16] S. Matsuo, K. Takeda, T. Sato, M. Notomi, A. Shinya, K. Nozaki, H. Taniyama, K. Hasebe, and T. Kakitsuka, "Room-temperature continuous-wave operation of lateral current injection wavelength-scale embedded active-region photonic-crystal laser," *Optics express*, vol. 20, no. 4, pp. 3773–3780, Feb. 2012. [Online]. Available: <http://www.ncbi.nlm.nih.gov/pubmed/22418134>
- [17] U. Khalique, "Polarization based Integration Scheme (POLIS)," Ph.D. dissertation, Eindhoven University of Technology, 2008.
- [18] Ghent-University, "CAMFR." [Online]. Available: <http://camfr.sourceforge.net/>
- [19] S. Keyvaninia, M. Muneeb, S. Stankovic, R. Van Veldhoven, D. Van Thourhout, and G. Roelkens, "Ultra-thin DVS-BCB adhesive bonding of III-V wafers, dies and multiple dies to a patterned silicon-on-insulator substrate," *Optical Materials Express*, vol. 3, no. 1, pp. 35–46, 2013. [Online]. Available: <https://biblio.ugent.be/publication/3159586/file/3159603.pdf>

- [20] R. G. Hunsperger, *Integrated Optics: Theory and Technology*. Springer, 2009.
- [21] F. Payne and J. Lacey, "A theoretical analysis of scattering loss from planar optical waveguides," *Optical and Quantum Electronics*, vol. 26, pp. 977–986, 1994.
- [22] L. P. Gonzalez, J. M. Murray, S. Krishnamurthy, and S. Guha, "Wavelength dependence of two photon and free carrier absorptions in InP," *Optics express*, vol. 17, no. 11, pp. 8741–8748, May 2009. [Online]. Available: <http://www.ncbi.nlm.nih.gov/pubmed/19466123>
- [23] R. Dekker, N. Usechak, M. Först, and a. Driessen, "Ultrafast nonlinear all-optical processes in silicon-on-insulator waveguides," *Journal of Physics D: Applied Physics*, vol. 40, no. 14, pp. R249–R271, Jul. 2007. [Online]. Available: <http://stacks.iop.org/0022-3727/40/i=14/a=R01?key=crossref.507595e7fe44c03dfc5b5bcccc35c262>
- [24] W. Bogaerts, P. De Heyn, T. Van Vaerenbergh, K. De Vos, S. Kumar Selvaraja, T. Claes, P. Dumon, P. Bienstman, D. Van Thourhout, and R. Baets, "Silicon microring resonators," *Laser & Photonics Reviews*, vol. 6, no. 1, pp. 47–73, Jan. 2011. [Online]. Available: <http://doi.wiley.com/10.1002/lpor.201100017>
- [25] A. Vörckel, M. Münster, W. Henschel, P. H. Bolivar, and H. Kurz, "Asymmetrically Coupled Silicon-On-Insulator Microring Resonators for Compact Add-Drop Multiplexers," *IEEE Photonics Technology Letters*, vol. 15, no. 7, pp. 921–923, 2003.
- [26] T. Ishii, H. Nozawa, and T. Tamamura, "Nanocomposite resist system," *Applied Physics Letters*, vol. 70, no. 9, pp. 1110–1112, 1997. [Online]. Available: <http://link.aip.org/link/APPLAB/v70/i9/p1110/s1&Agg=doi>
- [27] B. P. Downey, D. J. Meyer, R. Bass, D. S. Katzer, and S. C. Binari, "Thermally reflowed ZEP 520A for gate length reduction and profile rounding in T-gate fabrication," *Journal of Vacuum Science & Technology B: Microelectronics and Nanometer Structures*, vol. 30, no. 5, p. 051603, 2012. [Online]. Available: <http://link.aip.org/link/JVTBD9/v30/i5/p051603/s1&Agg=doi>
- [28] K. Inoue, D. Plumwongrot, N. Nishiyama, S. Sakamoto, H. Enomoto, S. Tamura, T. Maruyama, and S. Arai, "Loss Reduction of Si Wire Waveguide Fabricated by Edge-Enhancement Writing for Electron Beam Lithography and Reactive Ion Etching Using Double Layered Resist Mask with C60," *Japanese Journal of Applied Physics*, vol. 48, no. 030208, pp. 1–3, Mar. 2009. [Online]. Available: <http://jjap.jsap.jp/link?JJAP/48/030208/>
- [29] Y. Shen, I. B. Divliansky, D. N. Basov, and S. Mookherjea, "Perfect set-and-forget alignment of silicon photonic resonators and interferometers," in *Optical Fiber Communication Conference/National Fiber Optic Engineers Conference 2011*. Washington, D.C.: Osa, 2011, p. PDPC3. [Online]. Available: <http://www.opticsinfobase.org/abstract.cfm?URI=NFOEC-2011-PDPC3>

Bibliography

- [30] M. Wuttig and N. Yamada, "Phase-change materials for rewriteable data storage." *Nature materials*, vol. 6, pp. 824–832, Dec. 2007. [Online]. Available: <http://www.ncbi.nlm.nih.gov/pubmed/17972937>
- [31] R. E. Simpson, P. Fons, A. V. Kolobov, T. Fukaya, M. Krbal, T. Yagi, and J. Tominaga, "Interfacial phase-change memory," *Nature nanotechnology*, vol. 6, no. July, pp. 501–505, 2011.
- [32] S.-Y. Kim, S. J. Kim, H. Seo, and M. R. Kim, "Variation of the complex refractive indices with Sb-addition in Ge-Sb-Te alloy and their wavelength dependence," in *SPIE 3401, Optical Data Storage '98*, 1998.
- [33] M. Abellán, J. Anguita, and N. Sochinskii, "EBL Bi-layer resist scheme for CdTe/Si submicron structures for lift-off processing," *Microelectronic Engineering*, vol. 84, no. 5-8, pp. 1117–1119, May 2007. [Online]. Available: <http://linkinghub.elsevier.com/retrieve/pii/S0167931707001098>
- [34] P. S. Cho and J. B. Khurgin, "Return-to-zero differential binary phase-shift-keyed multichannel transmission with 25-Gbit/s polarization bit interleaving and 25-GHz spacing," *Journal of Optical Networking*, vol. 2, no. 5, pp. 112–118, 2003.
- [35] D. Vermeulen, S. Member, S. Selvaraja, P. Verheyen, P. Absil, W. Bogaerts, D. Van Thourhout, and G. Roelkens, "Silicon-on-Insulator Polarization Rotator Based on a Symmetry Breaking Silicon Overlay," *IEEE Photonics Technology Letters*, vol. 24, no. 6, pp. 482–484, 2012.
- [36] A. V. Velasco, M. L. Calvo, P. Cheben, A. Ortega-Moñux, J. H. Schmid, C. A. Ramos, I. n. M. Fernandez, J. Lapointe, M. Vachon, S. Janz, and D.-X. Xu, "Ultracompact polarization converter with a dual subwavelength trench built in a silicon-on-insulator waveguide." *Optics letters*, vol. 37, no. 3, pp. 365–367, Feb. 2012. [Online]. Available: <http://www.ncbi.nlm.nih.gov/pubmed/22297354>
- [37] L. Liu, Y. Ding, K. Yvind, and J. r. M. Hvam, "Efficient and compact TE-TM polarization converter built on silicon-on-insulator platform with a simple fabrication process." *Optics letters*, vol. 36, no. 7, pp. 1059–1061, Apr. 2011. [Online]. Available: <http://www.ncbi.nlm.nih.gov/pubmed/21478982>
- [38] J. Yamauchi, M. Yamanoue, and H. Nakano, "A Short Polarization Converter Using a Triangular Waveguide," *Journal of Lightwave Technology*, vol. 26, no. 12, pp. 1708–1714, Jun. 2008. [Online]. Available: <http://ieeexplore.ieee.org/lpdocs/epic03/wrapper.htm?arnumber=4542973>
- [39] B. L. Heffner and P. R. Hernday, "Measurement of Polarization-Mode Dispersion," *Hewlett-Packard Journal*, no. February, pp. 27–33, 1995.
- [40] S. Adachi and H. Kawaguchi, "Chemical Etching Characteristics of (001) InP," *Journal of The Electrochemical Society*, vol. 128, no. 6, pp. 1342–1349, 1981.

- [41] M. K. Smit, “New focusing and dispersive planar component based on an optical phased array,” *Electronics Letters*, vol. 24, no. 7, pp. 385–386, 1988.
- [42] J. Brouckaert, W. Bogaerts, P. Dumon, J. Schrauwen, D. Thourhout, and R. Baets, “Planar Concave Grating Demultiplexer on a Nanophotonic Silicon-on-Insulator Platform,” *Journal of Lightwave Technology*, vol. 25, no. 5, pp. 1269–1275, 2007. [Online]. Available: <http://ieeexplore.ieee.org/lpdocs/epic03/wrapper.htm?arnumber=4167948>
- [43] L. Midolo, “Electromechanical tuning of photonic crystal cavities,” Ph.D. dissertation, Eindhoven University of Technology, 2013.
- [44] S. Rishton and D. Kern, “Point exposure distribution measurements for proximity correction in electron beam lithography on a sub-100 nm scale,” *Journal of Vacuum Science & Technology B*, vol. 5, no. 1, pp. 135–141, 1987. [Online]. Available: http://link.aip.org/link/?JVJB/5/135/1&Agg=doihttp://ieeexplore.ieee.org/xpls/abs_all.jsp?arnumber=4965254
- [45] J. Brouckaert, W. Bogaerts, S. Selvaraja, P. Dumon, R. Baets, and D. Van Thourhout, “Planar Concave Grating Demultiplexer With High Reflective Bragg Reflector Facets,” *IEEE Photonics Technology Letters*, vol. 20, no. 4, pp. 309–311, 2008. [Online]. Available: <http://ieeexplore.ieee.org/lpdocs/epic03/wrapper.htm?arnumber=4443140>
- [46] H. J. S. Dorren, D. Lenstra, Y. Liu, M. T. Hill, and G.-D. Khoe, “Nonlinear Polarization Rotation in Semiconductor Optical Amplifiers: Theory and Application to All-Optical Flip-Flop Memories,” vol. 39, no. 1, pp. 141–148, 2003.
- [47] P. J. A. Thijs, “Strained-layer InGaAs(P)/InP quantum well semiconductor lasers grown by organometallic vapour phase epitaxy,” Ph.D. dissertation, Technische Hogeschool Delft, 1994.
- [48] R. Zhang, “Technology and Device Development for Active/Passive Integration on InP-based membrane on Si (IMOS),” Ph.D. dissertation, Eindhoven University of Technology, 2013.

The above bibliography is created from a Bib_T_EX-database.

List of Abbreviations

AWG	Arrayed Waveguide Grating
BCB	Benzo-Cyclo-Butene
BHF	Buffered HydroFluoric acid
CAMFR	CAvity Modelling FRamework
CMOS	Complementary Metal-Oxide-Semiconductor
COBRA	COmmunication technologies, Basic Research and Applications
DBR	Distributed Bragg Reflector
DFB	Distributed FeedBack
EBL	Electron Beam Lithography
EDFA	Erbium-Doped Fiber Amplifier
FIMMWAVE	FIlm Mode Matching for dielectric WAVEguides
FPR	Free Propagation Region
GST	Ge ₂ Sb ₂ Te ₅ , a phase-change material used in data storage
ICFO	The Institute of Photonic Sciences (Barcelona)
IMOS	InP-based Membrane On Silicon
InP	Indium Phosphide
MMI	Multi-Mode Interference
MZI	Mach-Zehnder Interferometer
OSA	Optical Spectrum Analyzer
PCE	Polarization Conversion Efficiency
PCG	Planar Concave Grating

List of Abbreviations

PCM	Phase-Change Material
PEC	Proximity Effect Correction
PECVD	Plasma Enhanced Chemical Vapor Deposition
PhI	Photonic Integration group (TU/e)
PIC	Photonic Integrated Circuit
POLIS	POLarization-based Integration Scheme
QW	Quantum Well
SEM	Scanning Electron Microscope
SOA	Semiconductor Optical Amplifier
SOI	Silicon On Insulator
TE	Transverse Electric
TM	Transverse Magnetic
ZEP	ZEP520A, Electron-sensitive resist

Building up a membrane photonics platform in Indium phosphide

Since the advent of the integrated circuit (IC) in 1958, electronic chips have revolutionized our society. They are present in every digital appliance from computers and mobile phones to watches and cars. However, integration on ICs has now become so dense that the associated power consumption threatens to prevent the performance improvements usually obtained from miniaturization. A solution proposed to overcome this problem is the use of optical on-chip interconnects.

In this dissertation, the development of a photonic platform suitable for integration on top of computer chips is described. The aim is to demonstrate high-quality devices to generate, guide and control light in circuits fabricated on an Indium phosphide-based membrane bonded on silicon (IMOS).

Chapter 2 contains a detailed description of the IMOS platform concept, software tools, fabrication technology, and characterization technique. The IMOS fabrication process-flow is extended to allow post-bonding or double-sided processing of high-quality nanometer and micrometer-sized photonic devices.

In **Chapter 3**, the main loss mechanisms relevant for the IMOS platform are described. Structures that enable measurement of the propagation losses of waveguides are then presented, and a discussion of several techniques used to reduce them is given. Waveguide propagation losses as low as $3 \text{ dB}\cdot\text{cm}^{-1}$ are obtained.

In **Chapter 4**, the first optical memory element integrated on a photonic platform using phase-change material is presented. This device is based on a microring resonator partially covered with a phase-change material, which can be switched in a fast, reversible and non-volatile way. The measurements performed on a fabricated device show that its transmission at $\lambda = 1550.38 \text{ nm}$ can be reversibly modulated by 12.4 dB, using optical pulses, with a switching time around $5 \mu\text{s}$. This switching time is limited by the heat dissipation dynamics of the structure, rather than by the switching speed of the PCM itself. This device can be used to create memory functionality in IMOS or SOI, as well as for the trimming of certain parameters in realized circuits.

The device presented in **Chapter 5** is used to convert the polarization of signals in IMOS circuits from TE to TM and vice versa. It is based on a new fabrication concept, resulting in the world's smallest polarization converter made to date in InP. The device performs very well over the C-band, and is inherently tolerant to

Summary

fabrication variations. The device's measured polarization conversion efficiency is more than $> 99\%$, with losses < 1.2 dB. It can be used for the implementation of polarization-diversity schemes, light intensity modulation or polarization bit interleaving applications in IMOS.

In **Chapter 6**, two new IMOS wavelength-selective devices are introduced. The first, a distributed Bragg reflector (DBR), can be used for wavelength filtering or to build laser cavities, as shown in the following chapter. The reflectivity of the fabricated device reaches 90% at $\lambda = 1550$ nm, which agrees well with the simulations. The second device is the first planar concave grating demultiplexer fabricated on an InP-based photonic membrane platform. The device shows 2.8 dB insertion loss, 1.2 dB channel non-uniformity and -18 dB cross-talk. It is a key component for wavelength-division multiplexing (WDM) signal processing, and for creating multi-wavelength lasers.

Finally, in **Chapter 7** the potential of a polarization-based active-passive integration scheme (POLIS) in IMOS is explored. Using POLIS material and the DBR mentioned before, a distributed feedback (DFB) laser is demonstrated. This laser is operating at telecommunication wavelengths and the optically-pumped prototype is fabricated in a single etch step.

The work described in this dissertation shows the potential of IMOS for providing full photonic functionality in an InP-based membrane. High-quality building blocks necessary for creating complex active-passive circuits have been designed, fabricated and characterized. Further work, including the demonstration of more complex devices and circuits, as well as the reduction of the energy consumed per bit of data transmitted in IMOS circuits, will tell whether this technology can be applied to revolutionize the IC industry.

Acknowledgments

My wife and I often joke that the Acknowledgments are the most read part of a thesis. Therefore, I will do my best to express my thanks in a neat and thoughtful way, without forgetting any of the special persons who accompanied me through the fantastic voyage leading to PhD graduation.

Meint, your unwavering enthusiasm about photonics and Indium phosphide has always given me inspiration and confidence during my work. I am proud to have been a member of the amazing PhI (OED) group for four years. Sorry that I couldn't make a good AWG in IMOS, but I'm sure someone will very soon!

Jos, I couldn't have dreamed a better supervisor than you. We share not only the first three letters of our names, but also the love of complex challenges (and their solutions), the need for a good work-life balance, and a vision of life based on pure optimism... I really enjoyed the freedom, fun and support I got working with you! *Merci pour tout !*

When IMOS becomes the most successful integration technology of all times, people will look up to its founders as a family of brave and fearless visionaries. I would therefore like to thank my relatives: Fred, Ray, Vathsa, Yuqing, Longfei, Alonso, Shahram, Muhammad and Gunther. It has been an honor to struggle and succeed at each other's sides. The achievements reported in this thesis would not have been possible without you.

Since fabrication is probably the toughest part in an IMOS PhD student's work, I owe the technicians of the NanoLab@TU/e cleanroom a lifelong debt of gratitude for the technological guidance and help they offered me. Jeroen, your legendary knowledge of French culinary terms is an eternal source of happiness and pride... Tjibbe, you are the best captain our football team ever had, and you can even play barefoot! Barry, your stunning musical and poetic mastery is a secret to no one. If there is still one thing you should learn, I think it is bossa nova. Erik Jan, we both share an affinity for electron beams. But don't forget that your real destiny is to become the Dutch Federer!

Doing cutting-edge PhD research in the cleanroom is like operating a pulse laser. Long periods of dark and intense frustration get periodically disturbed by ultra-short bursts of ultimate fulfillment. A special thank to all of you in the cleanroom who brightened the less exciting part of this cycle, and actually made it fun to wear giant Smurf outfits and stay for hours in this clean, bright and noisy environment. Antonio, Manu, Luc, Shahram, Vathsa, Ray, Yuqing, Longfei, Dima D, Giovanni, Elton, Domenico, Hadi, Rui, Sylwester, Aura, Victor, Leonardo, Francesco, Sartoon,

Acknowledgments

Yingchao, Pinxiang, Boudewijn, Milan and Martin, thank you and keep up the good work!

Of course some members of the PhI group are less often seen in the cleanroom. That's because they are working very hard on chip design and characterization in the Potentiaal building! Thank you Jing, Saeed, Valentina, Dima P, Emil, Weiming, Dominik, Aura, Rui, Kasia, Stanislaw, Xaveer, Erwin, Huub, Audrey and Jolanda, for always being available and willing to help me, when I needed it.

My thesis work also benefited greatly from discussion and interaction with members of our sister groups PSN and ECO, including René, Andrea, Rob, Oded, Kevin, Harm, Chigo, Yan, Haoshuo, Zizheng, Patty, Nikos, Nicola and Piet.

I was exceptionally lucky to spend the first four months of 2012 in Barcelona (ICFO), as part of my PhD. I certainly enjoyed the sunny weather, the Mediterranean food and the stunning scenery, but actually I also did some extremely stimulating and productive research there! Valerio and Rob, I would like to thank you very much for making this stay possible and very enriching, personally and scientifically. Miquel, Johann, Dhriti, Marc, Tonglai, Davide, Albert, Ilaria and Nadia, thank you for your warm and unreserved welcome. *Visca el Barça i visca Catalunya!*

Recently, I was also involved in a collaboration with the Niels Bohr Institute in Copenhagen, and actually I spent quite a few weekends in Denmark during all but the first year of my PhD. And so it happened that I made some friends there, and pretty good ones too. Pengfei, Natascha, Martin, Wei Li, Andreas, Gu Yun, Li Qian, Liu Guannan, Guo Yang and Shen Heng, thank you all for the hilarious and delightful moments we spent together!

Of course, I owe much of what I have become today to my family, and in particular to my parents and three brothers! Your unconditional love and support all these years has followed me everywhere I've been. And even if we spend less time together nowadays, a special place is forever reserved for you in my heart!

Finally, we come to the reason why I started a PhD in the first place... My dearest wife Haiyan. Without you, I don't think I would have had the idea to come to this small, dynamic and flat country, let alone lived in Copenhagen and Barcelona! You made me discover so many things about myself, and you make my existence a perpetual travel in both the real world and the mind. You are my inspiration, my happiness and my life...

Wo ai ni :)

List of Publications

Journal articles

- Y. Jiao, J. Pello, A.J. Millan Mejia, L. Shen, E. Smalbrugge, E.J. Geluk, M.K. Smit, & J.J.G.M. van der Tol (2014). “Fullerene-assisted electron-beam lithography for pattern improvement and loss reduction in InP membrane waveguide devices.” submitted to **Optics Letters**.
- H. Ma, P. Tian, J. Pello, P.M. Bendix & L.B. Oddershede (2014). “Heat generation by irradiated complex composite nanostructures.” accepted for publication in **Nano Letters**. (Web: January 6, 2014)
- J. Pello, M. Muneeb, S. Keyvaninia, J.J.G.M. van der Tol, G.C. Roelkens, & M.K. Smit (2013). “Planar concave grating demultiplexer on a InP-membrane-on-silicon photonic platform.” **IEEE Photonics Technology Letters**, 25(20), 1969-1972.
- M. Rudé, J. Pello, R. Simpson, J. Osmond, G.C. Roelkens, J.J.G.M. van der Tol & V. Pruneri (2013). “Optical switching at 1.55 μm in silicon racetrack resonators using phase change materials.” **Applied Physics Letters**, 103, 141119.
- J. Pello, J.J.G.M. van der Tol, S. Keyvaninia, P.J. van Veldhoven, H.P.M.M. Ambrosius, G.C. Roelkens & M.K. Smit (2012). “High-efficiency ultrasmall polarization converter in InP membrane.” **Optics Letters**, 37(17), 3711-3713.
- J.J.G.M. van der Tol, R. Zhang, J. Pello, F. Bordas, G.C. Roelkens, H.P.M.M. Ambrosius, P. Thijs, F. Karouta, & M.K. Smit (2011). “Photonic integration in indium-phosphide membranes on silicon.” **IET Optoelectronics**, 5(5), 218-225.

Conference contributions

- M. Rudé, R.E. Simpson, J. Pello & V. Pruneri, (2013). “Optical Switch based on Microring Resonators and Phase Change Materials.” Presented at the Conference on Lasers and Electro-Optics (CLEO/EUROPE), 12-16 May 2013, Munich, Germany.

List of Publications

- J. Pello, J.J.G.M. van der Tol, H.P.M.M. Ambrosius, P.J. van Veldhoven, M.K. Smit, S. Keyvaninia, & G.C. Roelkens (2012). “Demonstration of an ultra-short polarization converter in InGaAsP/InP membrane.” Presented at the 16th European Conference on Integrated Optics and Technical Exhibition (ECIO 2012), 18-20 April 2012, Barcelona, Spain.
- J. Pello, J.J.G.M. van der Tol, M.K. Smit, M. Rudé, R.E. Simpson, V. Pruneri, S. Keyvaninia, & G.C. Roelkens (2012). “Chalcogenides applied to microring switching.” Presented at the 16th European Conference on Integrated Optics and Technical Exhibition (ECIO 2012), 18-20 April 2012, Barcelona, Spain.
- J. Pello, P. Saboya, S. Keyvaninia, J.J.G.M. van der Tol, G.C. Roelkens, H.P.M.M. Ambrosius & M.K. Smit (2011). “Post-bonding fabrication of photonic devices in an Indium phosphide membrane bonded on glass.” Proceedings of the 16th Annual symposium of the IEEE Photonics Benelux Chapter, 01-02 December 2011, Ghent, Belgium, (pp. 213-216).
- J. Pello, J.J.G.M. van der Tol, G.C. Roelkens, H.P.M.M. Ambrosius & M.K. Smit (2010). “Design of a new ultra-small polarization converter in InGaAsP/InP membrane.” Proceedings of the 15th European Conference in Integrated Optics (ECIO 2010), 6-9 April 2010, Cambridge, United Kingdom, (pp. WeB2-1/2).

Curriculum Vitae

Josselin Pello was born on 16 April 1988 in Boulogne-Billancourt (France). He spent the first 20 years of his life in France, graduating from the standard school curriculum with honors, and later specializing in Mathematics and Physics in Lycée Condorcet, Paris, before joining the Institut d'Optique in Palaiseau (France) for a 3-year engineering degree in Optics. In 2008, he chose to spend the last year of this engineering degree in Asia at the Nanyang Technological University (Singapore), taking a Master of Science degree in Electronics. After graduating in 2009, he moved back to Europe and started a PhD project in the COBRA research group of the Eindhoven University of Technology (the Netherlands) of which the results are presented in this dissertation.